Applications of topological reconstruction to reduce the muon induced background in large volume liquid scintillator detectors

Anwendung topologischer Rekonstruktion zur Reduzierung des myon-induzierten Untergrundes in großvolumigen Flüssigszintillationsdetektoren

by

Felix Benckwitz

born on April 9, 1994

Bachelor thesis in physics

Universität Hamburg

March 29, 2017

1. reviewer: Dr. Björn Wonsak
2. reviewer: Prof. Dr. Caren Hagner

Abstract

The Jiangmen Underground Neutrino Observatory (JUNO) detector of 20 kTon liquid scintillator and an optical coverage of 78% yields an energy resolution of 3% per MeV. Therefore, the determination of the mass hierarchy of neutrinos will be possible. Due to the overburden of 700 m rock and the diameter of 34,4 m of the detector target volume, the muon rate is ~ 3 Hz. Thus, the muon background rejection is an important task. Veto strategies for JUNO rely on a good tracking of background events to reduce the effective deadtime of the detector. Especially showering muons yield huge deadtimes, because they are heavily linked to the creation of spallation isotopes ^{9}Li and ^{8}He. These isotopes have decay channels yielding the same coincidence, as the main neutrino detection channel.

Within this bachelor thesis, a reconstruction algorithm for a topological reconstruction of the spatial number density of emitted photons was improved in order to detect and analyse showering muon events. Adjustments for the near field of photomultiplier tubes, a statistical correction for scattered light and algorithms for a fast event topology were applied. Furthermore, the spatial resolution of epicentres of showering muon events was qualitatively examined. Finally, a rough spatial number density of emitted photons for showering muon events was reconstructed minimizing the computation time.

Zusammenfassung

Der JUNO detector stellt mit seinen 20 kTon Flüssigszintillator und seiner optischen Abdeckung von 78% eine Energieauflösung von 3% pro MeV für die Bestimmung der Neutrinomassenhierarchie bereit. Damit ist es möglich, die Massenhierarchie der Neutrinos zu bestimmen. Aufgrund der Überdeckung von 700 m Gestein und einem Durchmesser von 34,4 m des Detektionsvolumens ist die Myonenrate ~ 3 Hz. Damit ist die Unterdrückung des Myonenhintergrunds eine wichtige Aufgabe. Die Vetostrategien für JUNO obliegen dabei einer guten topologischen Bestimmung der Myonen, um die effektive Tozeit des Detektors zu verringern. Vor allem schauernde Myonen bringen große Totzeiten mit sich, da sie primär für die Entstehung von Spaltprodukten wie ^{9}Li und ^{8}He verantwortlich sind. Diese Isotope haben Zerfallkanäle welche das Detektionssignal nachahmen.

In dieser Bachelorarbeit wurde ein Rekonstruktionsalgorithmus für die Bestimmung der örtlichen Wahrscheinlichkeitsdichte emittierter Photonen hinsichtlich schauernder Myonen verbessert. Dafür wurden Anpassungen für das Nahfeld der Photomultiplier, eine statistische Bereinigung von gestreutem Licht und Algorithmen für eine schnelle Topologiefindung angewandt. Weiterhin wurde die Auflösung von schauernden Myonen qualitativ untersucht. Dies resultierte in einer ungefähren örtlichen Wahrscheinlichkeit für emittierte Photonen von schauernden Myonen mit reduzierter Rechenzeit des Rekonstruktionsalgorithmus.

Contents

1 Introduction

First regarded as impossible to detect by its proposer Wolfgang Pauli in 1930, advanced detector technology has made the impossible possible with the detection of the anti electron neutrino via the weak interaction in 1956 by Cowan and Reines.

The characterization of neutrinos has since been approached with a huge effort in particle physics. With the discovery of neutrino oscillations, which described the solar neutrino problem issued by the Homestake experiment by R. Davis in the late 1960s, a new field to measure neutrino parameters has been established. Neutrino oscillations are transitions between the neutrino flavours, measured via the weak interaction. This is possible, because the mass eigenstates and the weak eigenstates of neutrinos are distinct. Neutrino oscillations therefore demand for a non zero neutrino mass. The absolute mass, as well as the mass hierarchy of the three neutrino masses is unknown. Determining, whether the normal mass ordering $m_1 < m_2 < m_3$ or the inverted mass ordering $m_3 < m_1 < m_2$ is true, yields a better discrimination for other neutrino experiments.

For this matter, the multi-purpose neutrino detector JUNO, located near Kaiping, China, is a promising experiment based on the liquid scintillator technology, with the focus set to the neutrino mass hierarchy. Therefore reactor anti electron neutrinos from two nearby nuclear powerplants are to be measured via the inverse beta decay, which yields a coincidence of light signals. Due to JUNO's huge detector volume with a total mass of 20 kT liquid scintillator and an optical coverage of 78%, it provides huge statistics with an excellent energy resolution of 3% per MeV.

With the detection volume of neutrino detectors growing massively over the last decades, a huge demand is set to the background rejection of cosmogenic muons, which produce spallation isotopes in the liquid scintillator yielding the same coincidence upon their nuclear decay. Furthermore it was found in the former Kamioka Liquid Scintillator AntiNeutrino Detector (KamLAND) experiment, that production of spallation isotopes is heavily linked to showering muons. In the KamLAND experiment cosmogenic muons were vetoed with the total measurement data discarded for a designated time. For JUNO this veto rule would yield an effective measurement time of about zero due to the larger muon flux. Thus, a special effort

lies onto the tracking of cosmogenic muons to enable a partial veto for the detector, which reduces the effective deadtime.

Previous tracking methods for large liquid scintillator detectors only involve the determination of the track of the muon, thus only permitting a cylindrical veto around the track. A novel reconstruction approach for the spatial number density of emitted photons developed by Björn Wonsak yields a spatial energy deposition based on an iterative process. This may be an approach to improve the veto strategies with more suitable shapes in the upcoming JUNO experiment.

An enhanced version of the novel reconstruction approach regarding showering muons was developed and discussed in this bachelor thesis. This featured optimizations of the near field of Photomultiplier Tube (PMT)s, a statistical approach to correct scattered light and an algorithm for fast event topologies as an foundation for the novel reconstruction algorithm. Furthermore, a qualitative examination of showering muons with close attention to the detection of epicentres of showering muons was conducted with data simulated with the Low Energy Neutrino Astronomy (LENA) simulation.

Chapter 2 explains the JUNO experiment, as well as the theoretical background of neutrino oscillations, followed by an introduction into the LENA simulation and the novel reconstruction algorithm in chapter 3. The creation of multi-GeV muons, which are most likely to induce a muon shower, with the LENA simulation package is described in section 4.1. The problems of the novel reconstruction algorithm regarding multi-GeV muons are discussed in section 4.2. Then a new approach to correct scattered light in the novel reconstruction algorithm is introduced theoretically in section 4.3 followed by its implementation in section 4.4. An updated version regarding the probability mask as a base for the former algorithm for scattered light is explained afterwards in section 4.5. The evaluation of the enhanced reconstruction algorithm can be looked up in section 4.7 followed by a quantitative examination of the enhanced reconstruction algorithm regarding the detection of epicentres of showering muons in section 4.8.

2 Neutrino physics

This chapter contains the basic physics to understand the motivation and physics goal of the JUNO experiment.

2.1 The Standard Model of particle physiscs

The Standard Model (SM) is the general theory of particle physics concerning the today known fundamental particles, their corresponding antiparticles and interactions excluding gravitation. Todays SM consists of 3 interactions, 12 fundamental fermions and their corresponding anti-fermions, 4 gauge bosons and the Higgs Boson as seen in figure 2.1.

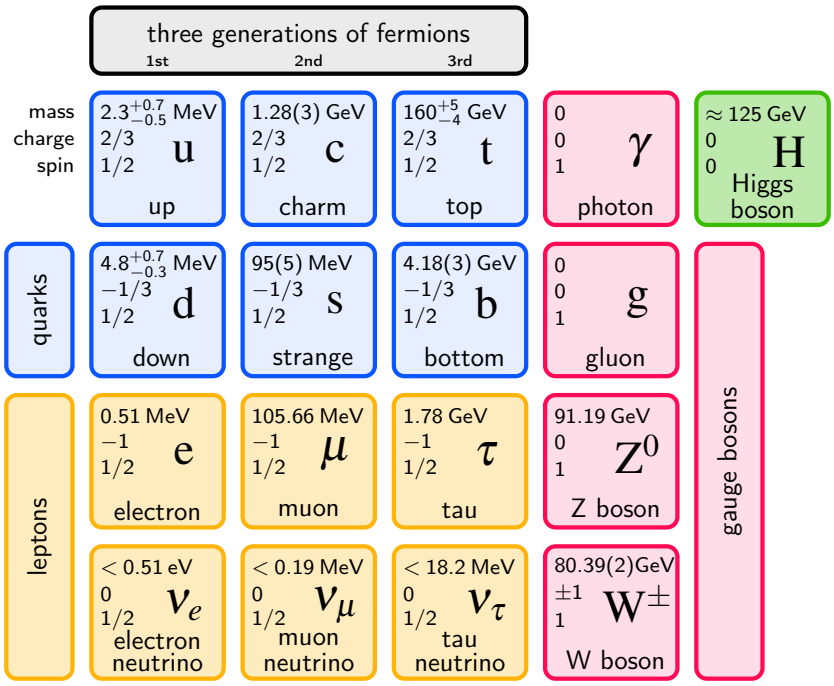

Figure 2.1: Overview of the Standard Model. Designated values for mass, charge and spin from [37]. TikZ-Design by Benedict Kaiser [28].

All known fundamental fermions can be divided into quarks and leptons. The SM contains six quarks of three generations formed by the up/down-, charm/strange- and top/bottom-quark. Quarks carry mass, fractional electric charge and colour charge. Additionally, taking the confinement-theory [18] into account, quarks do not occur isolated and are only found bound in hadrons.

The leptons are represented by the electron e, muon μ and tau τ and the respective neutrinos (electron-neutrino ν_e, muon-neutrino ν_μ, tau-neutrino ν_τ). While the electron, muon and tau carry electric charge the neutrinos are of electric charge zero. All charged leptons carry mass and do not carry any color charge. (See section 2.2).

The gauge bosons are the exchange particles of the three fundamental interactions in the SM and often referred to force carriers.

The theoretical approach of the SM is a gauge theory based on the local symmetry of the gauge group [40]:

$$SU(3)_C \times SU(2)_L \times U(1)_Y \tag{2.1}$$

This gauge group is the direct product of three subgroups as shown in equation 2.1.

The subgroup $SU(3)$ is the color charged sector with the strong interaction described by Quantum Chromo Dynamics (QCD) [19]. Its quantum number is the color charge and its resulting gauge bosons are eight color charged gluons and one color neutral gluon of mass and electric charge zero. Thus only the color charged quarks and the gluon itself take place in the strong interaction.

The $SU(2) \times U(1)$ subgroup is the electroweak sector also referred to as Glashow-Weinberg-Salam-Theory [29]. It describes the electromagnetic- and weak interaction.

The electromagnetic interaction described by Quantum Electro Dynamics (QED) is mediated by its gauge boson, the photon γ, and only affects electric charged particles.

The weak interaction is carried by the $W^\pm$ and Z^0 gauge bosons and couples to all fundamental fermions and the weak gauge bosons. The weak interaction is separated into electric charged currents (Charged Current (CC)) mediated by the $W^\pm$-Bosons and neutral currents (Neutral Current (NC)) mediated by the Z^0 Boson. Contrary to the photon and gluon the gauge bosons of the weak interactions have mass and are thus responsible for "weakness" of the weak interaction as they limit its range.

While the strong and electromagnetic interaction conserve all quantum numbers (except the isospin I), the weak interaction breaks Parity (P) and Charge Parity (CP) symmetry. By parity symmetry the symmetry of a physical process under inversion of all spatial coordinates is meant. Thus the inverted physical process does not violate the laws of physics. The charge parity symmetry covers both parity symmetry and charge symmetry. The charge symmetry is

an inversion of all electrical charges. Thus every particle is replaced by its antiparticle and vice versa.

Additionally the quark flavour can change in weak interactions with the probabilities described in the Cabibbo-Kobayashi-Maskawa (CKM)-matrix [50] since the weak quark eigenstates are superpositions of the quark-mass-eigenstates.

The inclusion of neutrinos in the weak interaction which do not take place in the strong nor the electromagnetic interaction is another notable fact, since it makes neutrinos exquisitely hard to detect.

The Higgs Boson and Higgs-Mechanism as well as gravity gets no further explanation as it is listed only for the sake of completeness.

2.2 Neutrinos

The SM lists the neutrino as a massless Dirac - fermion of spin $\frac{1}{2}$. Furthermore it does neither carry electric nor color charge [37]. Each lepton flavour e, μ, τ has its corresponding neutrino ν_e, ν_μ, ν_τ. The antiparticles correspond to the antineutrinos denoted as $\bar{\nu}_e$, $\bar{\nu}_\mu$, $\bar{\nu}_\tau$. This leaves three generations of leptons.

Being of no electric and color charge neutrinos only interact via the weak interaction making them hard to detect.

To maintain the conservation of energy, momentum and angular momentum in β-decays, Pauli postulated the neutrino in 1930 [18]. Today the β-decay is known to be a weak decay of a neutron n into a proton p, an electron e^- and an anti electron neutrino $\overline{\nu}_e$ (β^--decay)

$$n = p + e^- + \overline{\nu}_e, \tag{2.2}$$

or a proton p into a neutron n, a positron e^+ and an electron neutrino ν_e (β^+-decay)

$$p = n + e^+ + \nu_e. \tag{2.3}$$

A third option, although no β-decay itself, because of the lack of β-radiation, is the electron capture.

$$p + e^- = n + \nu_e. \tag{2.4}$$

A possibility to detect a neutrino works exactly the opposite way via the inverse β-decay [1] as seen in equation 2.5 [7].

[1] Neglecting the inverse β^--decay since the later introduced JUNO experiment detects reactor antineutrinos [7]

Furthermore, the Feynman diagram in figure 2.2 illustrates the weak interaction via a W^+ gauge boson.

$$p + \overline{\nu}_e = n + e^+ \tag{2.5}$$

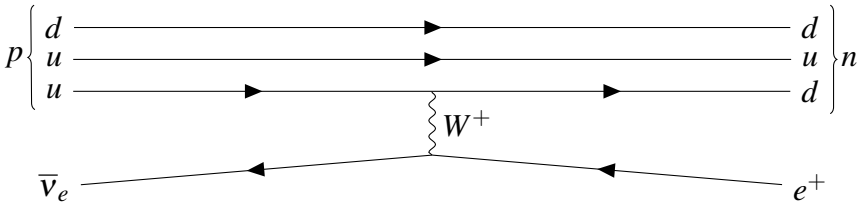

Figure 2.2: Feynman diagram of the inverse β-decay used to detect $\overline{\nu}_e$. Created with TikZ-Feynman [20].

The anti electron neutrino was first detected by Cowan and Reines in 1956 [16] by identifying the inverse beta decay by its coincidence of a positron electron annihilation followed by a neutron capture.

Up to now there are unsolved questions regarding the neutrino. It is still to be clarified whether the neutrino is its own antiparticle (Majorana-fermion) or not (Dirac-fermion). Furthermore the standard model lists the neutrino as a zero rest mass particle, though there is evidence that neutrinos have mass. The absolute neutrino masses as well as the hierarchy of the neutrino masses are still unknown. This matter is described in the following section 2.2.1.

2.2.1 Neutrino-Oscillations

In the later 1960s R. Davis measured a deficit of less than one half of the electron neutrino flux predicted by J.N. Bahcalls standard solar model [9, 17].

Further evidence was given by the Sudbury Neutrino Observatory (Sudbury Neutrino Observatory (SNO)) directly indicating a non-electron flavour component in the solar neutrino flux [14].

Instead of changing the standard solar model the so called solar neutrino problem was explained with neutrino flavour changing.

Like quarks the weak eigenstates of neutrinos are superpositions of their mass eigenstates. With these two sets of eigenstates being distinct lepton flavour mixing (neutrino oscillations) is enabled. In the consequence neutrinos must carry mass [2].

In a short theoretical introduction based on [50] the neutrinos are described by the n flavour eigenstates $|\nu_\alpha\rangle$ and the n mass eigenstates $|\nu_i\rangle$.

[2] For simplicity massive neutrinos in oscillations are called neutrinos, too

Both sets of eigenstates are orthonormal (see equation (2.6)).

$$\langle \nu_\alpha | \nu_\beta \rangle = \delta_{\alpha\beta} \qquad \langle \nu_i | \nu_j \rangle = \delta_{ij} \tag{2.6}$$

Furthermore they are connected by the $n \times n$ unitary mixing matrix U [3]:

$$|\nu_\alpha\rangle = \sum_i U_{\alpha i} |\nu_i\rangle \qquad |\nu_i\rangle = \sum_\alpha U^*_{\alpha i} |\nu_\alpha\rangle \tag{2.7}$$

The stationary mass eigenstates show dependence in time and position (See equation 2.8) assuming a neutrino propagating with momentum p_i in x-direction.

$$|\nu_i(x,t)\rangle = e^{-iE_i t} e^{ipx} |\nu_i\rangle \tag{2.8}$$

The energy E_i of a neutrino mass eigenstate $|\nu_i\rangle$ can be expressed using the relativistic energy-momentum relation [4].

$$E_i = \sqrt{p^2 + m_i^2} = p\sqrt{1 + \frac{m_i^2}{p^2}} \approx p + \frac{m_i^2}{2p} \approx E + \frac{m_i^2}{2E} \tag{2.9}$$

Whereby the Taylor expansion is justified by $p \gg m_i$ and $E \approx p$ is the neutrino energy. With the weak interaction being the sole way to detect neutrinos, a time dependent development of the neutrino state $|\nu_\alpha(x,t)\rangle$ depending on the n flavour eigenstates $|\nu_\alpha\rangle$ is desirable.

Starting with the unitary transformation 2.7 and using the time and position dependencies (See equation 2.8) of the mass eigenstates $|\nu_\alpha(x,t)\rangle$ can be written as.

$$|\nu_\alpha(x,t)\rangle = \sum_i U_{\alpha i} e^{ipx} e^{-iE_i t} |\nu_i\rangle \tag{2.10}$$

Finally using equation 2.7 the neutrino state $|\nu(x,t)\rangle$ can be written as a superposition of the n flavour eigenstates.

$$|\nu_\alpha(x,t)\rangle = \sum_{i,\beta} U_{\alpha i} U^*_{\beta i} e^{ipx} e^{-iE_i t} |\nu_\beta\rangle \tag{2.11}$$

Given the fact that neutrino masses are different, the phase factors $e^{ipx}e^{-iE_i t}$ in equation 2.11 are different for the terms of the sum. Thus the final flavour state $|\nu(x,t)\rangle$ does not equal the initial flavour state $|\nu_\alpha\rangle$.

[3] For antineutrinos the mixing is given by $|\overline{\nu}_\alpha\rangle = \sum_i U^*_{\alpha i} |\overline{\nu}_i\rangle$

[4] Using natural units: $c = 1$

Multiplying a flavour eigenstate from the left provides the time dependent transition amplitude for a flavour change from $\nu_\alpha \to \nu_\beta$.

$$A(\alpha \to \beta)(t) = \langle \nu_\beta | \nu(x,t) \rangle = \sum_i U^*_{\beta i} U_{\alpha i} exp(-i \frac{m_i^2}{2} \frac{L}{E}) = A(\alpha \to \beta)(L/E) \tag{2.12}$$

The experiment-favoured equation is the spatial dependent amplitude 2.12 using the distance between the detector and source $L = x = ct$ and the relativistic energy momentum relation 2.9. Taking its square of the absolute value provides the transition probability P of flavour state ν_α to ν_β.

$$P(\alpha \to \beta)(t) = |A(\alpha \to \beta)|^2 = \delta_{\alpha\beta} - 4 \sum_{j>i} U_{\alpha i} U_{\alpha j} U_{\beta i} U_{\beta j} sin^2(\frac{\Delta m_{ij}^2}{4} \frac{L}{E}) \tag{2.13}$$

In addition $U_{\alpha i}$ are taken real neglecting CP-violation and $\Delta m_{ij}^2 = m_i^2 - m_j^2$ being the difference between the squared masses of two neutrino states. For the experimental site a fixed L/E leaves a dependency on Δm_{ij}^2 and thus making Δm_{ij}^2 accessible for a measurement.

The n^2 parameters of the unitary mixing matrix can be reduced to $(n-1)^2$ independent parameters due to the realtive phases between the neutrino states. These parameters are commonly divided into $\frac{1}{2}n(n-1)$ weak mixing angles and $\frac{1}{2}(n-1)(n-2)$ CP-violating phases [50]. For the three known lepton flavours U has three weak mixing angles $[\theta_{12}, \theta_{13}, \theta_{23}]$and one CP-violating phase δ and is called the Pontecorvo-Maki-Nakagawa-Sakata(Pontecorvo-Maki-Nakagawa-Sakata (PMNS))-matrix [7]. U_{PMNS} can be parametrized by

$$U_{PMNS} = \begin{pmatrix} c_{12}c_{13} & s_{12}c_{13} & s_{13}e^{-i\delta} \\ -s_{12}c_{23} - c_{12}s_{13}s23e^{i\delta} & c_{12}c_{23} - s_{12}s_{13}s_{23}e^{i\delta} & c_{13}s_{23} \\ s_{12}s_{23} - c_{12}s_{13}c_{23}e^{i\delta} & -c_{12}s_{23} - s_{12}s_{13}c_{23}e^{i\delta} & c_{13}c_{23} \end{pmatrix} \begin{pmatrix} e^{i\rho} & 0 & 0 \\ 0 & e^{i\sigma} & 0 \\ 0 & 0 & 1 \end{pmatrix} \tag{2.14}$$

For reasons of clarity the denotations $c_{ij} = \cos(\theta_{ij})$ and $s_{ij} = \sin(\theta_{ij})$ are utilized. The second diagonal matrix is the Majorana phase matrix which is not affecting neutrino oscillations but is listed for the sake of completeness [7].

Summarizing the standard three lepton flavour case contains six independent parameters given those of the U_{PMNS}-matrix and two neutrino mass-squared differences Δm_{21}^2, Δm_{31}^2.

Evidence for neutrino oscillations and a good measurement of θ_{12},θ_{13},θ_{23},Δm^2_{21} and $|\Delta m^2_{31}|$ (see tab. 2.1) has been established by several experiments regarding solar (e.g. SNO), atmospheric (e.g. Super-Kamiokande), accelerator (e.g. Tokai to Kamioka (T2K)) and reactor (e.g. KamLAND) neutrino oscillations [7, 12].

There are still open issues concerning the oscillations of massive neutrinos. The sign of Δm^2_{31} is yet to be determined. Upon now it is not known, whether the mass hierarchy of the neutrinos follows the normal ordering ($m_1 < m_2 < m_3$, see figure 2.3a) or the inverted ordering ($m_3 < m_1 < m_2$, see figure 2.3a). Note that other neutrino oscillation parameters ($\theta_{13}, \theta_{23}, \delta$) are sensitive to the sign of Δm^2_{31} due to the approach of measurement of the experiments. The absolute values of neutrino masses can not be measured by observing neutrino oscillations and are yet to be determined through other experiments. Though ^{3}H beta decay experiments set the upper boundary for the effective electron neutrino mass $m^{(\text{eff})}_{\nu_e}$ to 2 eV [37]. The effective electron neutrino mass is given by $m^{(\text{eff})}_{\nu_e} = \sqrt{|\sum_i U_{PMNS,1i}|^2 m^2_{\nu_i}}$.

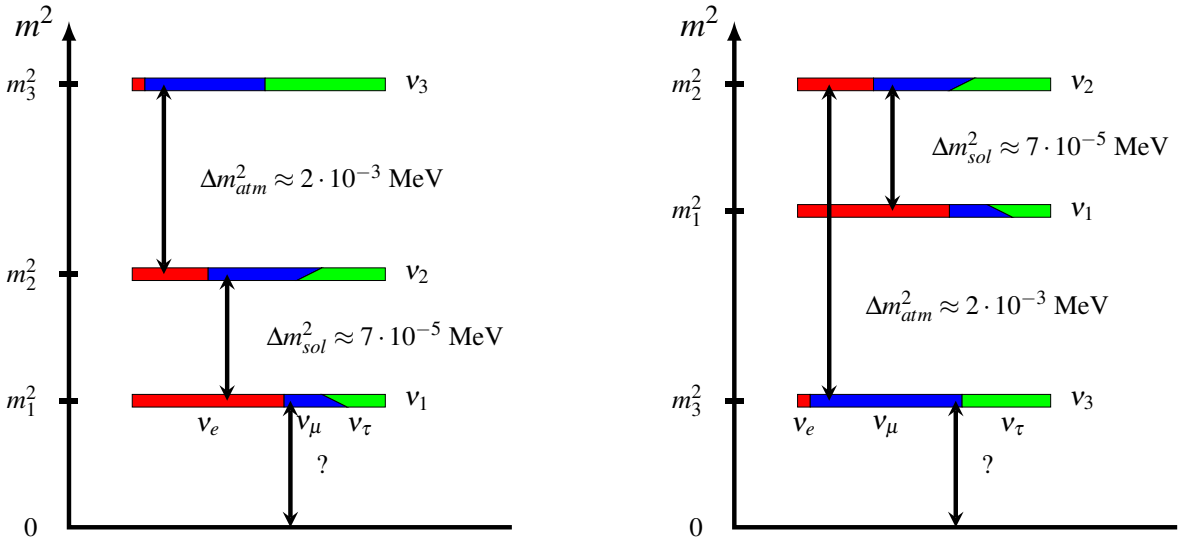

(a) Normal mass hierarchy

(b) Inverted mass hierarchy

Figure 2.3: Visualization of the normal and inverted mass hierarchy. The squared mass differences are denoted by $\Delta m^2_{atm} \sim |\Delta m^2_{31}| \sim |\Delta m^2_{32}|$ and $\Delta m^2_{sol} \sim \Delta m^2_{21}$. Atmospheric (*atm*) and solar (*sol*) are commonly used to denote the mass differences measured with the neutrinos originating from the atmosphere or the sun respectively. The coloured bars represent the mass eigenstates as a composition of the flavour eigenstates with the uncertanties originating from the unknown CP-violating phase δ_{CP} [39].

Furthermore, the CP-violating phase δ_{CP} is yet to be measured precisely with just hints for a non zero $\delta_{CP} \sim 1.4\pi$ [12].

Needlessly to say a precise measurement of all six independent neutrino oscillation parameters is favoured in upcoming experiments. The current state of the six values is presented in tabular 2.1.

Table 2.1: Values of the neutrino oscillation parameters in 1σ range for normal and inverted neutrino mass ordering [7]

Parameter	Normal neutrino mass ordering	Inverted neutrino mass ordering
$\Delta m^2_{21}[10^{-5}eV^2]$	$7.32 - 7.80$	$7.32 - 7.80$
$\Delta m^2_{31}[10^{-3}eV^2]$	$2.41 - 2.53$	$2.36 - 2.48$
$\sin^2(\theta_{12})[10^{-1}]$	$2.91 - 3.25$	$2.91 - 3.25$
$\sin^2(\theta_{13})[10^{-2}]$	$2.15 - 2.54$	$2.18 - 2.59$
$\sin^2(\theta_{23})[10^{-1}]$	$4.14 - 4.70$	$4.24 - 5.94$
δ_{CP}[rad]	$1.12 - 1.77$	$0.98 - 1.60$

Another possible field of application for neutrino oscillations is the search for hypothesized sterile neutrinos. These new neutrino flavours do not participate in the weak interaction but possibly in neutrino oscillations via flavour changes between active[5] and sterile neutrinos. This would expand the earlier introduced three flavour case [7].

This motivates the ongoing scientific effort for experiments regarding neutrino oscillations. The JUNO experiment which is part of these efforts is described in the next section.

2.3 JUNO-Detector

The Jiangmen Underground Neutrino Observatory (JUNO) located in Jiangmen, China near Kaiping city is a multi-purpose neutrino experiment based on a large volume liquid scintillator detector.

The JUNO-Detector has several nuclear power plants (NPP) nearby creating the reactor anti electron neutrino flux needed for JUNO's science goals. The anti electron neutrinos are detected via the inverse β-decay. Thus the detector measures a positron, which ends in a positron electron annihilation, and a signal of a neutron capture [7].

[5] Active neutrinos (ν_e, ν_μ, ν_τ) take part in the weak interaction

Figure 2.4: Location of the JUNO experiment with the Yangjiang and Taishan Nuclear Power Plant (NPP). The distance is $\sim 53\,\text{km}$ for both. For a good overview Hongkong and Kaiping are marked. Created with [2].

For the determination of the neutrino mass hierarchy, the NPP located in Yangjiang and Taishan are of special interest due to their baseline of $\sim 53\,\text{km}$ to JUNO. This baseline length combined with the expected anti electron neutrino spectrum is outstanding regarding the sensitivity for determining the mass hierarchy [1, 7] (For details see 2.3.2).

Regarding the reduction of the flux of cosmic muons, which induce an inadvertent background signal, the JUNO-Detector is to be build in an underground laboratory under the Dashi hill. In total the overburden of granite is more than $700m$, which is 2000m mass water equivalent [43]. This reduces the muon flux to an average of $0.003\frac{\text{Hz}}{\text{m}^2}$ [7].

2.3.1 JUNO: The detector

The detector of the JUNO experiment itself consists of a spheric vessel filled with 20kton liquid scintillator centered in a cylindrical pool of a water Cherenkov detector overlain by a muon tracker.

The central detector has a diameter of 35.4 m and is filled with liquid scintillator[6]. It is surrounded by a 75% to 78% coverage of about 18000 20 inch and 36000 3 inch photo multiplier tubes (PMTs) in a buffer liquid shielding from the radioactivity of the PMT glass. The total diameter of the detector's outter vessel adds up to 40 m [7].

[6] Linear alkylbenzene (Linear AlkylBenzene (LAB)) with a wavelength shifter PPO and bis-MSB [49]

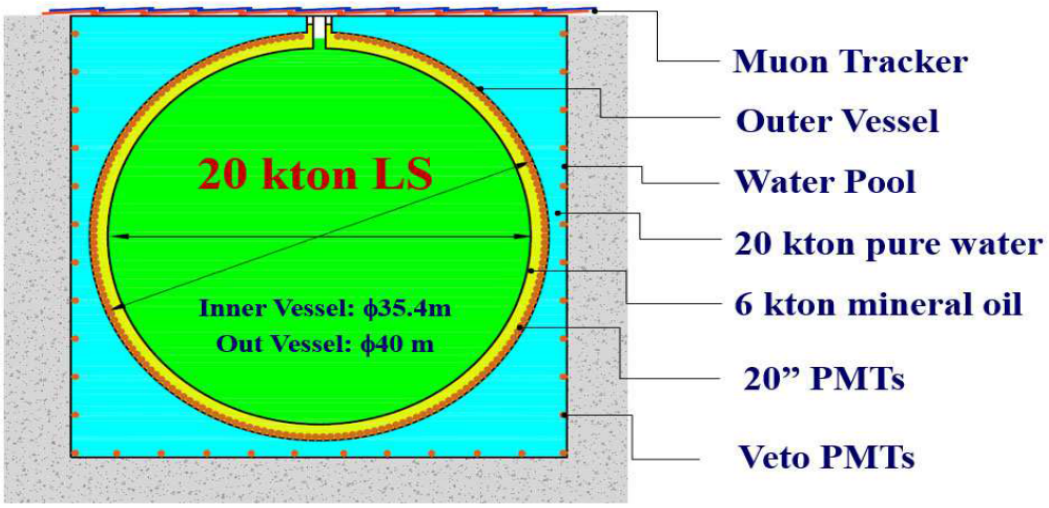

Figure 2.5: Sketch of the JUNO detector [7].

In total a energy resolution of 3% for 1 MeV is to be expected [1], which guarantees an unmatched measurement of neutrino oscillations. The water Cherenkov detector consists out of 20 kTon of pure water with about 2400 20 inch veto-PMTs, which is expected to have a muon detection efficiency of about 99.8%. The pool of water is also used to shield the inner detector from the surrounding radioactivity by keeping a minimum distance of 2 m water to the surrounding rock. The muon tracker on top is also used to measure the muon direction and covers more than 25% of the detector. The OPERA target tracker is reused for this task [7]. The background rejection is an important task for JUNO as the muon rate is $0.0030 \frac{\mathrm{Hz}}{\mathrm{m}^2}$.

With these properties the JUNO-detector is an excellent experiment for the physics goals described in the next section 2.3.2.

2.3.2 JUNO: Physics goals

The main goal of the JUNO experiment is to determine the mass hierarchy of the neutrino masses, which is described explicitly in this section. Furthermore an insight of other application fields is given shortly based on [1, 7].

The neutrinos in JUNO are anti electron neutrinos $\overline{\nu}_e$ originating from a nuclear reactor. They are to be detected via the inverse beta decay. Therefore the survival probability of a $\overline{\nu}_e$ is measured at the designated baseline of ~ 53 km.

The survival probability is given by equation (2.15) as the inverse of the probabilities to

oscillate into another flavour. It can be derived from equation 2.13 using the values of the PMNS matrix (See equation 2.14). The abbreviation $\Delta_{ij} = \frac{\Delta m^2_{ij}}{4}\frac{L}{E}$ is used.

$$\begin{aligned} P(\overline{\nu}_e \to \overline{\nu}_e) &= 1 - P_{12} - P_{13} - P_{23} \\ &= 1 - P(\overline{\nu}_e \to \overline{\nu}_\mu) - P(\overline{\nu}_e \to \overline{\nu}_\tau) - P(\overline{\nu}_\mu \to \overline{\nu}_\tau) \\ &= 1 - \sin^2(2\theta_{12}) c_{13}^4 \sin^2(\Delta_{12}) - \sin^2(2\theta_{13})[c_{12}^2 \sin^2(\Delta_{31}) + s_{12}^2 \sin^2(\Delta_{32})] \end{aligned} \tag{2.15}$$

It is of importance to note that the amplitude is given by the mixing angles θ_{ij} and the frequencies are given by the squared mass differences Δm^2_{ij}.

The first term P_{12} is dominant with a large amplitude respectively and causes the main oscillation based on the solar parameters.

The other two terms have significantly lower amplitudes which only differ slightly. This makes them interfere with each other. Thus they can not be resolved. But it is possible to see the high frequency modulation of P_{13} and P_{23} on the oscillation P_{12} induced by the solar parameters.

With P_{13} and P_{23} being dependent on Δm^2_{13} and Δm^2_{23} respectively, the frequencies of these oscillations are distinct. Thus the mass hierarchy determines the modulation by governing which frequency is larger which is depicted in figure 2.6.

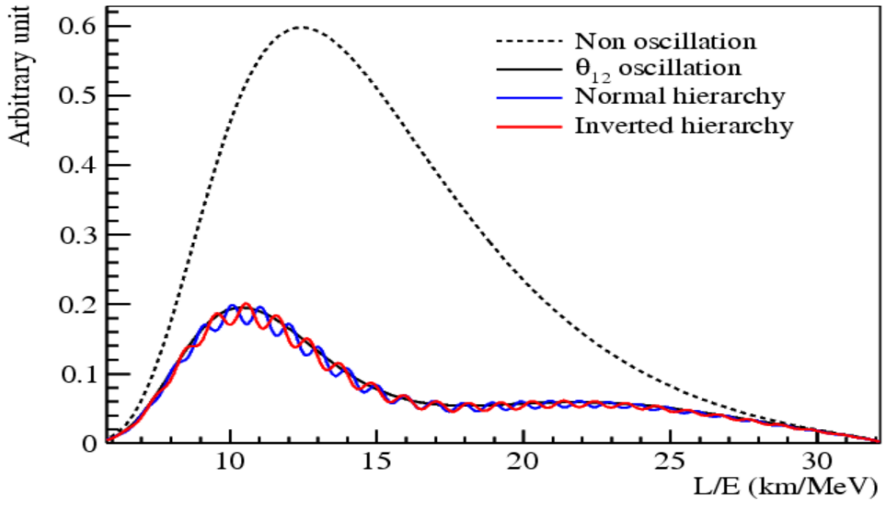

Figure 2.6: Antielectron-neutrino flux in the JUNO detector plotted against $\frac{L}{E}$. The dotted line represents the flux with no neutrino oscillations. The black line represents the oscillations induced by the solar parameters. The modulation of the normal mass ordering is marked in blue, the modulation of the inverted mass ordering is marked in red. Figure taken from [1].

The anti electron neutrino flux in arbitrary units is plotted against the conventional distance over energy L/E. The continuous black line represents the neutrino flux dominated by the oscillation of P_{12}. The modulations of P_{13} and P_{23} are painted in blue and red for the normal and inverted mass hierarchy respectively. The modulation of the normal mass ordering and the inverted mass ordering have a phase shift. This difference can be measured with the high energy resolution provided by the JUNO detector. Furthermore, JUNOs baseline length is at a point L/E in figure 2.6 where a good discrimination between both mass hierarchies is possible. A significance between 3 to 4 sigma is expected [1].

Furthermore JUNO, not limited to only detect reactor neutrinos, is designated to measure the three oscillation parameters Δm^2_{12} Δm^2_{23} and θ_{12} on a new level of significance. (see tabular 2.2).

Table 2.2: Current and expected precision on the three oscillation parameters Δm^2_{21}, Δm^2_{31} and $\sin^2(\theta_{12})$. [7]

Parameter	Current precision	Expected precision with JUNO
Δm^2_{21}	3%	0.6%
Δm^2_{31}	5%	0.6%
$\sin^2(\theta_{12})$	6%	0.7%

JUNO's magnificent energy resolution and its huge statistics due to its event rate promise a precision partially of a magnitude less than former experiments. This allows a better discrimination for other experiments regarding the neutrinoless double beta decay [7] or the measurement of the CP-violating phase δ_{CP} [1].

Although the solar neutrino problem was solved by the SNO experiment [14] and a wide range of the solar neutrino spectrum was measured by the Borexino-detector [42] there is still an open question regarding the flux of the CNO-cycle (Carbon (C) - Nitrogen (N) - Oxygen (O)- cycle), a nuclear fusion chain converting hydrogen (H) into helium (He) [10]. A precise measurement by JUNO would give insight on the metallicity of the sun.

In addition neutrino oscillations below neutrino energies of 1MeV are best described with vacuum oscillations and neutrino oscillations with neutrino energies beyond 3MeV are dominated by the Mikheyev-Smirnov-Wolfenstein effect [45]. Measuring the full ${}^{8}_{0}B$ solar neutrino spectrum[7] could verify this theory in the critical transition area of $1-3MeV$ which is not yet

[7]The β^+-decay of boron-8 yields electron neutrinos in a wide energy range of 10^{-1} to 10^{1}MeV [13]

measured precisely [1]. JUNO, being a spherical liquid scintilaltor detector similar to Borexino, can do this measurement potentially more precisely with its large statistics, high energy resolution and low energy threshold [7].

Also geoneutrinos originating from nuclear decays of radioisotopes in the earth's interior are of interest. Geoneutrinos will have an expected rate of 300 to 500 interactions per year in JUNO [7], can be examined with less uncertainty than Boron Solar Neutrino Experiment (BOREXINO) and KamLAND [21] and may yield more insight on the current geophysical models.

Furthermore a supernova which emits 99% of its energy as neutrinos can be detected with JUNO. A neutrino burst of a Supernova of $\sim 10\,\text{kpc}$ distance is expected to result in about 5000 neutrino events in a few seconds [1]. Another field of application is the Diffuse Supernova Neutrino Background (DSNB) which is formed by the neutrinos originating from the Supernovae of the universe. The low-energy neutrinos of the DSNB may be detected with JUNO [7] and give insight on the rate of star emergence.

Finally JUNO will be a good tool to search for new physics such as sterile neutrinos, neutrinos from dark matter annihilation processes in the sun and possible non standard neutrino interactions. This may be an answer to the some still unsolved problems in modern physics.

2.3.3 Muon background in JUNO

Primary cosmic radiation (e.g. high energy protons) produces pions and kaons in the atmosphere of the earth. Pions and kaons are mesons which occur on both charged $\pi^{+,-}$, $K^{+,-}$ and neutral π^0, K^0 states in the atmosphere. The charged pions and kaons decay into muons, via the following decays:

$$\pi^+/K^+ \to \mu^+ + \nu_\mu, \qquad \pi^-/K^- \to \mu^- + \overline{\nu}_\mu. \tag{2.16}$$

Muons originating from the atmosphere are called cosmogenic muons. The muon flux of the atmosphere is heavily impacted by the matter surpassed. Therefore liquid scintillator detectors are built in underground laboratories. The total muon event rate of JUNO is expected to be $5s^{-1}$ which is caused by the small overburden of 700m [24]. The expected energy distribution of single muon events can be seen in figure 2.7a.

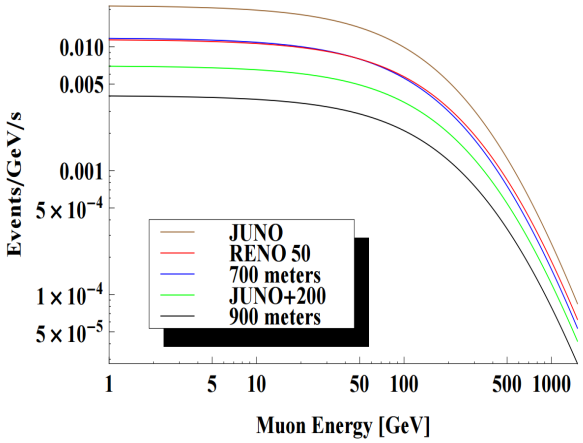

(a) Energy distribution of single muon events at depths for JUNO and Reactor Experiment for Neutrino Oscillation (RENO) 50 (a similar experiment to JUNO). Furthermore, reference depths of exactly 700 m or 900 m, as well as the depth of JUNO plus 200 m are depicted. Figure from [23].

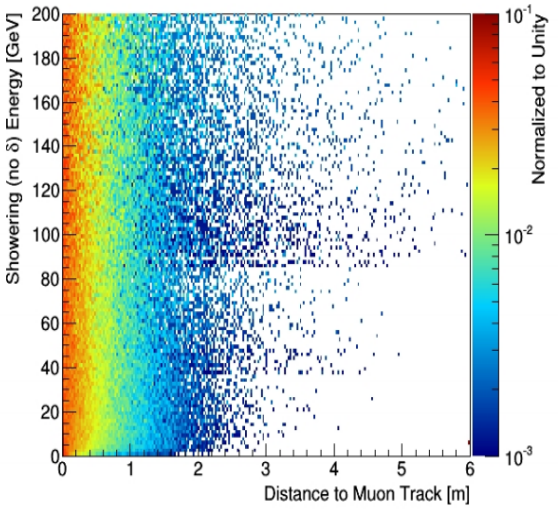

(b) Radial distribution of the ^{9}Li isotopes around the muon track (x-axis) with showering energy (y-axis). 99% of the ^{9}Li production is within 3.5 m around the track of the muon. Figure from [24].

Figure 2.7: **(a)**: Energy distribution of single muon events at variuos depths. **(b)**: ^{9}Li isotope production around the muon track with respect to the showering energy. Both simulations are FLUktuierende KAskade (FLUKA) simulations [23, 24].

Cosmogenic muons passing large area liquid scintillator detectors such as JUNO are heavily linked to the creation of cosmogenic radioisotopes like ^{9}Li and ^{8}He. These isotopes are produced via cosmogenic muon spallation on ^{12}C in the liquid scintillator [23].

The cosmogenic radioisotopes can decay yielding the same coincidence which is used to detect anti electron neutrinos. This decay channel for ^{9}Li is divided into two parts. First the

^{9}Li decays via the β decay. Subsequently ^{9}Be decays into two α particles and a neutron n.

For ^{9}Li the background rate in JUNO is expected to be $8.5 \cdot 10^{-4}$ Hz with the coincidence mimicking decay channel weighted with 51%. The values for ^{8}He are $3.0 \cdot 10^{-5}$ Hz and 16% respectively [24,31]. Thus the ^{9}Li background is of primary interest for the JUNO experiment. Furthermore, the creation of ^{11}C produces a neutron capture, which can possibly be interpreted for coincidence with a non correlated β-decay, which may be yield by other spallation isotopes (See table I in [31]).

In particular it was found in KamLAND that radioisotope occurence is heavily amplified by showering muons [15]. Showering muons are classified by an additional energy deposition of $E_{shower} > 3$GeV to their ionization energy $E_{ionzation}$. The ionization energy can be precisely calculated with a muons differential energy loss of $dE/dx|_\mu = 1.43$MeV/cm (minimal ionisation) [23]. The radial distribution of the ^{9}Li isotopes around the muon track with a particular showering energy can be seen in figure 2.7b. Furthermore about 99% of the ^{9}Li is within a range of 3.5 m around the track of the muon [24].

The physical process of a showering muon is mostly the showering of an electron produced in an ionization process of a muon as muons itself do not radiate high amounts of bremsstrahlung.

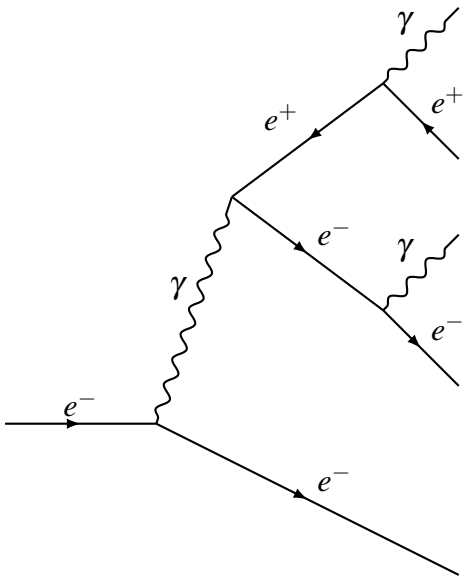

Figure 2.8: Showering electron: The electron yields a photon due to bremsstrahlung which interacts via pair production production. The positron and electron then yield another photon which then can interact again via pair production.

Furthermore a hadronic shower of a proton due to ^{12}C spallation is possible. As hadronic showers induce electromagnetic showers due to π^0 production via the strong interaction, elec-

tromagnetic showers are induced by the photons of the $\pi^0 \rightarrow \gamma\gamma$ decay. The cascade of an electromagnetic shower starts with an electron yielding a high energy photon, which is permitted in matter. These high energy photons primarly interact with the liquid scintillator via pair production. Pair production is the conversion of a photon into an electron and a positron, which is permitted for photons in matter, if the energy exceeds the energy of two electron rest mass energies. The electron and positron created in the pair production often have enough energy to yield another photon which then interacts again via pair production. This cascade is stopped when the energy of the photons fall below the energy threshold of two electron rest masses which energetically forbids another pair production [38]. A showering electron is depicted in figure 2.8.

Another problem induced by JUNO's size are muon bundles travelling nearly the same direction. With a typical distance of 10m at the JUNO experiments depth the muon bundles make up $17-20\%$ of the muon events [23].

With a showering probability of 20% for a single muon and 30% for a muon bundle [23], the muon background rejection is an important task.

2.3.4 Vetostrategies for JUNO

In preceding experiments with small liquid scintillator detectors (e.g. KamLAND) compared to JUNO this background was mostly rejected using a full detector veto of 2s.

Applying this kind of veto strategy to JUNO would cause a vanishing measurement time due to the high muon event rate in JUNO.

With a larger background signal than the original signal in large liquid scintillator detectors this demands inevitably for a new approach to veto the cosmogenic muons.

Current analyzation of veto strategies regarding the spallation isotope background in JUNO imply a full detector veto for not successfully tracked muons with an energy E greater than a threshold energy E_f for a time t_f. If a muon of energy $E > E_c$[8] is well tracked a cylindrical veto of radius r_c around the muons track is applied for a time t_c. Muons below these threshold energies are eventually not vetoed. It has been shown that the rejection efficiency can increase if muons below an energy threshold are not vetoed [24]. This is due to the low isotope production of muons with low energies. These parameters are optimized to create the best possible background rejection for the different science goals of JUNO. For details see [24].

To provide the best possible tracking is an important task for the sensitivity to the mass hierarchy and other physics goals in JUNO.

Although the imperfect tracking of single muons[9] is mostly negligible, the current tracking problems of muon bundles, as they have a significant occurence rate, is not [24].

The veto strategy for JUNO is therefore bound to the tracking ability of muons. A good tracking of single muons and muon bundles is needed.

Furthermore the reconstruction of muon showers could decrease the vetoed detector volume. The shower probability and the probability of surpassing the whole detector rises with the muon energy. A full track cylindrical veto whose radius r_c is only determined by the shower could therefore be replaced by a more suitable shape.

A new approach to a topological reconstruction which may solve these issues is presented in section 3.4.

[8] E_c is in fact a second threshold energy for well tracked muons
[9] If $10-20\%$ of all muon events are poorly tracked

2.4 LENA-Detector

This section describes the proposed Low Energy Neutrino Astronomy (LENA) experiment located in the Pyhäsalmi mine, Finland. Since simulations and reconstruction of muon events was executed in the LENA detector geometry the experiment is of importance for this thesis. The description will only include the detector (See figure 2.9) as the physics goals are almost analogical with JUNO. For a detailed description see [32].

The LENA detector is a cylindrical shaped 50kton liquid scintillator detector of 96 m height and 14 m radius with about 30000 12 inch PMTs covering about 30% of the detector surface.

Similar to JUNO a Water-Cherenkov-detector is installed with about 2000 PMTs being able to reconstruct the muon background and shield from the natural radioactivity. Furthermore a muon-tracker is installed on the top.

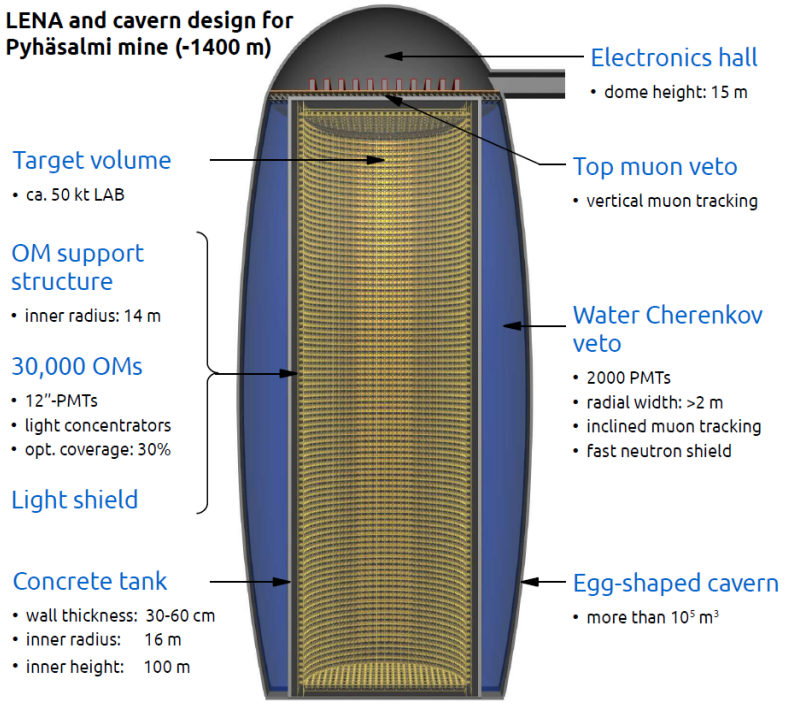

Figure 2.9: Projection of LENA. Optical Module (OM): Optical Module (e.g. a PMT). Figure from [47].

The liquid scintillator is LAB with a wavelength shifter and a luminophore to enhance the light yield [10]. The attenuation length of LAB is ~ 20 m and light yield about 10000 photons per MeV [32].

[10] 3 g/l PPO (luminophore) and 20 mg/l bis-MSB (wavelength shifter) [49]

3 Simulation- and reconstruction methods for the LENA-Detector

This chapter briefly explains the simulation of muon events in LENA and then discusses the new approach to topological track reconstruction in large volume liquid scintillator detectors such as LENA or JUNO. Prior to this, basic effects regarding light in matter[1] and light detection with optical modules (PMTs) with respect to its simulation and reconstruction are explained.

3.1 Scintillation process and light attenuation in liquid scintillator

A liquid scintillator detector design is determined by the light production and its attenuation in the scintillation medium. As these are the main factors regarding the reconstruction of muon events, the focus lies onto the organic liquid scintillator LAB as design studies propose it for the upcoming JUNO experiment [49].

3.1.1 Scintillation process

If a charged particle traverses a liquid scintillator detector, it ionizes the scintillation material with a differential energy loss dE/dx [32]. The scintillation process is the conversion of excitation energy, except heat, into light of a characteristic spectrum. Thus the excited atomic states decay into stable states yielding isotropic distributed photons. This effect is called luminescence.

The differential luminiscence dL/dx is called the scintillation light yield. In organic scintillators about 3% of the deposited energy is converted into photons or one photon is created per 100 eV [37]. In fact the differential luminescence does not depend linearly on the differential

[1] For this work Linear alkyl benzene (LAB)

energy loss due to quenching effects and is semi-empirically described by Birks' formula with Birks constant kB.

$$\frac{dL}{dx} = L_0 \frac{\frac{dE}{dx}}{1 + kB\frac{dE}{dx}} \tag{3.1}$$

Furthermore the time distribution of the scintillation photons is of special interest for the reconstruction. The decay of excited atomic states is a statistical process following an exponential decay function. Given multiple excited states the time distribution is a weighted sum of exponential decay functions [11]. Accordingly the probability density function $\Phi_{photon}(t)$ is given by

$$\Phi_{photon}(t, \mathbf{c}) = \sum_{i=1}^{n} \frac{w_i}{\tau_i} e^{-\frac{t-t_0}{\tau_i}}; \qquad t \geq t_0; \qquad \sum_{i=1}^{n} w_i = 1. \tag{3.2}$$

Where $\mathbf{c} = \{ \begin{pmatrix} \tau_1 \\ w_1 \end{pmatrix}, ..., \begin{pmatrix} \tau_n \\ w_n \end{pmatrix} \}$ are the n components with weight w_i and mean lifetimes τ_i. Additionally t_0 marks the time of excitation.

Moreover relativistic particles with $\beta > \beta_{threshold} = 1/n(E)$ radiate Cherenkov light under the Cherenkov angle $cos(\theta_c) = 1/\beta n(E)$ [27], which is the second source of light along with scintillation light. Here β is the particles speed in vacuum speed of light units c_0 and $n(E)$ is the energy dependent refractive index. As the Cherenkov light is making up only a few percent of the produced light in liquid scintillators it is not further discussed (For detailed information see [32]).

3.1.2 Light attenuation

Prior to a mediums attenuating effects on light it is important to note that the speed of light in a medium is given by the group velocity of a wave package $v_g < c_0$ [27].

The attenuation of light in a medium is dominated by absorption and scattering. Important effects are Rayleigh-scattering off bound electrons, Mie-scattering from scintillator impurities as well as absorption and absorption with reemission[2].

[2]The light is reemitted either in form of light visible to the detector, invisible light(infrared) or heat

The probability density function Φ_{dir} for a photon directly surpassing the medium for a distance $x = |\mathbf{x} - \mathbf{x}_0|$ is given by an exponetial law using the attenuation length L [48]:

$$\Phi_{dir}(x, L) = \frac{1}{L} e^{-\frac{x}{L}}. \tag{3.3}$$

The attenuation length L is given by the propagation lengths of the prior introduced effects:

$$\frac{1}{L} = \frac{1}{L_A} + \frac{1}{L_S}; \qquad \frac{1}{L_S} = \frac{1}{L_{are}} + \frac{1}{L_{ray}} + \frac{1}{L_{mie}}. \tag{3.4}$$

With the absorption length L_A and the scattering length L_S, which in equation 3.4 is determined by the absorption/re-emission length L_{are}, the Rayleigh scattering length L_{ray} and the Mie-scattering length L_{mie}.

The reduction of light reaching the photo detectors limits the scale of liquid scintillator detectors. Furthermore, scattered light is false information as its not related to its origin anymore. Therefore, it does carry information for the energy deposited, but has lost all its information about the topology of the event. Thus these effects heavily affect the later introduced reconstruction method 3.4. For LAB the attenuation length is $\sim$ 20m at a photon wavelength of 430 nm [22].

3.2 Light detection with PMTs

This section covers critical effects regarding the light detection with photomultiplier tubes (PMTs) shortly resuming [30, 32].

PMTs detect photons via the photoelectric effect, thus converting incoming photons into electrons using a photocathode. These electrons get accelerated through an applied potential to a dynode chain, where they release more electrons. Passing the dynode chain the electrical current gets amplified by a factor typically between 10^3 and 10^8. Thus the sole photon signal is transferred into a noticeable electrical signal. A schematic overview of a PMT with photoelectric effect is given in figure 3.1.

Predominantly the light detection efficiency is reliant on the quantum efficiency of the PMT[3]. The quantum efficiency is defined by the number of photoelectrons per photon hit on the photocathode and depends on the photocathodes material, the materials temperature and the wavelength of the photon.

[3] Assuming a nearly perfect capture efficiency. The capture efficiency is the amount of released photocathode electrons hitting the dynode chain

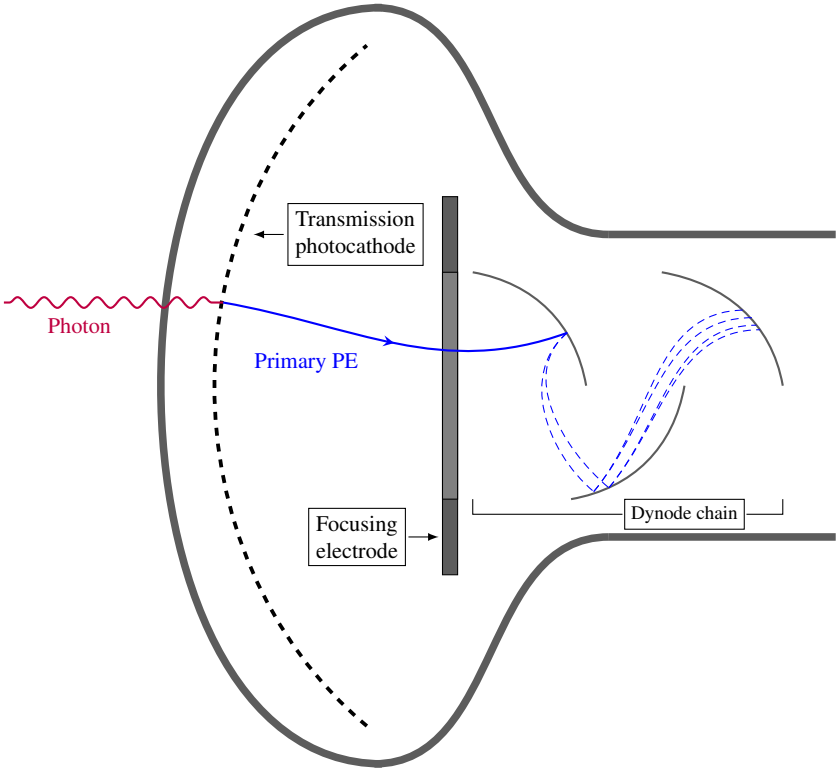

Figure 3.1: Overview over a photomultiplier tube.

Nonetheless the electrics of the PMTs harbour errors. These errors are given by the dark current, pre- and after-pulses. Electrons which leave the photocathode without an incident photon are called dark current. This is caused e.g. by thermally induced emission. Pre-pulses are caused by photons hitting the dynode chain while after-pulses occur during an interaction of an electron with remaining gas in the PMT. The created ion creates another delayed signal when hitting the photocathode. Both effects can shift the signal time over several nanoseconds (See figure 3.2).

These effects have to be taken into account when evaluating event data as photons may be interpreted with false hit times or a dark current signal is taken for a photon hit.

Furthermore, the optical coverage of each PMTs is desired to be as large as possible. Therefore light concentrators (Winston Cones) are used to reflect light from a larger area onto the photocathode. Although they enhance the amount of detected light, they deteriorate the angular acceptance because above a critical incident angle δ_{crit} the light gets reflected back into the detector target. This effect is depicted in figure 3.3.

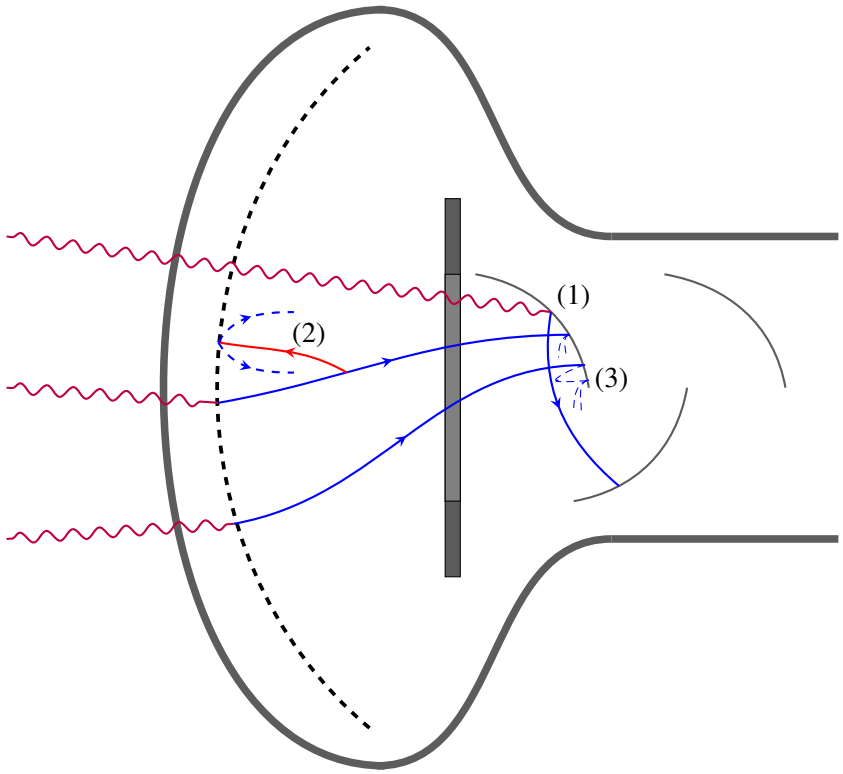

Figure 3.2: Possible origins of pre-pulses due to a photon hitting the dynode chain directly (1) and after pulses due to ionization (2) or elastic scattering of the primary photoelectron (3). The purple lines represent photons, the blue lines represent photoelectrons and the red line represents a positive Ion. Secondary photoelectrons are hinted by dashed blue lines.

3.2.1 Angular acceptance

The angular acceptance is the probability of detecting a photon with respect to its incident angle α. The incident angle is the angle between the photon track and the normal vector of the PMTs photocathode. It is determined by the light concentrator of the PMT. Two possible events of incident photons are shown in figure 3.3. The blue line depicts a photon with an incident angle $\delta_1 > \delta_{crit}$ and gets reflected back. The red line shows a photon with an incident angle $\delta_2 < \delta_{crit}$. Thus the red lines photon hits the PMT.

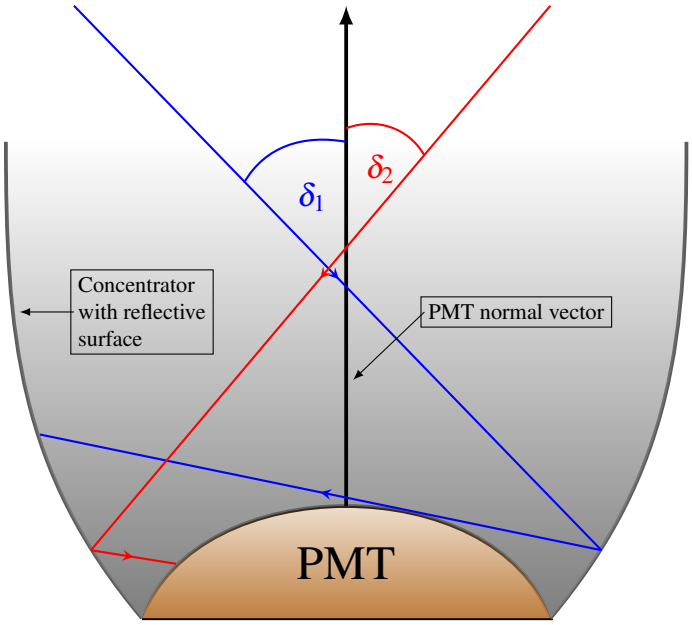

Figure 3.3: Visualization of a PMT with a lightconcentrator with a reflective surface. The incident photon angles are calculated with respect to the PMT normal vector. Two possible events of incident photons are shown. The blue line depicts a photon with an incident angle $\delta_1 > \delta_{crit}$ and gets reflected back. The red line shows a photon with an incident angle $\delta_2 < \delta_{crit}$. Thus the red lines photon hits the PMT.

The transmission curve based on a Monte Carlo simulation for BOREXINO's light concentrators can bee seen in figure 3.4.

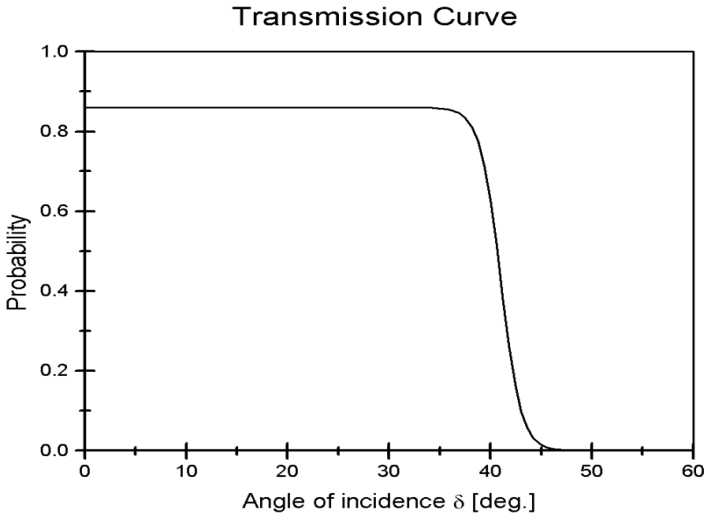

Figure 3.4: Angular acceptance for a BOREXINO light concentrator with a reflectivity $r = 0.86$ and a critical angle of acceptance $\delta_{crit} \sim 44°$. Figure from [36]

This angular acceptance is also part of the LENA simulation 3.3 as the same light concentrators were proposed for this experiment.

3.2.2 Hit probability

Although not important for the simulation itself the reconstruction of liquid scintillator detector events demand a hit probability. Assuming isotropic distribution of scintillation light the possibility of the photon emitted in the solid angle α of a particular PMT located at $\mathbf{r}_{PMT}$ is the hit probability $\Phi_{hit}(x,\alpha)$ from a spatial point $\mathbf{x}$. For a visualization see figure 3.5.

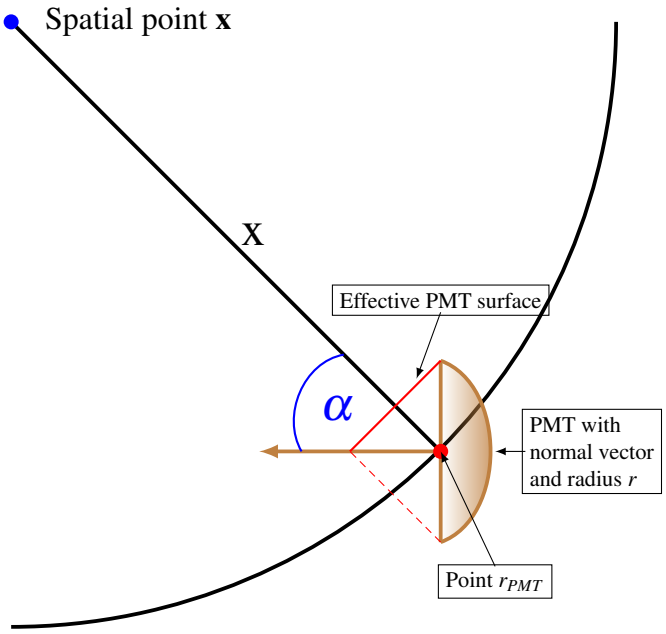

Figure 3.5: Schematic of the hit probability. The sphere around the spatial point $\mathbf{x}$ with radius x has a solid angle α to the at $\mathbf{r}_{PMT}$ located PMT's normal vector. The thick red line represents the effective PMT surface the solid angle α. The quotient between the effective PMT surface and the surface of the sphere with radius x is the hit probability for isotropic emitted light from point $\mathbf{x}$.

The hit probability can be approximated by the fraction of the detection surface of the PMT with radius r perpendicular to the vector $\mathbf{x}-\mathbf{r}_{PMT}$ (Effective PMT surface) and the spherical surface with radius $x = |\mathbf{x}-\mathbf{r}_{PMT}|$. Thus the hit probability is given by

$$\Phi_{hit}(x,\alpha) = \frac{r^2\cos(\alpha)}{4x^2} \tag{3.5}$$

This approximation is a far-field approximation and only valid for $x > r$.

3.3 LENA Simulation

The LENA Simulation is a simulation for Monte-Carlo events in the detector geometry of LENA. It is written in **C++**, is based on the **GEANT4** toolkit[4] [5] and uses the **ROOT** framework [8] for data storage. The LENA simulation especially enables the simulation of high energy cosmogenic muons in a liquid scintillator detector. For this work, multi-GeV muons were simulated to examine showering muons with the Wonsak Reconstruction introduced in section 3.4.

This section focusses on the simulated detector geometry and the PMT distribution as well as the general performance approximations in the LENA simulation. For a detailed description see [32].

LENA has an upright cylindrical structure which is shown in figure 3.6. The innermost of the detector is the actual neutrino target with the PMTs on its surface. The target has the height h_{tgt} and radius r_{tgt}. It is surrounded by a buffer where the support structure for the PMTs is located. The buffer medium with height h_{bfr} and radius r_{bfr} is liquid scintillator but separated from the target with an optical opaque foil. Target and Buffer are surrounded by a stainless steel tank with height h_{tnk} and radius r_{tnk}. A muon veto is installed on the cylinder barrel. It consists of a water tank with height h_{v} and radius r_{v} surrounding the detector tank. On its surface PMTs are installed forming a Water-Cherenkov-detector. The values for the different radii and heights in the simulation can be looked up in table 3.1

Table 3.1: Parameters of the LENA detector in the LENA simulation from [32]

Parameter description	Parameter	Value
Target Radius	r_{tgt}	14.0m
Buffer radius	r_{bfr}	16.0m
Tank radius	r_{tnk}	16.3m
Veto radius	r_{v}	18.3m
Target height	h_{tgt}	96.0m
Buffer height	h_{bfr}	100.0m
Tank height	h_{tnk}	100.6m
Veto height	h_{v}	100.6m

[4] Version 4.9.6. Patch 02

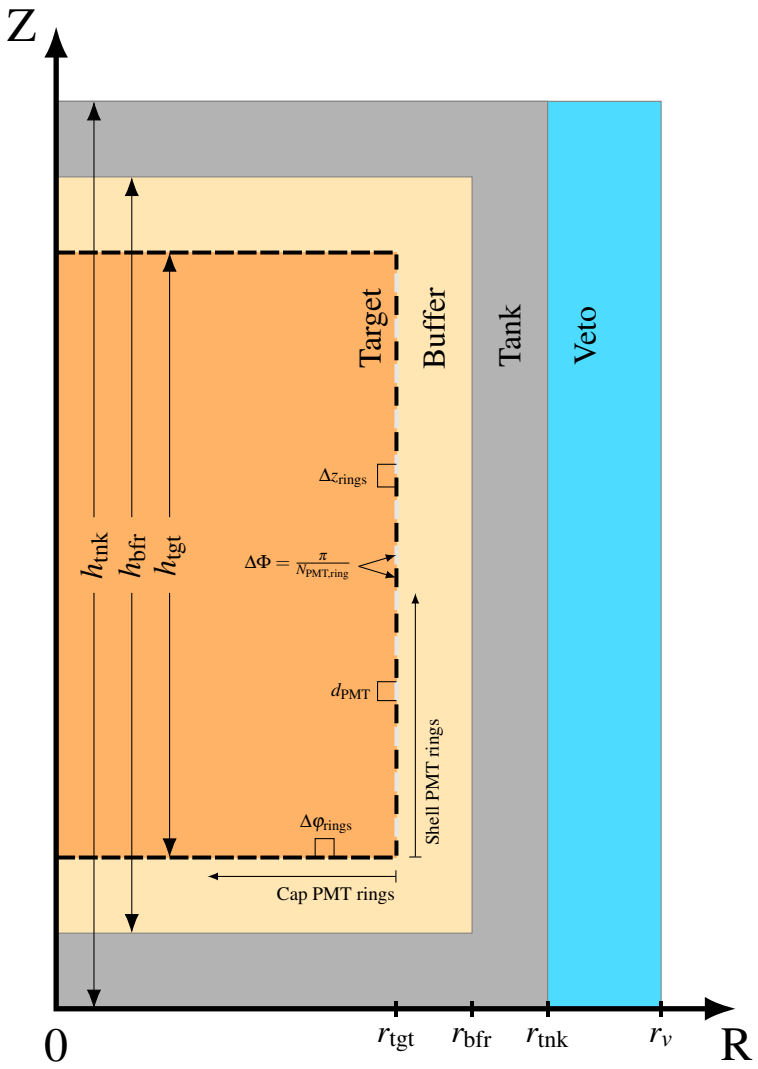

Figure 3.6: Visualization of the upright LENA detector with its geometric parameters listed in table 3.1. The shell PMT-rings are successively shifted by the angle $\Delta\Phi$ and are depicted in black (even PMT-ring) and gray (odd PMT-ring).

Furthermore the PMT distribution around the target volume is of special interest. There is a total number of N_{PMT} PMTs distributed over the targets surface with $N_{\mathrm{PMT,shell}}$ on the detector barrel and the rest on the caps. The PMTs on the detector barrel form N_{ring} rings of PMTs with $N_{\mathrm{PMT,ring}}$ PMTs per ring. Two adjacent rings are shifted by an angle of $\Delta\Phi = \pi/N_{\mathrm{PMT,ring}}$ which is half of the angle between two PMTs on the same ring. This creates even and odd PMT rings, which are coloured black and gray respectively in figure 3.6. The distance between two PMT rings on the cylinder barrel is $\Delta z_{\mathrm{rings}}$. The cap PMTs are installed in concentric circles around the center of the cap.

Furthermore, the radial distance of two adjacent cap PMT rings is $\Delta\varphi_{\text{rings}}$. The designated values can be seen in table 3.2.

Table 3.2: Parameters of the LENA detector PMTs in the LENA simulation from [32]

Parameter description	Parameter	Value
Total PMTs	N_{PMT}	30542
PMTs on shell	$N_{\text{PMT,shell}}$	26640
PMTs per ring	$N_{\text{PMT,ring}}$	144
Total PMT rings	N_{ring}	185
Distance of adjacent shell PMT rings	Δz_{rings}	51.9cm
Radial distance of adjacent cap PMT rings	$\Delta\varphi_{\text{rings}}$	55.1cm
PMT diameter	d_{PMT}	51.0cm

3.3.1 Basic approximations used

The physical processes of a particle surpassing the LAB and photon interactions such as absorption and Rayleigh scattering as well as the Cherenkov light process are covered in GEANT4. Further coverage of isotropic scattering and a implementation of the scintillation process is part of the LENA simulation software [32].

Simulation of muon events can be a time-consuming task. To shorten the simulation time some approximations were made without distorting the outcome drastically. These approximations are taken from [32].

The buffer medium is simulated as liquid scintillator with a light yield $L = 0\text{MeV}^{-1}$ to mimic the opaque foil between the buffer and the target without loosing the properties of the buffer regarding surpassing particles.

The Cherenkov light process was disregarded. This is justified by its share of a few percent of the actual scintillation light. Furthermore, wavelength dependent effects were ignored. Thus all photons travel with the phase velocity $v = c_0/n$ with the refractive index n of the liquid scintillator. Therefore, the optical model is a crude approximation.

Additionally the light yield of the liquid scintillator located in the target is set to 2000MeV^{-1} which is about a fifth of the liquid scintillator mixture used in LENA. This is compensated by setting the quantum efficiency of the PMTs from 20% to 100% as it is time consuming to simulate photons which are discarded in 80% of the cases because the quantum efficiency is 20%.

The PMTs itself are simulated as flat disks. A Look-Up-Table (LUT) like in figure 3.4 is used to determine if a photon is accepted. This costs less time than a complex simulation of light concentrators in front of the PMT.

In the end the accepted photons at a particular PMT are stored with their hit-time t, which is smeared with δt from a normal distribution in the interval $[0, \Delta T]$ with $\Delta T = 1\text{ns}$. This covers up some of the effects regarding the uncertainties of PMTs, although pre- and after-pulses, as well as the dark current, are ignored.

The simulated data does not cover all the physics of an muon event but is a good enough approximation to test the reconstruction method in section 3.4.

3.4 Wonsak-Reconstruction

The Wonsak-Reconstruction is a new approach to topological event reconstruction in liquid scintillator detectors. Whilst the algorithm was developed by Björn Wonsak [46], a general object oriented C++ software package was implemented by Sebastian Lorenz [32], thus making the algorithm highly adaptable to all kind of liquid scintillator detector geometries and Monte-Carlo simulations. Currently the code is optimized for the LENA experiment but a further optimization for the use in the JUNO experiment is in progress.

The following section will shortly describe the reconstruction algorithm based on [32].

With its spatial resolution of the energy loss $dE/d\mathbf{x}$ it can be used for a muon background rejection in LSc detectors. Furthermore, a non full detector veto can be given for showering muons or muon bundles, both highly related to the creation of cosmogenic radioisotopes. This can be an exceptional tool for the upcoming JUNO experiment with a rate of $0.5s^{-1}$ for showering muons and muon bundles in 10% of all muon events [7] (For detailed insight see section 2.3.3).

The principle of the algorithm is to calculate the spatial number density of emitted photons. Thus it gives access to a $dE/d\mathbf{x}$ estimation of the detector event.

The basic idea relies on two assumptions:

1. The particle traverses the detector on a straight track with speed of light c_0.

2. A reference point $\mathbf{r}_{ref}$ with a reference time t_{ref} for the particle is known. The reference point can be any point on the particle track. The input can be given by the particle vertex using the backtracking algorithm [34].

In a liquid scintillator detector event the data is given by photon hits with a designated time $t(\mathbf{x})$ on a PMT with a designated position $\mathbf{r}_j$. This leads to equation 3.6.

$$t(\mathbf{x}) = t_{ref} + \frac{|\mathbf{x} - \mathbf{r}_{ref}|}{c_0} + \frac{|\mathbf{r}_j - \mathbf{x}|}{\frac{c_0}{n}} \tag{3.6}$$

The time $t(\mathbf{x})$ of a photon hit on the PMT with position $\mathbf{r}_j$ is the reference time t_{ref} plus the time the particle travels from the reference point $\mathbf{r}_{ref}$ to the point $\mathbf{x}$ in the detector volume with speed of light c_0 plus the time the photon travels from point $\mathbf{x}$ to the position $\mathbf{r}_j$ of the PMT with its speed $\frac{c_0}{n}$ in the liquid scintillator with refractive index n (See for a visualization 3.7). Therefore point $\mathbf{x}$ is the emission point of the photon.

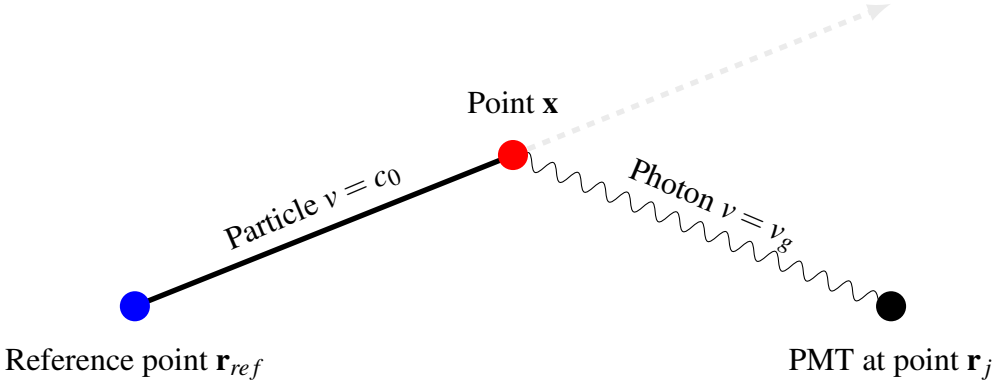

Figure 3.7: Visualization of equation 3.6

The solution for the mathematical set of $\mathbf{x}$ of a single PMT-hit is a three dimensional drop-shaped surface around the PMT (See 3.9 black line). Though this is the principle of the reconstruction method the formula does not take into account the experimental environment. The basic approach is the smearing of the drop shaped surface with the time distribution (See figure 3.8) caused by the scintillation process [5] with a Gaussian of 1ns deviation representing the time uncertainty of the PMTs (See 3.9 left).

[5]The excited state of the scintillator decays exponentially yielding a photon

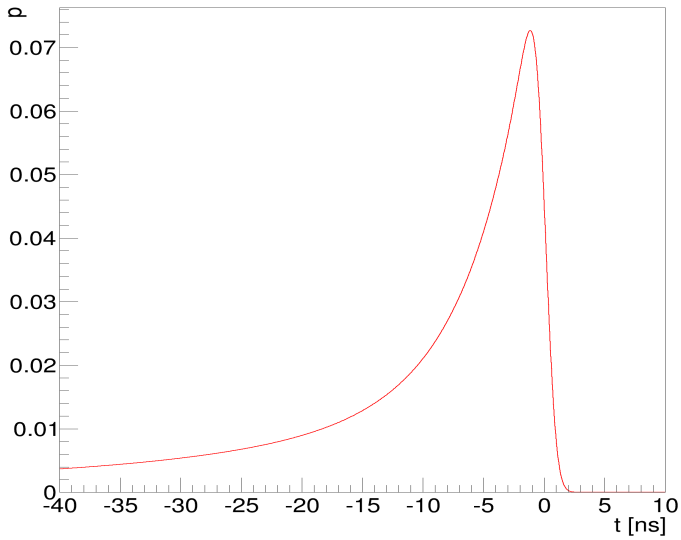

Figure 3.8: Time distribution of the scintillator decay components with a gaussian of 1ns deviation representing the uncertainty of the PMTs. Time t on the x-axis and emission probability p on the y-axis.

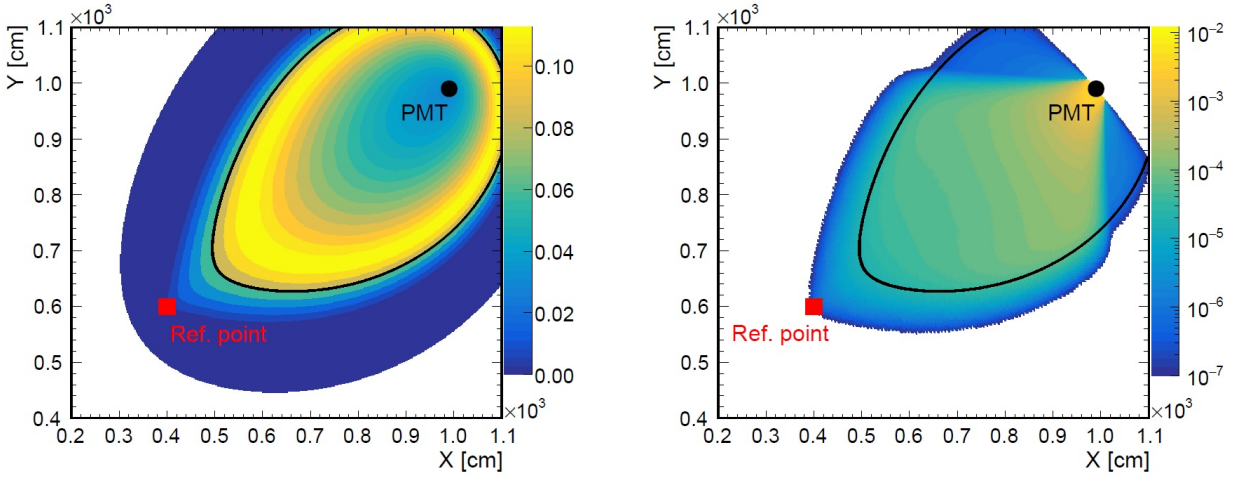

Figure 3.9: **left:** Drop shaped surface of equation 3.6 (sharp black line) smeared with the time distribution 3.8. **right:** left surface with taking hit and angular acceptance of the PMT as well as the survival probability of a photon into account. Both figures are unnormalized. Figure from [32].

Furthermore the photon detection probability for each PMT is dependent on the location **x**. This is caused by the hit and angular acceptance of the particular PMT as well as the survival probability of a propagating photon in the liquid scintillator detector. The effect of both time and spatial deviations are shown in figure 3.9 right. This gives a scalar field $\Phi^*_{j,k}(\mathbf{x})$ of photon emission probability for a PMT j and a single photon hit k of PMT j. Being the information of a sole detected photon, this scalar field has to fulfil the normalization condition.

$$\int_{V_{LSc}} \Phi^*_{j,k}(\mathbf{x}) d\mathbf{r} = 1 \tag{3.7}$$

The spatial number density of detected scintillation photon emissions is the superposition of all hit PMTs j with all their hits k

$$\hat{\Gamma}_{det}(\mathbf{x}) = \sum_{j=1}^{N^{hit}_{PMTs}} \sum_{k=1}^{N_{hits,j}} \Phi^*_{j,k}(\mathbf{x}). \tag{3.8}$$

Note that this is the spatial number density of detected scintillation photon emissions $\hat{\Gamma}_{det}$. To get the spatial number density of emitted scintillation photon emissions $\hat{\Gamma}_{em}$, $\hat{\Gamma}_{det}$ is divided by the local detection efficiency $\varepsilon(\mathbf{x})$. $\varepsilon(\mathbf{x})$ is the sum over all PMT detection probabilities $P_{det,j}$ [6]. Thus this results in

$$\varepsilon(\mathbf{x}) = \sum_{j=1}^{N_{PMT}} P_{det,j}(\mathbf{x}). \tag{3.9}$$

Unfortunately the computed $\hat{\Gamma}_{em}$ is widely spread in the detector and only reflects the real emitted light Γ_{em} if reduced to the true events topology.

To further enhance the $\hat{\Gamma}_{em}$ of the reconstruction algorithm it is necessary to note that the light emission is dependent on the events topology. Thus the light signals are correlated. This can be utilized by making the reconstruction an iterative process. Therefore the prior iteration is normalized and used as a probability mask for a further iteration. Typically 21 iterations result in a good estimation of the spatial number density of emitted photons with a binning of 12.5cm. The probability mask serves as a pre reconstruction knowledge of the event by giving a normalized probability field $M(\mathbf{x})$ which is taken into account as a factor when calculating the $\Phi^*_{j,k}$. Because this method is prone to self enhancement errors a binary probability mask

[6] including unhit PMTs

can be extracted from the probability field $M_{binary}(\mathbf{x})$ by setting a threshold a.

$$M_{binary}(\mathbf{x}) = \begin{cases} 1 & \text{if } \Phi^*_{j,k} \geq a \\ 0 & \text{else} \end{cases} \tag{3.10}$$

Further implementations of a probability mask are explained in section 4.5.

Nonetheless there are still particular effects with need of improvement. It is still assumed that all detected light is scintillation light following the rules of equation 3.6. Thus it neglects the Cherenkov-light. Furthermore events produce a huge amount of scattered light. If scintillation light is scattered it loses its timing-information due to its untrackable path through the detector. Thus the photon does not satisfy equation 3.6. A statistical approach to distinguish between direct and scattered light is discussed in section 4.3. In addition the computation time of the algorithm is tremendous when iterating several times over high energy events. However the algorithm can be sped up using parallelization with multiple CPUs or GPUs [41] and by additional code optimization.

3.4.1 Raw Wonsak Reconstruction

Sometimes the Wonsak reconstruction algorithm leaks in robustness for multi-GeV muons (See section 4.2). Another approach is to completely ignore normalizations in the reconstruction algorithm to estimate a event topology. In return the exact spatial energy distribution information is lost. Only relative statements regarding the energy distribution can be done. Thus a reconstruction is done with the drop shapes of 3.8 which are presented in the unnormalized form. This counteracts the overvaluation of near field of the PMTs. The result can be utilized as a probability mask for a further reconstruction, if a topology can be extracted.

3.5 Other reconstruction methods for event topologies

In this section other tracking and reconstruction methods are presented shortly as they are indispensable for the construction of event topologies (See section 4.5). These methods are very fast tools in comparison with the rough reconstruction of section 3.4.1.

3.5.1 The Opera target tracker

The Oscillation Project with Emulsion tRacking Apparatus (OPERA) target tracker [3] is reused in the JUNO experiment and is a reliant source for the reconstruction of particle tracks entering the detector from above. It consists of 6.86m long, 10.6mm thick and 26.3mm wide scintillator strips which contain wavelength-shifting (WaveLength Shifting (WLS)) fibres to enhance the light transport to their ends. The strips are readout with 64-channel photodetectors at their ends. Thus 64 strips are merged into a bundle which is called a basic module [3]. A schematic view of a scintillator strip can be seen in figure 3.10a.

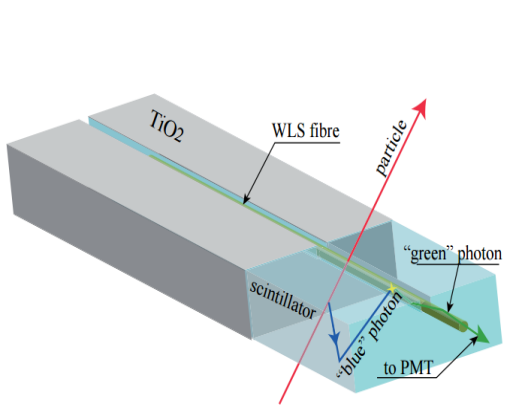

(a) Scintillation strip with a TiO_2 reflective shell and a possible event reaction.

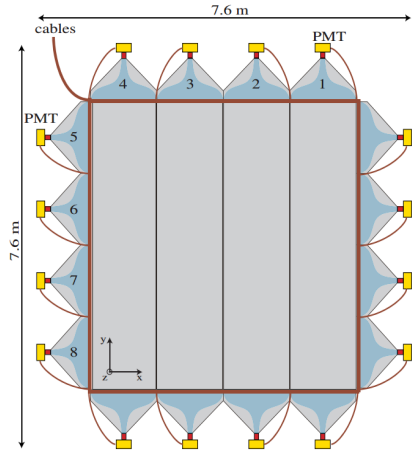

(b) A strip wall consisting out of 8 basic modules.

Figure 3.10: Schemes of a scintillation strip and the assembly of basic scintillation strip modules (scintillation strip wall) to access a xy-reconstruction of surpassing particles. Both figures from [3].

These basic modules are assembled together as four, covering an area of $6.7 \times 6.7\,\mathrm{m}^2$. In addition these four-pieces are layered vertically and horizontally to provide an xy-information with two consecutive four-pieces which are then called a tracker wall (See figure 3.10b). The z-information is derived with consecutive tracker walls. The OPERA target tracker contains

62 tracker walls which cover 98.5% of the $6.7 \times 6.7\,\mathrm{m}^2$ area [3]. The reconstruction is based on the one-dimensional spatial information of each strip provided by the signal times of both strip ends. The whole target tracker provides enough three-dimensional points to fit the particle track.

3.5.2 The Cherenkov detector

The outter water pool of JUNO is used as a Cherenkov detector. With 800 PMTs on the outer barrel, 200 PMTs on the top and bottom cap as well as 800 PMTs on the central detectors surface pointing away from the target, JUNOs Cherenkov detector allows a track resolution within 1.5m for each spatial direction [4]. The principle is to use the only in a particular angle θ_c around the particle track radiated Cherenkov light to reconstruct the Cherenkov-cone around the particle. The track direction can be extracted using a maximum likelyhood fit including the particles vertex, direction and impulse [44] which is necessary due to the multi factor dependence of the Cherenkov cone.

3.5.3 First-Hit-Reconstruction in liquid scintillator detectors

A similar approach to 3.5.2 can be done with the first photon surfaces of a particle in liquid scintillator. A sketch of the first photon surfaces is shown in figure 3.11. The envelope of all first photon surfaces can be reconstructed in the detector with the PMTs first hits. Due to the enevelope's asymetric shape the track aswell as the direction can be well calculated. A likelyhood fit can be made based on the particles vertex and direction aswell as the start time and kinetic energy as with the Cherenkov light [26].

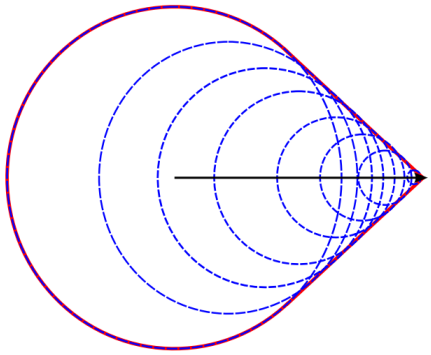

Figure 3.11: The black arrow indicates the particle's track. The dashed blue lines represent the first photon surfaces and the red line is the envelope of all first photon surfaces. Figure from [26].

4 Showering muons in liquid scintillator detectors

The background of cosmogenic muons leads to a production of cosmogenic isotopes which yield the same coincidence as the anti electron neutrino, which is to be detected in the JUNO experiment. The veto strategies in section 2.3.3 depend on the reconstruction of these muons, especially showering muons and muon bundles. The goal of this thesis is to examine showering muons with the Wonsak reconstruction algorithm and proof the ability to reconstruct those events, providing a solid base for an efficient muon veto. In this chapter the simulation of muons which most likely produce a muon shower is described in section 4.1. The problematic of high energy muons reconstructed with the Wonsak reconstruction algorithm is explained in section 4.2. The further improvements of the algorithm regarding the probability mask in section 4.5 and a statistical consideration of scattered light in section 4.3, which were part of this work, are presented afterwards. Finally, the results of the improved reconstruction algorithm are outlined in section 4.7. The examination of showering muon events regarding the possibility to locate the muon shower is presented in section 4.8.

4.1 Creating showering muons with LENA-Simulation

The LENA-Simulation (see section 3.3) uses the command line interface and can be controlled by a macro in the batch mode [35].

The utilized macro setup is divided into three parts. The *physics.mac* macro contains the settings for the physics processes. Furthermore the *geometry.mac* macro describes the detector geometry and the PMT distribution on the target volume. Lastly the *template.mac* macro combines the former macros and sets the file specifications like the filename and the quantity of successive simulated events.

The macros can be found in appendix 6.1 with batch comment lines giving a short introduction to the commands, as not all of them will be covered in this chapter.

The goal was to maximize the possibility for the muon to create a shower. This can be done

in the simulation by maximizing the target volume surpassed by the muon by adjusting its track. Furthermore, the muon needs enough energy to create a shower at any time in the target volume. Therefore, muons with enough energy to surpass the whole detector on the longest possible way are preferred to create a showering muon event with the LENA simulation. Thus, the simulated muons start at the edge of the upper detector cap. The position of the particle gun $\mathbf{x}_{gun}$ (start point of the muon) is

$$\mathbf{x}_{gun} = \begin{pmatrix} 1000 \\ 830 \\ 4600 \end{pmatrix}. \tag{4.1}$$

The direction points through the origin of the coordinate system located in the detector center onto the opposing side of the detector. The vector for the gun direction $\mathbf{v}_{gun}$(muons direction) therefore is

$$\mathbf{v}_{gun} = \begin{pmatrix} -0.209 \\ -0.174 \\ -0.962 \end{pmatrix}. \tag{4.2}$$

Finally the energy has to be large enough to guarantee a full transition through the detector on this path. According to section 2.3.3 the differential energy loss $dE/dx|_{\mu}$ through the ionisation of a muon is 1.43 MeV/cm (minimal ionisation).

Thus, the needed energy threshold E_t calculates to

$$E_t = 2 \cdot |\mathbf{x}_{gun}| \cdot dE/dx|_{\mu} = 13680\,\text{MeV} \approx 14\text{GeV}. \tag{4.3}$$

In fact, a muon needs an initial energy to trigger a shower. Therefore high energies are needed. To compensate between the probability of creating a shower and the duration of the simulation all energies were chosen in the interval $[20,40]$ GeV. This rough estimation created enough showering muon events. Therefore, the threshold energy E_t is just the minimum energy needed.

An event with these parameters is shown with the LENA event display in figure 4.1.

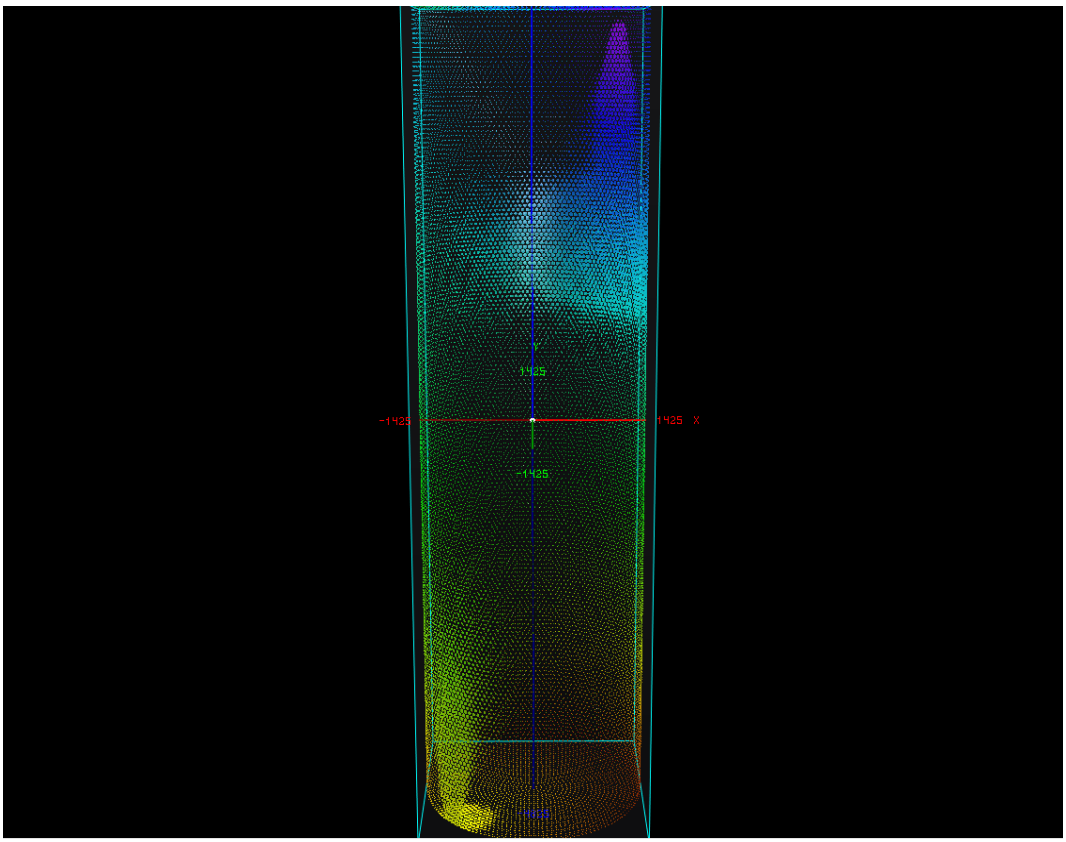

Figure 4.1: LENA event display visualizing the photon hits on the PMTs from a muon with kinetic energy $E_{kin} = 40\text{GeV}$, start position $\mathbf{x}_{gun}$ from equation 4.1 and direction $\mathbf{v}_{gun}$ from equation 4.2. PMTs with photon hits are colourized. The colours represent the time of flight corrected hit times with respect to the barycenter . The color code ranges between blue $\sim 0\,\text{ns}$ and red $\sim 400\,\text{ns}$. The total area of the PMT panels represents the charge of the PMTs which is the quantity of detected photon hits. The event display source code originates from [26].

After the simulation the data gets processed furthermore using the Dataprocessing algorithm. The general idea is to put the data into a more suitable format with all photon hits assigned to the PMTs they encountered [26] . This processed format is accepted as input for the Wonsak reconstruction algorithm.

4.2 Problems of high energy muon reconstruction

The scalar field of spatial density of deposited energy Γ_{em} computed by the Wonsak reconstruction algorithm is stored in a three-dimensional histogram with values of double precision. The software package developed by Sebastian Lorenz [32] produces an output for contained muons[1], which is consistent with the Monte Carlo (MC)-Data. A reconstructed muon can be seen in figure 4.2.

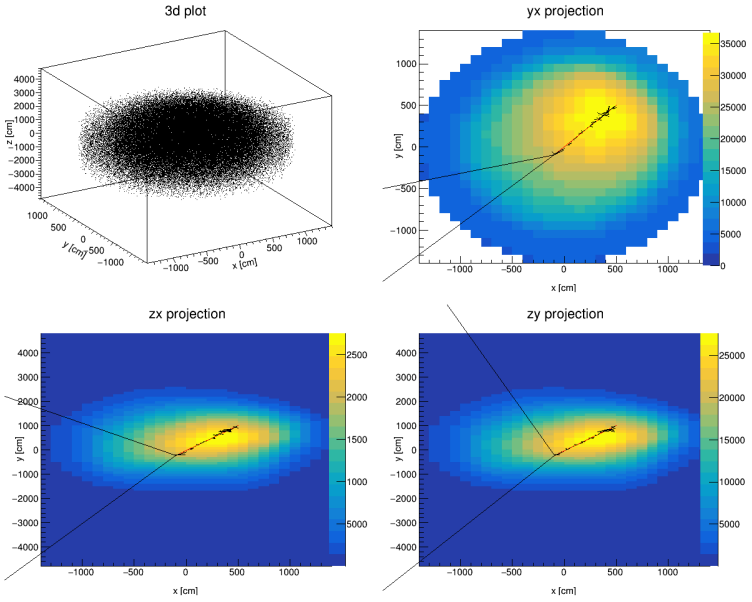

Figure 4.2: Reconstruction of a 3 GeV muon event starting and ending in the detector volume. Thus speaking of a contained event. The reconstruction was done with one single iteration. Thus the spatial density of emitted photons is widely spread. Nonetheless this is a good approximation of the event's topology. The red line indicates the primary muon and the black lines the secondary particles (mostly electrons due ionization) of the MC-Data corresponding to the event.

Although the reconstruction works well for these events especially if they are contained, the output shows signs of weakness when the muons pass areas near the PMTs. A 20GeV muon surpassing the detector in the xy-plane is depicted in figure 4.3. These events were chosen to test the new approach of the reconstruction algorithm in section 4.7.

[1]The full track of the muon is in the target volume

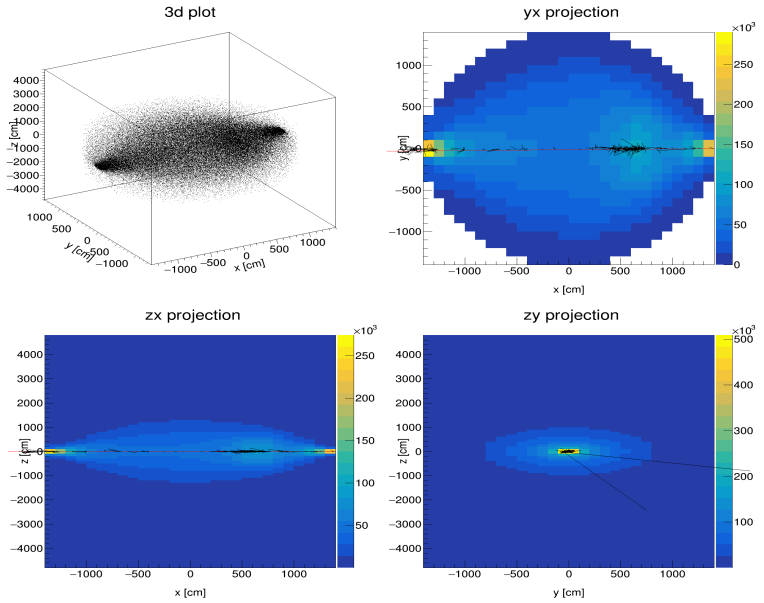

Figure 4.3: Reconstruction of a 20 GeV muon surpassing the detector in the xy-plane. The result is distorted by the energy deposition near the PMTs.

The effects of the spatial energy density being drawn to the targets exterior surface (or to the PMTs) can be explained with scattered light. Scattered light occurs through different effects explained in section 3.1.2. In the following sections light which causes a PMT signal will be referred to as scattered or direct light when it reaches the PMT with or without a scattering process respectively. Multi-GeV energy events yield huge amounts of light. Taken the simulated light yield of $L = 2000/\text{MeV}$ and the energy loss $E_t = 13680\,\text{MeV}$ of a muon surpassing the whole detector due to ionization calculated in equation 4.3, the amount of produced photons $n_{photons}$ is

$$n_{photons} = L \cdot E_t = 27360000. \tag{4.4}$$

Note that the quantum efficiency of the PMTs is set to 100% to compensate the five times lower light yield. In addition a possible shower, much more likely in the GeV muon energy range, would deposit another $1 - 10\text{GeV}$ [23] of showering energy. The near field of the PMTs enhances these problems drastically, because it gets huge amounts of light. Only a few PMTs near the entry point and exit point of the muon distort the result of the reconstruction algorithm in the first iteration (See figure 4.3). Another problem regarding the reconstruction is the scattered light, which causes a deterioration of the reconstructed spatial number density of emitted photons due to false information regarding equation (3.6). The time the photon hit the PMT and its origin are not connected for scattered light. In the far field, scattered light

leads to a widening of the topology of the reconstruction result. Scattered light originating from the far field does not follow a special pattern. Therefore, a drastic change of the topology of the event is not caused. However, the near field yields more drastic problems regarding scattered light. A possible event could pass the detector between two PMTs in a way that one PMT gets much direct light and the other PMT does not (see figure 4.4). Actually both PMTs see light. One mostly due to direct light and one due to scattering. Thus one PMT gets huge amounts of false information and together with other PMTs deteriorates the reconstruction outcome.

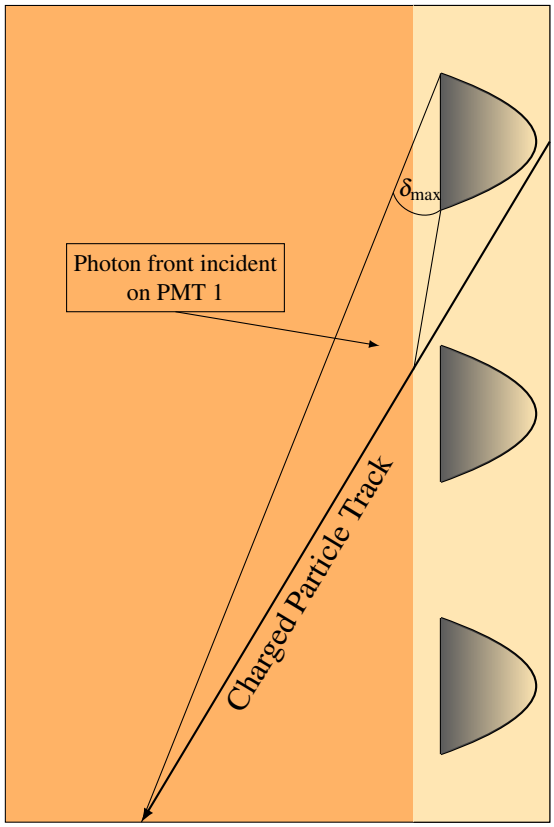

Figure 4.4: A charged particle enters the detector target volume (orange) between two PMTs in the buffer volume (light orange). The three PMTs are PMT 1,2 and 3 seen from the top. Whilst the PMT 2 and 3 get much direct light, the incident photon front hits PMT 1 under an angle $\delta < \delta_{max} < \delta_{crit} \approx 48°$ an therefore sees close to zero direct light, although getting a huge amount of photon hits due to scattering.

Thus, high energy muons demand another approach to distinguish scintillation light based onto their probability to be scattered. A statistical approach within the Wonsak Reconstruction and its implementation in the reconstruction framework is discussed in the following section 4.3.

4.3 Correcting scattered light

The Wonsak reconstruction algorithm uses all photon hits as equal information, but some photons are statistically less likely to be direct light.

The basic idea demands some preknowledge:

1. The events topology is roughly known. The algorithm demands a probability mask.

2. The probabilities of scattered light $p_{\text{scat}}(t)|_{i,\mathbf{x}_{\text{em}}}$ and direct light $p_{\text{dir}}(t)|_{i,\mathbf{x}_{\text{em}}}$ for all PMTs (index i) and time t after emission time $t_0 = 0$ from all possible emission points $\mathbf{x}_{\text{em}}$ in the detector are known.

For muon events the particle track can be provided by a former reconstruction of a muon tracker, the Cherenkov veto or a robust reconstruction with the same algorithm which are covered in section 3.5. A possible way to get access to an approximate topology based on the track of the muon, which is called the probability mask in the Wonsak reconstruction, is covered in section 4.5.

The probabilities for scattered and direct light can be simulated and stored into LUTs[2]. The possible emission points are reduced to a reasonable binning to compromise simulation time and data storage. Furthermore the symmetric detector geometry can be used as an advantage.

The probability for direct light is a probability density function $\Phi_{photon}(t,\mathbf{c})$ of the photon emission of the detector's target material calculated with equation (3.2) delayed by the time of flight t_{tof} from emission point $\mathbf{x}_{\text{em}}$ multiplied with the probability of reaching the PMT i from emission point $\mathbf{x}_{\text{em}}$. The probability of reaching a PMT is calculated as a product of the attenuation probability $\Phi_{dir}(x,L)$ (see subsection 3.1.2), the angular acceptance $\Phi_{aa}(\alpha)$ (see subsection 3.2.1) and the hit probability $\Phi_{hit}(x)$ (see subsection 3.2.2). Distance x, incident angle α as well as t_{tof} can be derived from emission point $\mathbf{x}_{\text{em}}$ and PMT i. Furthermore the components $\mathbf{c}$ and the attenuation length L can be precisely measured for the scintillator and are considered as constants. Thus the direct light probability $p_{\text{dir}}(t)|_{i,\mathbf{x}_{\text{em}}}$ can be expressed using

$$p_{\text{dir}}(t)|_{i,\mathbf{x}_{\text{em}}} = \Phi_{\text{photon}}(t - t_{\text{tof}}) \cdot \Phi_{\text{dir}}(x) \cdot \Phi_{\text{aa}}(\alpha) \cdot \Phi_{\text{hit}}(x,\alpha). \tag{4.5}$$

The probability for scattered light needs to be simulated. The general idea is to emit a large amount of photons isotropically at an emission point $\mathbf{x}_{\text{em}}$ and calculate their way through the detector. Scattered photons get tagged as scattered upon their first scattering process. The probability of scattered light from an emission point $\mathbf{x}_{\text{em}}$ is the number of scattered photons

[2]Look up tables (LUTs) are data packets which contain data which is independent of the event

$n_{p,scat}(t)|_{i,\mathbf{x}_{\text{em}}}$ detected on a PMT i divided by all detected photons $n_p(t)|_{i,\mathbf{x}_{\text{em}}}$ on a PMT for a time interval $t_a < t < t_a + \Delta t$, where Δt is the bin size. Thus the scattered light probability can be written as

$$p_{\text{scat}}(t_a)|_{i,\mathbf{x}_{\text{em}}} = \frac{n_{p,scat}(t_a)|_{i,\mathbf{x}_{\text{em}}}}{n_p(t_a)|_{i,\mathbf{x}_{\text{em}}}} \text{ for } t_a < t < t_a + \Delta t \tag{4.6}$$

For comparability the binning of the direct light probability LUT is set the same as the scattered light LUTs binning.

The scattered light probability is not given by $p_{\text{scat}} = 1 - p_{\text{dir}}$ because direct light from a spatial emission point $\mathbf{x}_{\text{em}}$ does not imply the scattered light being from the same point $\mathbf{x}_{\text{em}}$. Figure 4.5 depicts the fact that given a topology there are possible origins for direct light calculated by equation 3.6 (black line) and possible origins for scattered light (red area). Note that the whole area in the drop shape is a possible origin for scattered light, but the gray topology reduces this volume to the red area. Two exemplary photons are drawn for a direct hit (black arrow) and a scattered hit (dashed arrow) with the same hit time. Therefore the emission points do not coincide and thus light being scattered or not does not follow a binomial distribution. Thus an statistical estimation over all emission points in the topology is needed.

These probabilities for direct and scattered light are necessary to compute a total direct light probability. The statistical approach evaluates the possibility of the photon hit being correlated to the given topology. This is called the *total direct light probability* $P_{tot,k}$ of a photon hit k.

The scattered light algorithm (SLA) calculates the direct light probability $p_{dir,j}$ and scattered light probability $p_{scat,j}$ for each unique hit k for each bin j in the event topology with respect to the corresponding PMT. These probabilities are added up and form the total direct light probability $P_{tot,k}$ for the photon hit k with equation (4.7).

$$P_{tot,k} = \frac{\sum_j p_{dir,j}}{\sum_j p_{dir,j} + \sum_j p_{scat,j}} \tag{4.7}$$

Thus the algorithm computes the possibility of the photon hit correlated directly with the event's topology. This information is stored and the further contribution of the photon k is weighted with its new probability of being direct light $P_{tot,k}$.

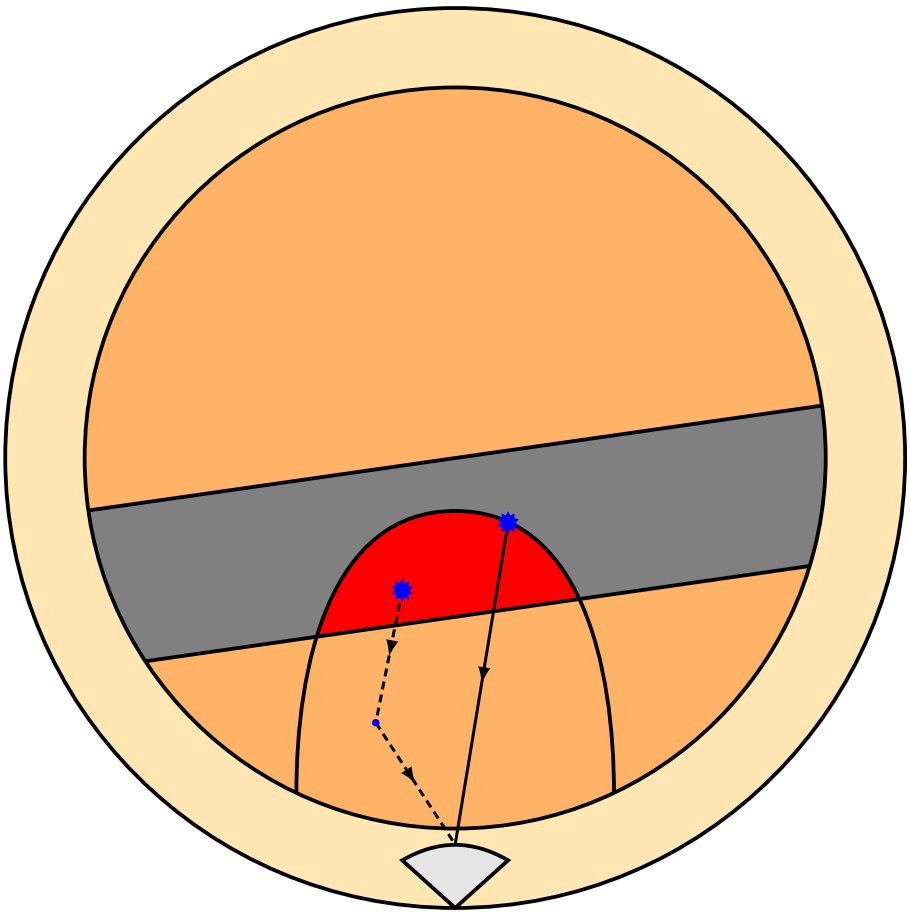

Figure 4.5: Visualization of the scattered light algorithm. The xy-projection of the LENA detector with the target volume (orange) and a PMT (light gray) in the buffer volume (light orange) with an event topology (gray). The possible origins for a hit calculated with equation 3.6 on the PMT is shown by the black curve around the PMT. The red area marks the possible origins for scattered light. Although the whole area in the drop shape is a possible origin for scattered light, the topology reduces it to the red area. Two exemplary photons are drawn for a direct hit (black arrow) and a scattered hit (dashed arrow) with the same hit time.

The topology is given by the probability mask in the reconstruction algorithm. The probability mask is a scalar field, which represents an in advance topology of the event. If the probability mask is binary, equation 4.7 can be applied. If the probability mask is not binary and thus already yields information of the spatial number density of emitted photons additional to the topology, equation 4.7 needs a correction. This is done by including the probability M_j of the bin j of the probability mask in equation 4.7, thus giving equation 4.8.

$$P_{tot,k} = \frac{\sum_j M_j p_{dir,j}}{\sum_j M_j p_{dir,j} + \sum_j M_j p_{scat,j}} \tag{4.8}$$

4.4 Implementation of the scattered light algorithm for LENA

This section covers the implementation of the direct and scattered light LUTs as well as the algorithm itself into the reconstruction framework.

4.4.1 Scattered light LUTS

The scattered light LUTs were simulated in circular segments on various heights in the upper half of the detector. Computing LUTs with high statistics is a time consuming task. Therefore much effort lies on the reduction of the amount of the emission points of the LUT, which are spatial points in the detector volume simulated as an origin of photons. All following reductions regarding the emission points are justified by the symmetry of the detector. The general idea is to find a corresponding LUT emission point for every bin (spatial, cubic segment of the detector volume) in the SLA and shift the PMT distribution in a way that the bin overlaps the emission point in the LUT. The consequence is a shifting of all PMT IDs. Thus a transformation rule is derived from the relative position of the bin to the emission point, which is then applied to all PMT IDs.

First the focus for the reasoning of the LUTs lies on a particular PMT ring, followed by the z-coordinate in the detector.

The circular segments have an angle of $\alpha_{seg} = 1.25^\circ$ and are placed to the right of a PMT in the ring. For a consistent numbering of the PMT ring, the interval $[0, N_{\text{PMT,ring}}]$ is used. The reasoning behind this choice is the PMT distribution being invariant to a rotation of an angle $\delta = n \cdot \Phi$ with n being an non-negative integer. This is due to the fact that one PMT-ring in the LENA detector has $N_{\text{PMT,ring}} = 144$ PMTs per ring, thus giving $\phi = 360^\circ/144 = 2.5^\circ$. Figure 4.6 depicts the general idea behind a transformation in a PMT ring. The red bin near PMT i corresponds to the emission point (yellow star) relative to PMT 0. Therefore the PMT ring gets turned until PMT i overlaps PMT 0. This is expressed by the simple equation 4.9. j denotes the PMTs in the interval $[0, N_{\text{PMT,ring}} - 1]$. If the equation goes out of bounds of the interval, 144 is added.

$$j' = j - i \tag{4.9}$$

The blue bin is on the left side of PMT i. After the ring gets turned, the ring has to be inverted to match the blue bin and the emission point. This means the nth order right and left to the PMT 0 change places for all orders. This is described by equation 4.10.

$$j' = i - j \tag{4.10}$$

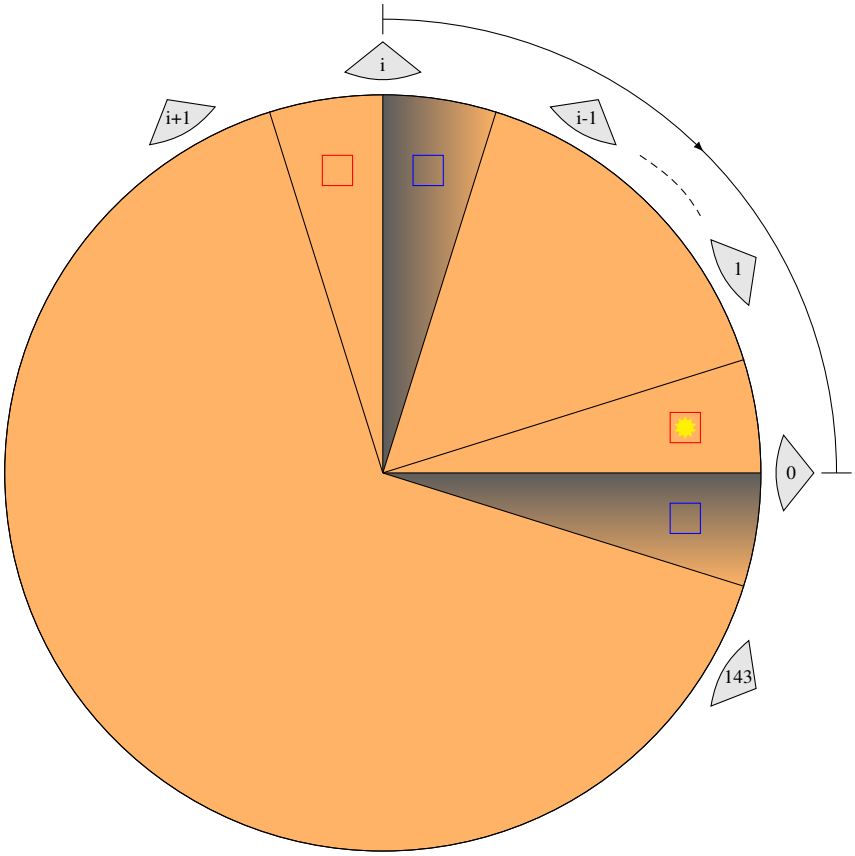

Figure 4.6: This figure depicts the transformation within a PMT ring. The red bin is to the right of the PMT ID i and matches the right oriented LUT at PMT ID 0 with its emission point (yellow star). Thus all PMT IDs get transformed with equation 4.9. The blue bin is to the left of PMT ID i and does not match the emission point. Therfore all PMT IDs get transformed with equation 4.10.

The final LUT ring consists out of $n_{em} = 81$ emission points for 27 radial bins of 50 cm and 3 circular segment fractions of 0.5°.

Secondly, the z-distribution of the LUT rings is of interest. For this the PMT ring IDs are used as they quantize the z-axis. The LENA detector has N_{ring} PMT rings in the interval $[0, N_{\text{ring}} - 1]$. The first approach is to neglect the lower half of the cylindrical detector because it is symmetric to an area perpendicular to its z-axis. The central PMT ring has the ring ID

92. Thus the rings which need a LUT are of the ID $k \geq 92$. The rings with an ID $k < 92$ are assigned to their counterpart on the upper half following the transformation in equation (4.11).

$$k' = 184 - k \tag{4.11}$$

With this assignment the ring IDs of all PMT rings change too following equation (4.11). This effectively is the mirroring of the detector on the xy-area located at the center of the detector.

Furthermore, the number of LUTs for the PMT rings of the upper detector half can be reduced, because no drastic changes were found between two LUTs of consecutive PMT rings. If the PMT ring does not have a LUT, the nearest ring ID having a LUT is chosen and the distance d in the unit of PMT rings is calculated. This is done after transformation (4.11) for ring IDs $k < 92$. Thus the additional transformation rule is given by equation (4.12) $[0, N_{\text{ring}} - 1]$.

$$k'' = k' + d \tag{4.12}$$

The problem occurring during the use of transformation rule (4.12) is the ring ID going out of bounds of the interval $[0, N_{\text{ring}} - 1]$. To account for this relative distances are used. The principle is the invariance of PMT rings with equal relative distances. A simple example of the upper half of the detector can be seen in figure 4.7. The red bin at ring ID b gets assigned to the LUT at ring ID $b + d$ with the distance d in units of PMT rings between them. The ID k' can be transformed using equation (4.12). Thus the ring at ID k' gets assigned to the LUT values of ID k''. This does not work for ring ID l, which would exceed the maximum ring ID. Therefore another ring ID below with the same distance to the LUT ID $b + d$ is chosen.

$$k''' = b_{LUT} - (k'' - b_{LUT}), \tag{4.13}$$

with $b_{LUT} = b + d$ representing the ring ID of the LUT and $k'' = l + d$ in the example of figure 4.7.

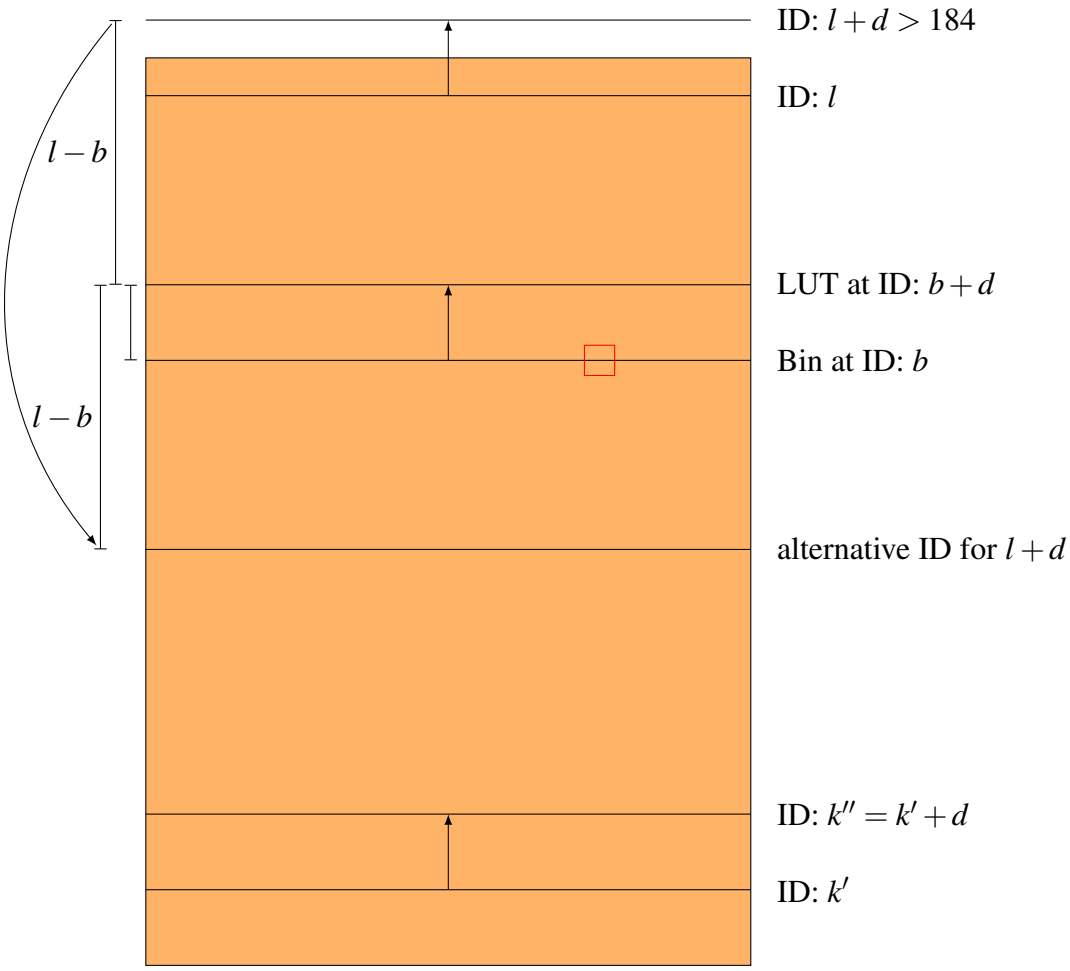

Figure 4.7: Visualisation of the ring ID transformations in the upper detector half. The bin at ring ID b gets assigned to the LUT at ring ID $b+d$ with the distance d to each other. The transformation for ring ID k follows equation 4.12. For the transformation of the ring ID an alternative ring ID needs to be found, since ring ID $l+d$ does not exist.

Another problem is the phase-shift of two adjacent PMT rings of $\Delta\Phi = 1.25°$. Therefore the final z-distribution of LUTs consists out of 10 triple-packs. The 10 triple-packs are evenly distributed over the upper detector half. Each triple-pack is simulated on two PMT rings, one being odd and one being even. Two on the height of both PMT rings and one in the middle of both PMT rings.

Thus another rule has to determine if the bin is located on an even or odd PMT ring ore in the middle of two adjacent PMT rings. This finally determines the scattered light LUT and the transformation of the PMT distribution for each bin in the detector target volume.

An exemplary scattered light LUT for $z = 0.0\,\text{cm}$, $r = 0.0\,\text{cm}$ and the angle zero with

$n_{ph} = 10000000$ simulated photons can be seen in figure 4.8. The two dimensional histogram consists out of the scattered light probability. The PMT ID is found on the x-axis and the time t in ns on the y-axis. The palette ranges from 0 to 100 because the scattered light probability times $n_{ph}s$ is stored. The transition on PMT ID 26640 is caused by the transition from the PMTs on the cylinder barrel to the PMTs of the detectors caps.

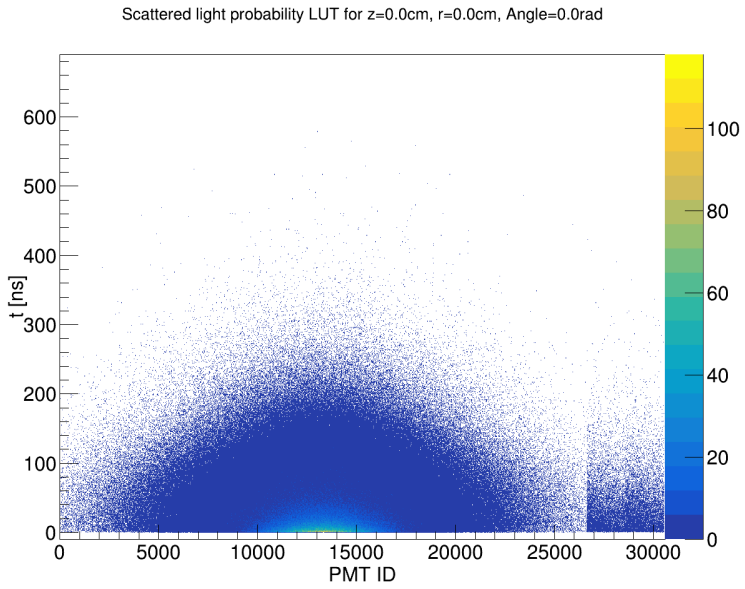

Figure 4.8: Scattered light LUT for $z = 0.0\,\text{cm}$, $r = 0.0\,\text{cm}$ and the angle zero. The PMT IDs are shown on the x-axis with the time of flight corrected hit time on the y-axis. The pallete shows the scattered light probability times the number of simulated photons ($n_{ph} = 10000000$). The transition on PMT ID 26640 is caused by the transition from the PMTs on the cylinder barrel to the PMTs of the detectors caps.

A transformation rule for the cap PMTs is yet to be made. All reconstructions done with the SLA do not use the cap PMTs.

4.4.2 Direct light LUTs

The direct light LUT without a time dependency was already implemented in the reconstruction algorithm. Thus the direct light probability for a spatial point in the detector volume for a particular PMT is available. The LUT was reused and the time dependency was implemented following two approaches. The first approach was a cut on the time of flight corrected hit time t_{tof}.

This is the actual hit time t_h on the PMT at position $\mathbf{r}_j$ minus the propagation time of a particle to a spatial point $\mathbf{x}$ with speed of light and the propagation time of the photon from the spatial point to the PMT with the speed of light in the scintillator medium.

$$t_{tof} = t_h - \frac{\mathbf{x}-\mathbf{r}}{c_0} - \frac{\mathbf{r}_j-\mathbf{x}}{c/n} \tag{4.14}$$

$\mathbf{r}$ denotes the reference point (here: vertex of the particle) and n denotes the refraction index of the scintillator.

If the time of flight corrected hit time exceeded 0.5 ns, the direct light probability of the hit seen from a spatial point was set to zero. The correction of the time of flight was also done in the scattered light LUTs. The bin structure of the reconstruction and the structure of the emission points in the LUTs are distinct. Hence, the time of flight to the PMT from the bin center and emission point are not the same. To account for these small differences, the value for the bin is looked up in the nearest LUT at the time of flight corrected hit time computed from the bin center. This yields the best result given the uncertainties of the LUT structure. The second approach was to weigh the direct light probability from a spatial point with the normalized time distribution of the scintillator decay components and electronics. The histogram follows the function of figure 3.8 and can be seen in figure 4.9. Consequently the hits get a better rating for their direct light probability.

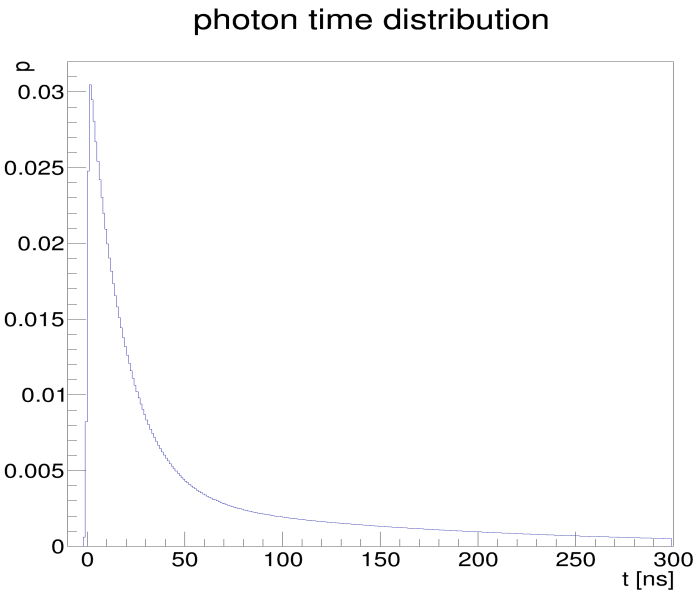

Figure 4.9: Histogram of the photon time distribution in figure 3.8.

Furthermore, the cut of 0.5 ns is not reasonable for large bins, because the direct light probability gets highly influenced by binning effects. The light travels roughly 20 cm in 1 ns. If the bin size is set to $100 \times 100 \times 100\,\mathrm{cm}^3$ the binning itself discards a lot of direct light probabilities possibly true for the event. Although, this problem is not essentially fixed by the time distribution, it improves the algorithm. In addition randomized bin centres were computed based on appendix 6.2.2 to decrease binning effects, which occur when a fixed structure gets used for an actually continuous effect.

4.4.3 The algorithm

The intuitive way of implementing the SLA would be a loop over all hits and a direct determination of the probabilities for scattered and direct light. Unfortunately the LUTs are bound to the bins of the reconstruction grid, thus the time to load every LUT for each hit and convert every bin for each hit would be time consuming. The solution is an assignment of every bin to its corresponding LUT. Therefore the algorithm loops over all LUTs utilized and then processes every bin assigned to it. Thus the total direct light probability of equation (4.7) does not get computed at a stride. In fact the sums of direct and scattered light probability are calculated and at the end of the loop assigned to each hit following equation (4.7).

The current state of the SLA increases the already inadequate computation time of the reconstruction algorithm. One approach would be to detach the assignment of the bin to the LUT and form LUTs for all detector bins. This would greatly enlarge the memory usage, but could yield easier forms of an implementation, with less computation time due to less steps of calculation. Furthermore, the algorithm is parallelisable. The best approach would be an analytical ansatz as implemented for the direct light algorithm. This is yet to be achieved and a highly non trivial task.

4.5 Improvement of the probability mask

The Wonsak reconstruction algorithm is time consuming. To veto muon events only a rough topology with its spatial energy distribution is needed. It has already been stated that the algorithm encounters problems with scattered light in multi GeV muon event ranges. One simple solution is to get a probability mask with fast reconstruction algorithms (See section 3.5), perform the scattered light algorithm and start the reconstruction algorithm afterwards. This process saves the iterations of the reconstruction algorithm to find the topology of the event and produces an acceptable result for muon vetos.

The probability mask is a scalar field representing the events topology within the detector geometry. It does not stand for the spatial number density of emitted photons. The utilization is to provide a topology for the reconstruction algorithm. Therefore, the probability mask reduces the to be reconstructed volume. Only if the number density of emitted photons is calculated for the topology of the event, an estimation of the spatial deposited energy can be made. Thus the reconstruction algorithm is an iterative process.

Two approaches were acquired. One uses the information of the track of the primary particle of the event. The other further derives a rough energy distribution over the z-axis of the detector from the photon hit distribution over the z-axis to weight the result of the first approach.

The input from other reconstruction algorithms is a plain knowledge of the particles track. For multi-GeV muons the probability of traversing the detector completely is realistic (See equation 4.3). The probability mask is therefore assumed to be a cylinder around the track. Using appendix 6.2.1 to calculate the distance between a point $\mathbf{x}$ and a line in three dimensions the probability mask can be derived from a scalar function $f(d_t(\mathbf{x}))$ of the distance $d_t(\mathbf{x})$ to the particles track. The shape of the function $f(d_t(\mathbf{x}))$ should respect the vertical extent of the track of the muon. For this instance the function was set to 1 for the interval $[0,350]\,\mathrm{cm}$ of the vertical distance to the track. An exponential decay over the interval $(350,450]\,\mathrm{cm}$, as well as the value 0 for distances exceeding 450 cm was further applied to the function $f(d_t(\mathbf{x}))$. Thus $f(d_t(\mathbf{x}))$ follows equation 4.15 and satisfies the ^{9}Li distribution of figure 2.7b around the track.

$$f(d_t(\mathbf{x})) = \begin{cases} 1 \text{ for } d_t \in [0,350]\,\mathrm{cm} \\ \exp(-\frac{d_t - 350\,\mathrm{cm}}{10000\,\mathrm{cm}}) \text{ for } d_t \in (350,450] \\ 0 \text{ else} \end{cases} \tag{4.15}$$

This probability mask minimizes the volume for the reconstruction algorithm without neglecting possible origins of background events to a significance level beyond 99% [24] (See figure 2.7b).

Although the exponential decay function is a better fit to the actual event, binary probability masks following the function $f_{bin}(d_t(\mathbf{x}))$ of equation (4.16) where created, because of the negative binning effect of high edge length bins with a decay function exponentially decaying from one to zero over an interval with absolute length lower than the bins edge length.

$$f_{bin}(d_t(\mathbf{x})) = \begin{cases} 1 \text{ for } d_t \in [0,450]\,\text{cm} \\ 0 \text{ else} \end{cases} \tag{4.16}$$

Both functions are plotted over the interval $[0,600]\,\text{cm}$ in figure 4.10a and 4.10b.

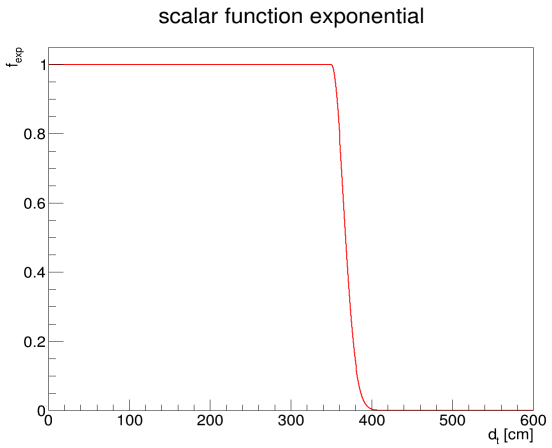

(a) Plot of the scalar function of equation 4.15.

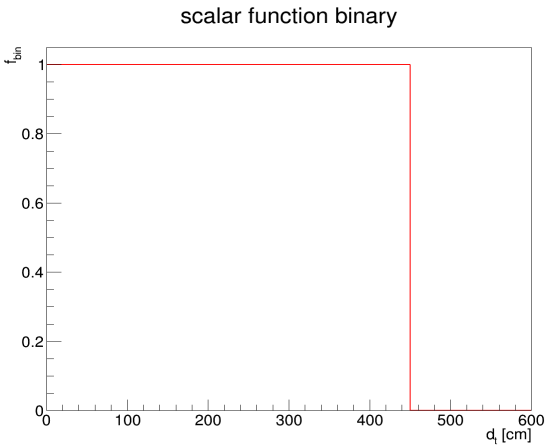

(b) Plot of the scalar function of equation 4.16.

Figure 4.10: Scalar functions used to determine the value of the probability mask perpendicular to the main particles track.

A further possibility to enhance the probability mask is to weight the detector's z-axis of the event. Especially for LENA the photon hit distribution over the PMT-rings describes the rough energy distribution of mostly vertical events. This was found with a qualitative examination of 10 events with muons of 40 GeV surpassing the detector mostly vertically. This can be seen in figure 4.11 with the photon hit distribution over the z-axis (figure 4.11a) and the MC-data of deposited energy in form of secondary particles over the z-axis (figure 4.11b).

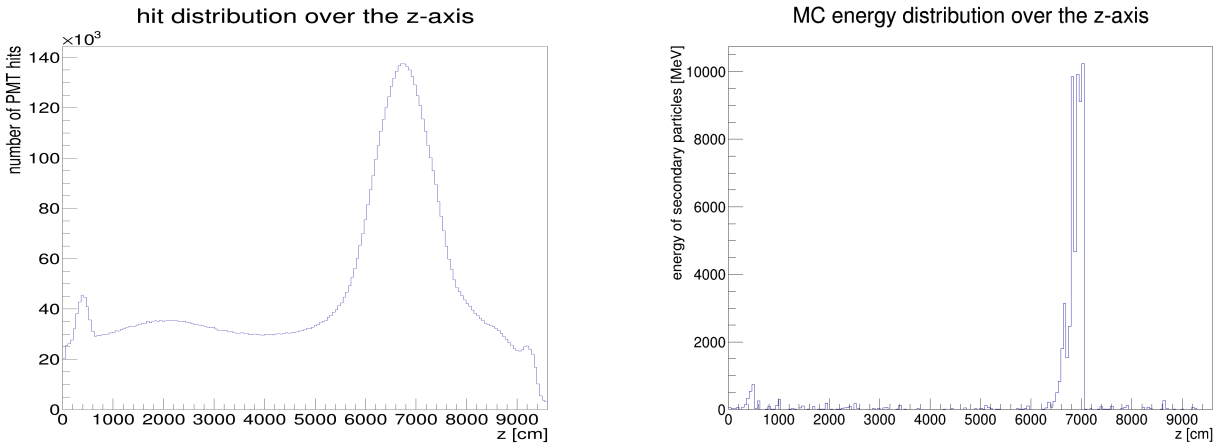

(a) Distribution of the photon hits over the PMTs. Each PMT ID is dereferenced to its position on the detectors z-axis starting from zero at the bottom.

(b) Distribution of the kinetic energy of the secondary particles based on the MC-Truth data. The kinetic energy at the vertex of the secondary particle is projected on the z-axis.

Figure 4.11: Comparison between the distribution of photon hits and the energy of secondary particles based on the MC data over the z-axis. The distribution of photon hits over the z-axis is highly correlated to the deposited energy.

If a particle traverses the LENA detector all rings of PMTs get approximately the same amount of light regardless of the position of the particle in the particular ring. Thus the amount of detected photons in one PMT ring is approximately independent of the point of emission in the PMT ring. A basic simulation of this effect is shown in figure 4.12. The average direct light probability in one PMT ring was calculated for over a million emission points. The average direct light probability from one emission point is the normalized sum of the direct light probabilities of 144 PMT simulated around the ring.

The two dimensional histogram holds the average direct light probability calculated by equation 3.3 over all PMTs in one ring for a point (x,y). The average direct light probability differs slightly in the inner volume with a total deviation of 8% from the innermost to the outermost edge. Thus the approximation that all PMT rings get the same amount of light regardless of the origin of the light within the PMT ring is acceptable.

This does not apply to the PMT rings near the caps of the LENA detector. These PMT rings get less light since the target volume nearby with a non vanishing direct light probability is lesser than a PMT ring in the middle. This effect was disregarded for this probability mask.

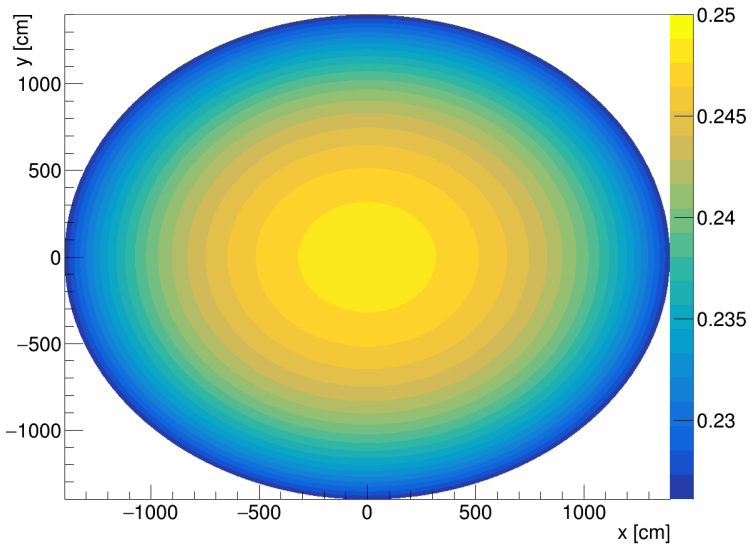

Figure 4.12: Simulation of the average direct light probability in one xy-projected ring in the LENA detector. The PMTs are evenly distributed over the outer circle (transition from blue to yellow). The value for each bin is the average direct light probability of all PMTs from the bin center.

The photon hit distribution is naturally binned by the distance between two PMT rings. This histogram can be fit and provides another scalar function $g(z(\mathbf{x}))$ of the z-coordinate of the point $\mathbf{x}$. Thus the total scalar field $\Phi(\mathbf{x})$ for the probability mask is given by

$$\Phi(\mathbf{x}) = f(d_t(\mathbf{x})) \cdot g(z(\mathbf{x})) \tag{4.17}$$

The implementation of a z-modulation in JUNO is more complex due to its spheric symmetry. Furthermore the modulation would rather be a modulation along the particle's track. Therefore the detector is divided into circles of PMTs perpendicular to the track. To maintain equality the changing distance and quantity of the PMTs in each ring has to be taken into account. Furthermore the angular acceptance changes for each perpendicular ring.

The probability mask with a z-modulation can be seen in figure 4.13b. The weighting for the z-axis is shown in figure 4.11a. For comparability the probability mask without this z-modulation is shown in figure 4.13a.

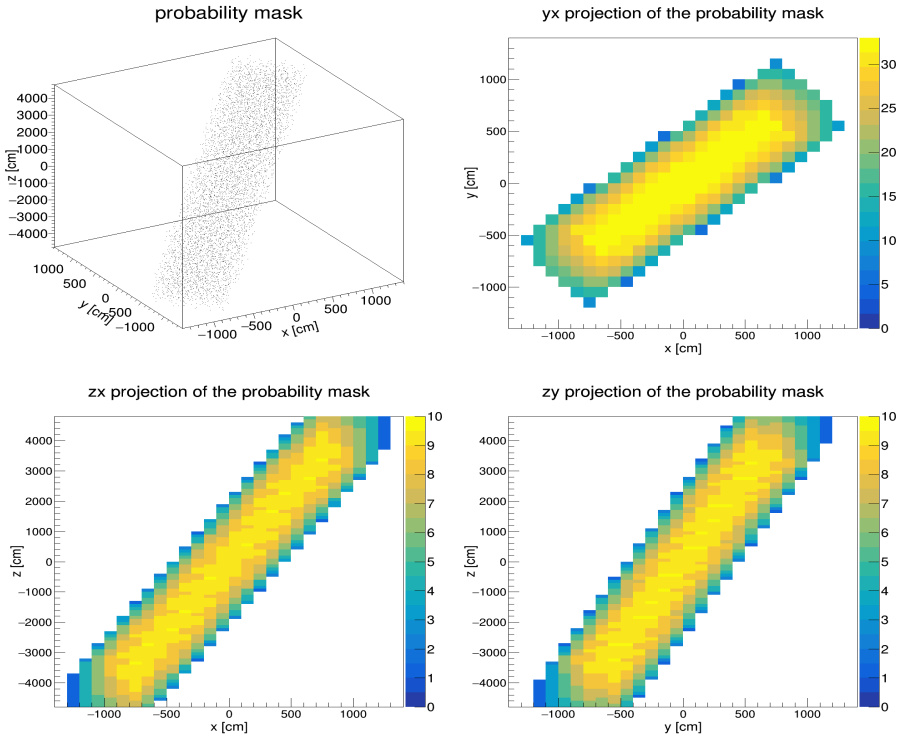

(a) Probability mask using the z-modulation of figure 4.11a.

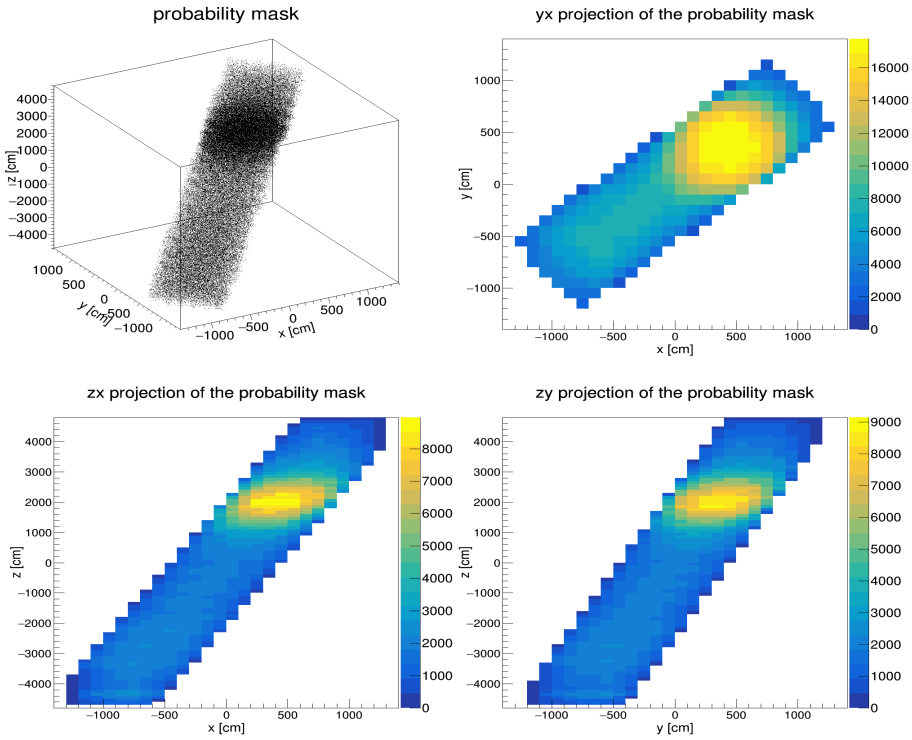

(b) Plain probability mask around the track of the muon.

Figure 4.13: Probability masks created around the track of a 40 GeV muon surpassing the detector with the input values suggested in section 4.1. The binary probability mask function of equation 4.16 was applied. Both probability masks are not normalized.

4.6 Removing critical PMTs

Another approach tested in this bachelor thesis is the deliberate removing of PMTs which may hold corrupt information. Section 4.2 already covered the critical behaviour of PMTs near the track regarding scattered light, which is explicitly shown in figure 4.4. Furthermore, the SLA is problematic in these areas because of the binning effects. On the one hand the binning could be set to a small edge length of about 10 cm to enhance the SLA, but on the other hand this would cause a massive increase of computation time. Therefore this is only an option if the reconstruction algorithm is foreseen to do a full run onto the event. A more applied approach would be the removal of the PMTs near the track of the muon. Thus the SLA has not to be performed or can be done with a wider binning, because the PMTs where it is sentenced to fail are disregarded. In addition the simulation is able to process huge amounts of incident photons at a time, while a real PMT would go in saturation and lose its information. Therefore these PMTs would be removed from any reconstruction approach anyway.

The implementation in the reconstruction can be done by two approaches. The first one is to calculate if a particular PMT is near the track of the muon within a threshold distance r_t, which was set to 300 cm based on empirical knowledge. The other approach would be the removal of PMTs with a number of incident photons above a threshold number $n_{p,t}$[3]. For this work, the first approach was applied.

4.7 Improved reconstruction results

Section 4.2 already pointed out the problems the reconstruction algorithm encounters during the reconstruction of multi-GeV muon events especially in the near field of the PMTs.

Recapitulating, the SLA with a randomized binning was implemented to solve these problems. The probability masks were a necessity to run the SLA. To ensure the success of the reconstruction in the near field, PMTs near the muon's entry and exit point had the possibility to be disregarded.

These three options were tested and qualitatively evaluated in this section with a 20 GeV muon surpassing the LENA detector in the xy-plane located in the center of the detector. The entry point of the particle is $\mathbf{x}_{en} = (1400, 0, 0)$ cm and the exit point is $\mathbf{x}_{ex} = (-1400, 0, 0)$. 20 GeV is more than enough to surpass the diameter of 28 m of the detector. The xy-plane was chosen to validate the SLA with PMTs in the near field, as the cap PMTs had no transformation rules for the LUTs of the SLA. The particles created according to the MC-data are printed on

[3] In an actual experiment one would determine the PMTs which went into saturation

top of the projections of the reconstruction algorithm. It is used as an reference for the events energy deposition. It does not stand for the exact number of created photons but can be utilized as a good approximation for the number of created photons.

This analysis is exemplary to underline the problems occurring in the near field. For the far field a good result of the spatial number density of emitted photons was found for 10 40 GeV muons surpassing the detector with the values calculated in section 4.1. The near field was not tested for these events because the cap PMTs had no transformation rules (see section 4.4.1).

The main goal is to create the best possible first iteration with bins of 100 cm edge length of the reconstruction algorithm, as only a rough spatial number density of emitted photons is needed to identify a showering muon. The reconstruction algorithm has been proven to work with multi-GeV muons. Still some iterations are necessary to create a topology for the event. Therefore, this approach saves a lot of computation time of the reconstruction algorithm. The result of the iterating process is stated with the ninth iteration. These iterations are typically needed to find a topology. The ninth iteration contains bins of 50 cm edge length and got refined. Refining means the target volume further computed in the reconstruction algorithm got reduced to the events topology. The reason these plots are evaluated quantitatively is the early stage of this approach with the reconstruction algorithm. It has been proven that the eye of the observer is a valuable tool to evaluate the result of the reconstruction algorithm. Nonetheless a quantitative test of theses methods is pending.

4.7.1 Result of the reconstruction

The first look belongs to the reconstruction algorithm without the enhanced options summarized before, which can be seen in figure 4.14. Although the track of the muon is estimated well for the first reconstruction, the entry and exit point get an overestimation of spatial number density of emitted photons, which does not correspond to the MC-data which is drawn with the black lines corresponding to the secondary particles created and the red line corresponding to the primary muon. Although the spatial number density of emitted photons is somewhat larger near the shower located at $\mathbf{x} = (650, 0, 0)$ cm, the reconstruction algorithm will need further iteration steps, due to the falseness of the probability mask, which gets created by normalizing this iteration step. The ninth iteration can be seen in appendix 6.3 figure 6.1. This is the proof that the reconstruction algorithm recovers from the bad effects in the first iteration due to the iterating process.

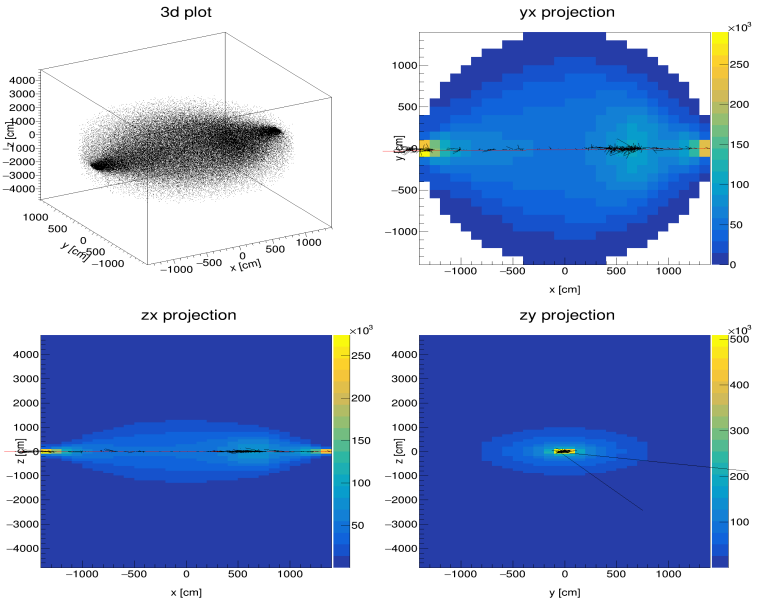

Figure 4.14: Normal reconstruction of a 20 GeV muon surpassing the center of the detector in the xy-plane.

4.7.2 Result of the reconstruction with a probability mask around the track

The reconstruction algorithm just using the probability mask created from the track information (see section 4.5), which is the MC data of the muon in this first tests, can be seen in figure 4.15. The result is better than the former approach. The particle shower at $\mathbf{x} = (600, 0, 0)$ gets assigned spatial number density of emitted photons. An overestimation on the entry and exit point of the muon is still existent, thus a failure in the near field is still imminent. The improvements originate from the squeezing of the full information into a smaller corridor. The succeeding ninth iteration can be seen appendix 6.3 figure 6.2. No major differences can be seen between the normal reconstruction with and without the probability mask around the track of the primary particle. This qualitatively proves that sharp probability masks have no bad effects on muons not stopping in the detector. For stopping muons sharp probability masks have been found to have bad edge effects for the reconstruction algorithm [46].

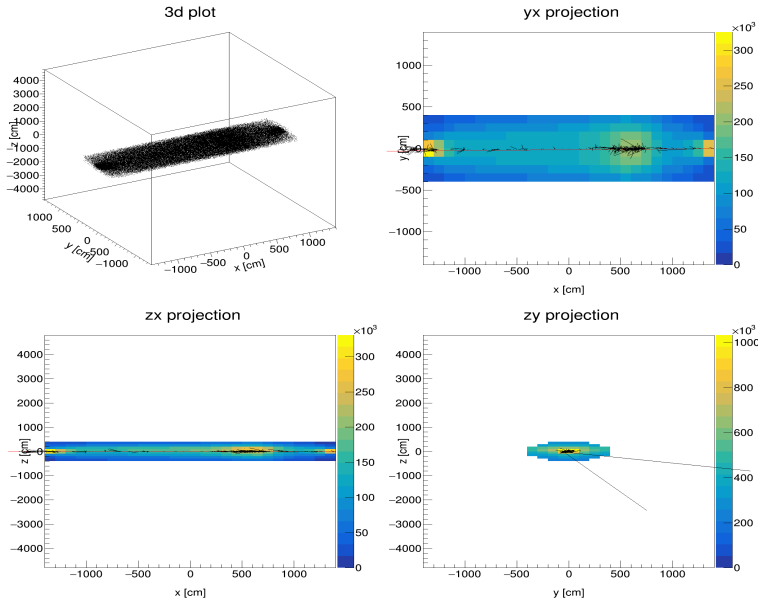

Figure 4.15: Normal reconstruction with a pre-defined probability mask of a 20 GeV muon surpassing the center of the detector in the xy-plane.

4.7.3 Result of the reconstruction algorithm utilizing the SLA

If the SLA is added the result of the reconstruction can be seen in figure 4.16. On the entry point of the muon the SLA actually works, reducing the spatial number density of emitted photons. On the exit point the SLA fails, as an additional energy deposition is done which can be seen in the MC-data printed. The SLA therefore ignores more light from the shower, located at $\mathbf{x} = (650, 0, 0)\,\text{cm}$, as it should and still overestimates the exit point. One explanation is the binning. The problematic zone on the exit point contains just a few bins of an edge length of $l = 100\,\text{cm}$. With the speed of light in the liquid scintillator of approximately $20\frac{\text{cm}}{\text{ns}}$, deviations of bin centres due to random binning and the rough binning itself do not accurately represent the near field, as they cause uncertainties of a few nanoseconds. Another strategy has to be found, which reduces the volume of the bins in these areas. The ninth iteration can be seen in appendix 6.3 figure 6.3. The result is still consistent with the MC-data but is essentially more focussed on areas with a higher energy deposition. Other areas nearly vanish in spatial number density of emitted photons.

Therefore, it is necessary to remove the PMTs near the entry and exit point of the muon to ensure a succeeding first iteration of the reconstruction. The in detail tested approaches were the reconstruction with just the probability masks and the PMTs near the track removed and the same approach with the SLA added on top. The radius around the track was set to 300 cm for the rule to turn off PMTs. Both can be seen in figure 4.17 and figure 4.18 respectively.

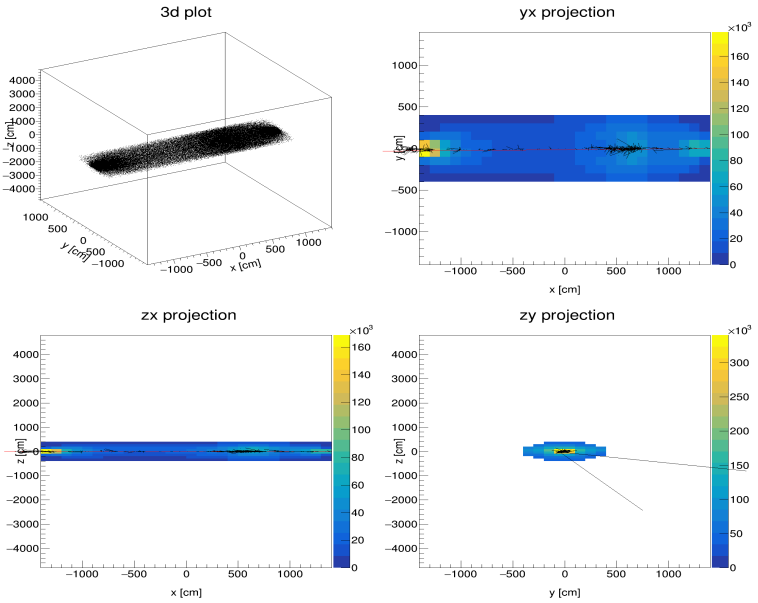

Figure 4.16: Reconstruction with a pre-defined probability mask and the SLA of a 20 GeV muon surpassing the center of the detector in the xy-plane.

4.7.4 Result of the enhanced reconstruction algorithm without the SLA

The reconstruction algorithm with the probability mask and the PMTs near the track turned off seems to succeed in the first iteration, which can bee seen in figure 4.17a. Therefore, 8 further iterations were made, reducing the binning to $50 \times 50 \times 50\,\mathrm{cm}^3$. Unfortunately the overestimation of the entry and exit point still occurs in the ninth iteration, which can be seen in figure 4.17b. Thus the near field does not profit enough if the PMTs near the track are ignored in a 300 cm radius. Increasing the radius for this rule would yield a better result for the far field, but would effectively ignore the near field. Further studies regarding the effects on the reconstruction result with an asymmetrical PMT distribution are necessary.

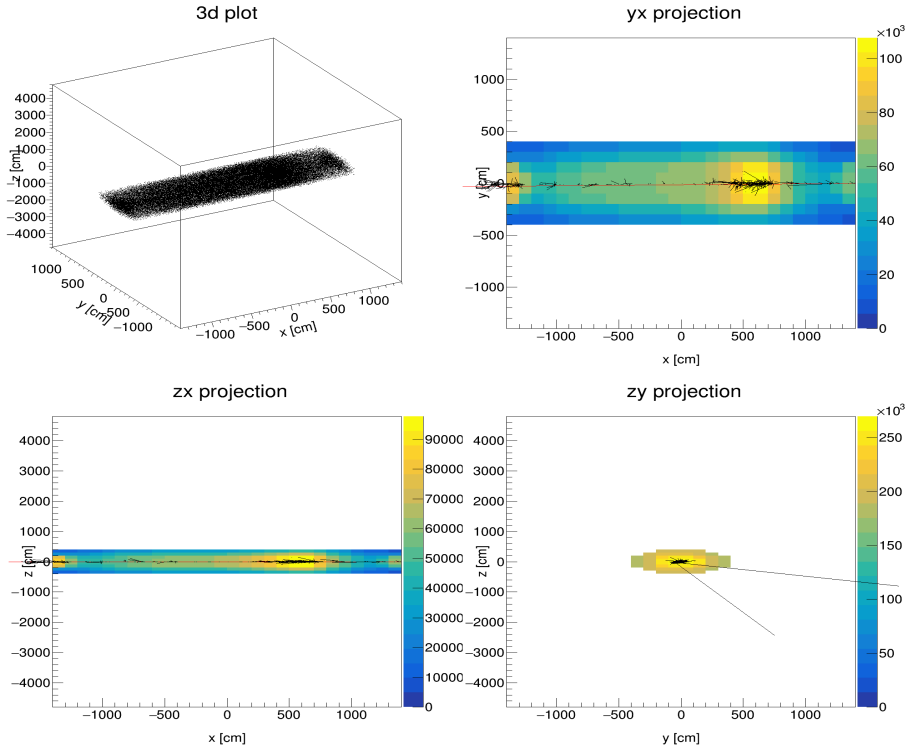

(a) First iteration.

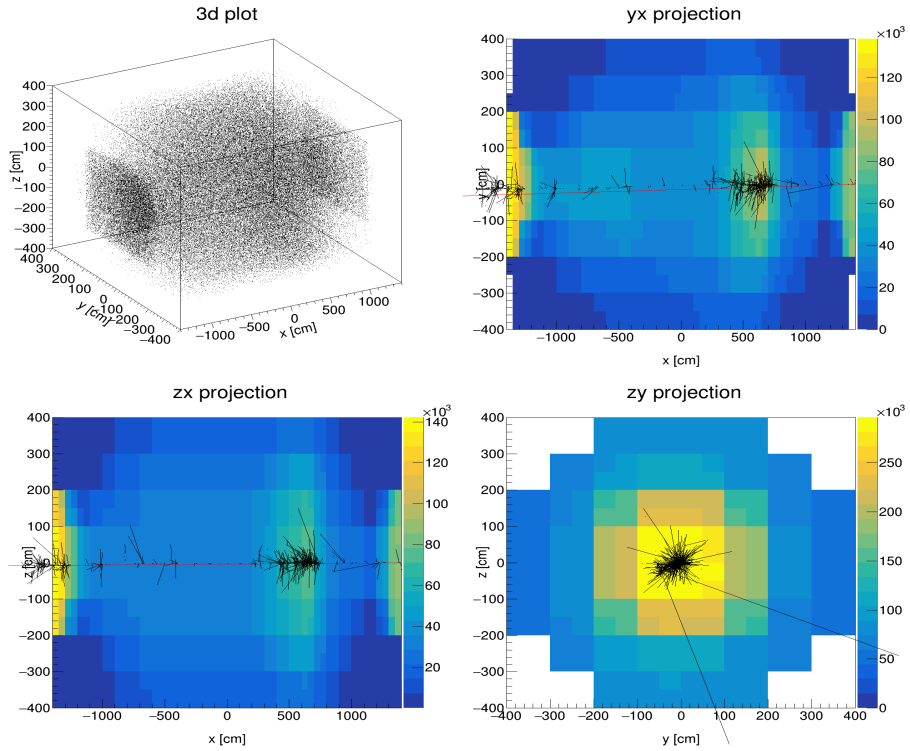

(b) Ninth iteration.

Figure 4.17: Normal reconstruction with a pre-defined probability mask of a 20 GeV muon surpassing the center of the detector in the xy-plane. In addition the PMTs near the track of the muon are turned off for the reconstruction.

4.7.5 Result of the enhanced reconstruction algorithm

The enhanced reconstruction algorithm contains the normal reconstruction algorithm with a probability mask around the track and the SLA. Furthermore, the PMTs within 300 cm of the track of the muon are turned off.

Looking at the enhanced reconstruction algorithm, the first iteration in figure 4.18a is looking worse to the former approach. The shower is found, but the spatial number density of emitted photons in the near field seems to vanish. This may be true in relation to the shower, but is still false in relation to the rest of the track. The ninth iteration in figure 4.18b yields a better result and is mostly consistent with the MC-Data. The shower is estimated properly , but the near field has a nearly vanishing spatial number density of emitted photons. Thus the scattered light algorithm ignores light from the near field on a rough binning, instead of correcting it properly.

In conclusion the fully enhance reconstruction algorithm yields the best result, although the near field was not reconstructed properly. For the study of the identification of showers of muons the events surpassed mostly the far field. Thus a failure of the enhanced reconstruction algorithm is not to be expected.

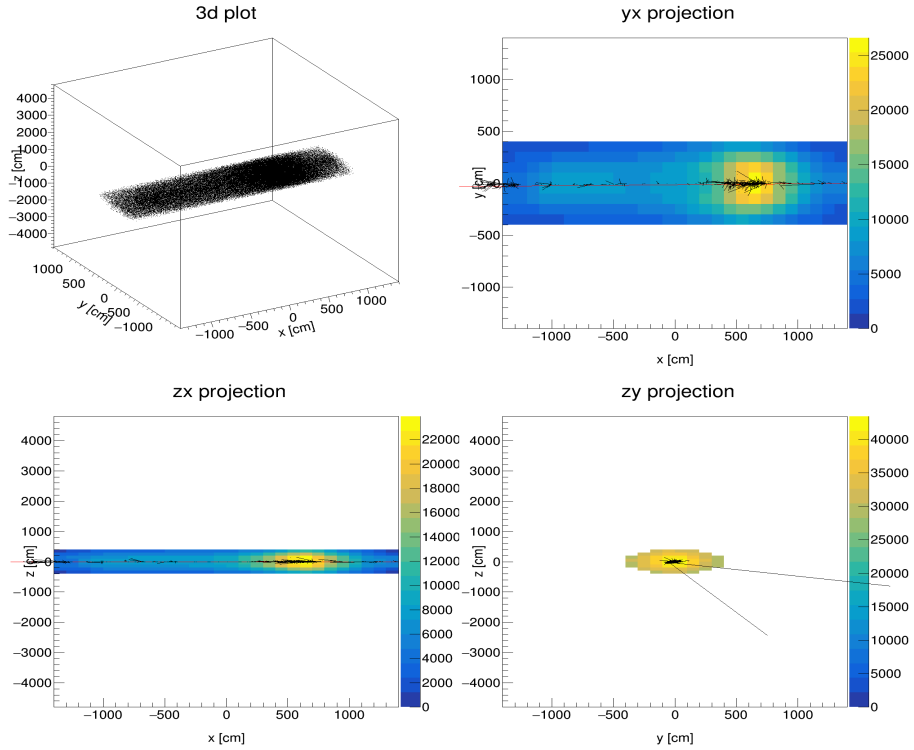

(a) First iteration.

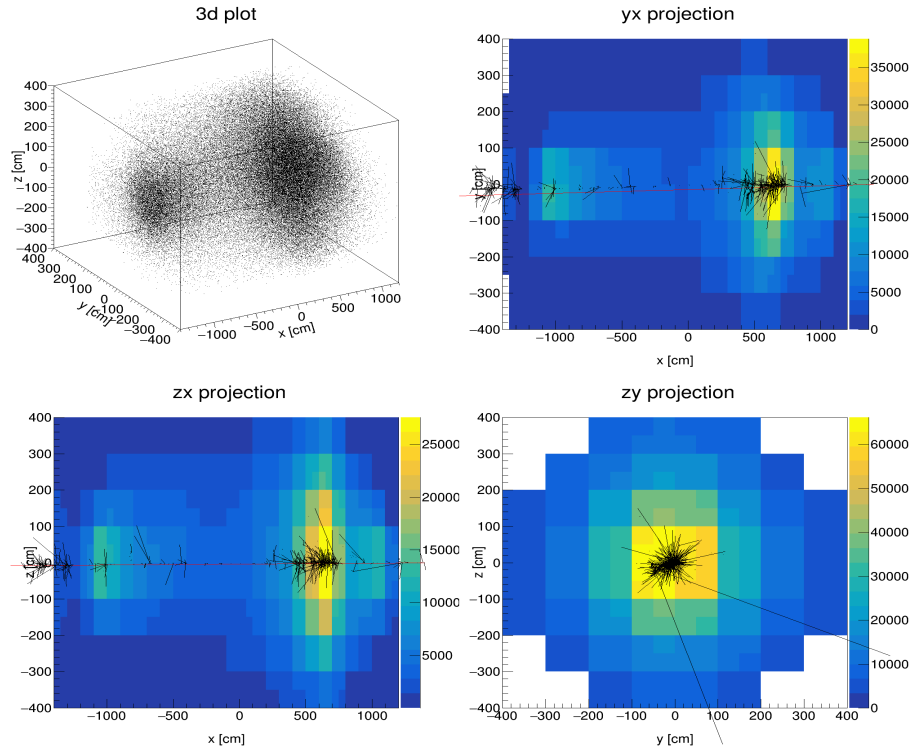

(b) Ninth iteration.

Figure 4.18: Reconstruction with a pre-defined probability mask and the SLA of a 20 GeV muon surpassing the center of the detector in the xy-plane. In addition the PMTs near the track of the muon are turned off for the reconstruction.

4.8 Identification of showering muons

The resulting spatial number density of emitted photons holds information of the spatial energy deposition of the charged particles. Thus, the reconstruction algorithm is able to identify the position of high energy deposition which could be induced by a showering muon. Utilizing the improved reconstruction algorithm makes the topological muon event reconstruction for multi-GeV muon energies accessible.

One possible way to examine the energy deposition for multi-GeV muons is the projection of the result of the reconstruction algorithm on the track of the muon. This allows a determination of epicentres of high energy deposition. The track of the muon can be determined using the pre-reconstruction information of the track of the muon (See section 4.5). If the reconstruction is build on the raw reconstruction algorithm (see section 3.4.1) the track of the muon can be determined by various algorithms [25]. Since the reconstruction utilized a probability mask with the track information of the primary particle, this information was used. Therefore, the track used for these projections is the track of the MC-Truth data.

The content of the bins in the reconstruction algorithm was projected perpendicular to the track of the muon using the calculation in appendix 6.2.1. Furthermore, the MC-Data is used as a reference. Unfortunately the MC-Data does not cover the full spatial number density of emitted photons of the event. But the MC data covers all secondary particles created storing the value of their initial energies. This can be utilized as an approximation to the number of created photons, but does not yield the exact number, as the light production in the scintillator is not the same for different particles. Therefore the energies of the secondary particles were projected on the track of the primary muon. Because most secondary particles do not travel far from their origin, the point between their start and end point was projected. This clearly marks the epicentres of high energy depositions. Thus this suffices the requirement of a reference for the identification of muon showers.

Although no quantitative evaluation was done, a good qualitative result could be reproduced for 10 events of 40 GeV muons. Therefore, two remarkable events are chosen as examples. The first event can be seen in figure 4.19 with the relative energy calculated by the enhanced reconstruction algorithm in figure 4.19a and the energy distribution based on the energies of the secondary particles of the MC-Data in figure 4.19b. The x-axis represents the track of the primary particle starting on the vertex at $x = 0\,\text{cm}$ in these figures.

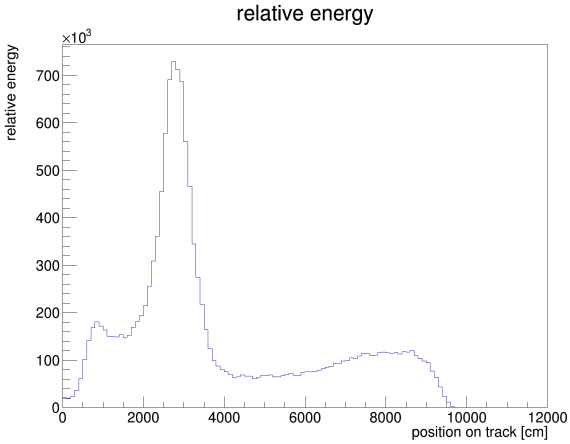

(a) Relative energy distribution over the track of the primary particle computed with the enhanced reconstruction algorithm.

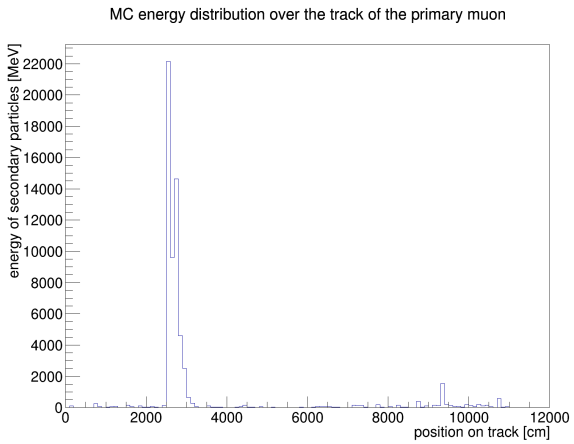

(b) Distribution of the energy of the secondary particles based on the MC-Truth data over the track of the primary particle.

Figure 4.19: Comparison of the energy distributions calculated with the enhanced reconstruction algorithm and the MC-Data. Both graphs start at the vertex of the primary particle. The primary particle is a muon with an initial kinetic energy of 40 GeV. The plot of the reconstruction can be viewed in appendix 6.4 figure 6.4

The enhanced reconstruction algorithm is able to locate the muon shower at the position $x = 2750\,\text{cm}$ on the track. This is consistent with the huge amount of particles produced stated by the MC-Data. It is necessary to note that the MC-Data does not reveal the true energy, which gets deposited. It does not take the actual scintillation effect into account. Therefore, basic differential energy loss can be seen in the reconstructed energy distribution. The edge effects of the reconstructed energy distribution decreasing approaching $x = 0\,\text{cm}$ and $x = 9750\,\text{cm}$ is due to the detectors geometry. In these areas there is not as much target volume nearby. Thus, the projection onto the track does not represent the relative energy loss in these areas. Since the focus lies on the identification of high energy depositions these effects are ignored and not corrected with the actual target volume perpendicular to the track. Furthermore, the cap PMTs are not included in the enhanced reconstruction algorithm. Thus the information near the caps is to treat with caution. Nonetheless the algorithm and the track projections work well for the target volume more than 500 cm apart from the detector caps.

The cut to zero at $x = 9600\,\text{cm}$ in the projection of the reconstruction algorithm is due to the particle leaving the target volume. The MC-data further covers the buffer and veto, which is not relevant for this analysis.

The second event can be seen in figure 4.20. Both graphs are shown in the same way as for the former muon event.

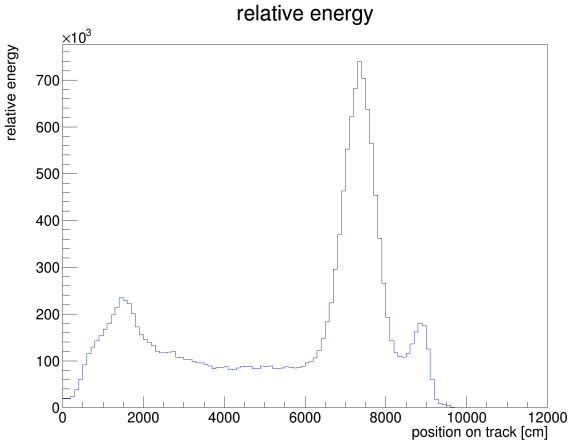

(a) Relative energy distribution over the track of the primary particle computed with the enhanced reconstruction algorithm.

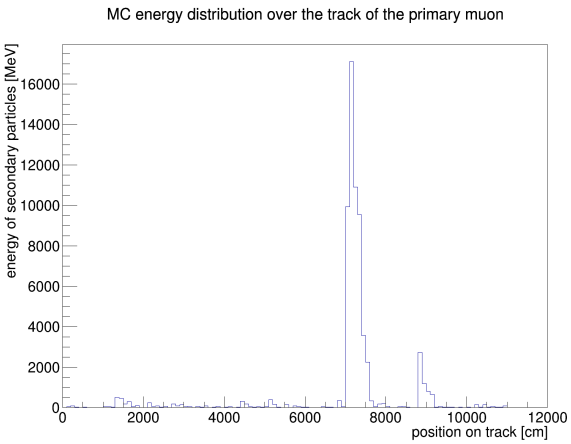

(b) Distribution of the energy of the secondary particles based on the MC-Truth data over the track of the primary particle.

Figure 4.20: Comparison of the energy distributions calculated with the enhanced reconstruction algorithm and the MC-Data. Both graphs start at the vertex of the primary particle. The primary particle is a muon with an initial kinetic energy of 40 GeV. The plot of the reconstruction can be looked up in appendix 6.4 figure 6.5

The enhanced reconstruction algorithm is able to locate the muon shower[4] at $x = 7250\,\text{cm}$ and also the second peak at $x = 9000\,\text{cm}$. Unfortunately the peak at $x = 1500\,\text{cm}$ is not fully explainable with the MC-Truth. It needs to be stated, that the secondary particles are no exact measure for the number of photons emitted. The comparability is only given for huge energy depositions like a muon shower.

For a better overview both reconstruction results are shown as projection plots with the particles of the MC-Data printed on top in figure 4.21.

The reconstruction result is a good fit to the MC-event data, although this is the first iteration of the reconstruction algorithm. If an evaluation beyond the localisation of the muon shower is needed, more iterations are needed.

The other 8 events yield the same result, if the muon produced a shower. If the energy deposition was distributed over the whole track, no clear difference could be found. Therefore, more iterations are needed.

[4] This was actually a hadronic shower

The following example in figure 4.21 depicts a problematic case for the analysis.

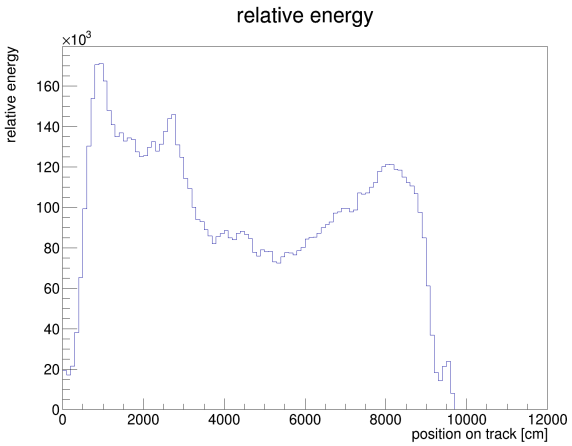

(a) Relative energy distribution over the track of the primary particle computed with the enhanced reconstruction algorithm.

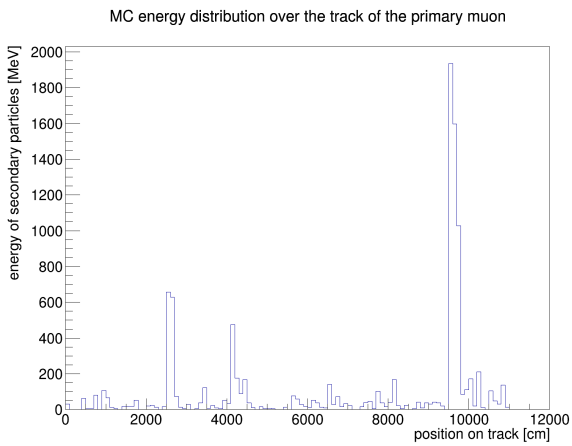

(b) Distribution of the energy of the secondary particles based on the MC-Truth data over the track of the primary particle.

Figure 4.21: Comparison of the energy distributions calculated with the enhanced reconstruction algorithm and the MC-Data. Both graphs start at the vertex of the primary particle. The primary particle is a muon with an initial kinetic energy of 40 GeV. The plot of the reconstruction can be seen in appendix 6.4 figure 6.6

The MC energy distribution in figure 4.21b shows a high energy deposition near $x = 9600\,\text{cm}$ on the track. This region is not fully covered with target volume and near the cap PMTs, which are turned off. Therefore, the enhanced reconstruction algorithm does not yield the best result for this region, which can be seen in figure 4.21a. Furthermore, the region around $x = 2600\,\text{cm}$ does get more spatial number density of emitted photons, which is explainable with the MC-data. The region around $x = 1000\,\text{cm}$ also gets a huge valuation. This does not correspond with the MC-data. The differences between the energy distributions are therefore not distinct enough. In these cases the MC-data of the secondary particles is to be read with caution. It does not cover the full data about each photon created. With these relatively small deviations in the energy distribution a concrete evaluation can not be made.

5 Conclusion

Within this bachelor thesis showering muons were analysed with the novel algorithm for topological reconstruction in liquid scintillator detectors developed in Hamburg. Therefore, multi-GeV muon events were simulated with the LENA simulation and reconstructed with the novel reconstruction algorithm, which got enhanced for high energy events by developing suitable probability masks and an algorithm to correct false information yield by scattered light. The goal was to spatially resolve muon showers in the detector to prove that an effective vetoing of the muon background in liquid scintillator detector events is possible with the novel reconstruction algorithm.

The first result is an improved reconstruction algorithm for multi-GeV muon events. This shows in particular, that sharp probability masks can be applied to muons fully traversing the detector (see section 4.5). This allows an early application of an algorithm to correct scattered light (see section 4.3). Furthermore, these probability masks reduce the long run time of the reconstruction algorithm by the iterations, which are necessary to find the topology of the event. In addition, the scattered light algorithm induces positive effects on the reconstruction result, although it does not correct the problematic near field of PMTs. For this instance the deliberate ignoring of PMTs near the muons entry and exit point in the reconstruction algorithm has been proven to be robust. The lost information affects solely the near field of those PMTs. Combined, those improvements promise good results for the reconstruction of high energy muons (See section 4.7).

The second result is the possibility to spatially resolve particle showers of muons with the enhanced reconstruction algorithm. In a first qualitative analysis only small deviations of the epicentre of a particle shower from the reconstructed data to the MC data was found in 10 muon events of 40 GeV initial kinetic energy (see section 4.8). Furthermore, the analysis was performed with the first iteration of the enhanced reconstruction algorithm, not fully taking advantage of the capabilities of the reconstruction algorithm. In addition the computation time of ~ 40 min on a Intel Xeon 2.67 GHz CPU for the first iteration of a muon with 40 GeV initial kinetic energy is reasonable. There is a possibility of further optimizations and a parallelisation, as well as much better hardware.

Thus, the reconstruction algorithm can be applied to calculate a suitable veto for the muon background in large liquid scintillator detectors.

The relevance of this reconstruction strategy for the upcoming JUNO experiment depends on further improvements. At first the scattered light algorithm demands JUNO specific look-up-tables for scattered light. Furthermore, the strategy regarding the binning for the scattered light algorithm needs improvements for the near-field. In addition the run time of the reconstruction algorithm is intolerable. Therefore, the conditioning of the reconstruction algorithm for a parallelisation is inevitable.

6 Appendix

6.1 Macros for the LENA Simulation

The following subsections contain the macros for the LENA simulation. The given values are for the events discussed in chapter 4. For a detailed documentation of the command lines see [35].

6.1.1 Physics.mac

```
#nuclear processes
/Lena/phys/reg G4EmExtra
#elastic hadron processes not covering neutrons
/Lena/phys/reg G4HadronElastic
#inelastic hadron processes including elastic processes for
   ↪ neutrons
/Lena/phys/reg HadronQGSP_BERT_HP
#capture processes
/Lena/phys/reg G4QStopping
#physics processes for ions
/Lena/phys/reg G4Ion
#optical photon physics(e.g. scintillation/scattering
   ↪ process)
/Lena/phys/reg LenaOP
#radioactive decays
/Lena/phys/reg G4Radioactive
#muonnuclear processes (extended package for muons in LENA)
/physics_engine/tailor/MuonNuclear on
#initialize the physics list
/run/initialize
```

```
/control/verbose 2
/run/verbose 2
#set the light yield in MeV^{-1}
/Lena/det/light_yield 2000
#don't generate dark counts/late pulses/after pulses
/Lena/det/dark_noise false
/Lena/det/late_pulses false
/Lena/det/after_pulses false
#turn off time of flight correction of simulated photon hits
/Lena/det/tof false
#simulate particles with a particle gun
/Lena/gun/type 0
#particle type (here: muon)
/gun/particle mu-
#the primary particles kinetic energy
/gun/energy 40000 MeV
#position of the gun (vertex of the primary particle)
/gun/position  1000 830 4600 cm
#direction of the primary particle
/gun/direction -0.209202833 -0.173638351 -0.96233303
```

6.1.2 Geometry.mac

```
#use PMTs indivdually (false: use the whole detector wall)
/Lena/det/pmts true
#don't use a geometrical model of the winston cones (saves
   ↪ computation time)
#but use the angle LUTs from BOREXINO (type 1)
/Lena/det/winston_cones_geo false
/Lena/det/winston_cones true
/Lena/det/winston_cones_type 1
#simulate PMTs as flat discs
/Lena/det/pmt_sphere false
#set data for PMT discs
/Lena/det/geo/setRadiusPMTEncapsulation 27 cm
```

```
/Lena/det/geo/setRadiusPMT 0.255440795489 m
/Lena/det/geo/setHeightPMTEncapsulation 0.1 cm
#set the PMT distribution
/Lena/det/geo/setNumPMTRings 185
/Lena/det/geo/setNumPMTPerRing 144
/Lena/det/geo/setNumPMTRingsCap 25
/Lena/det/geo/setPMTRingCapConst 6
#--- DETECTOR GEOMETRY ---#
#set radius and hight of the veto, tank, target and buffer
/Lena/det/geo/setRadiusVeto 18.6 m
/Lena/det/geo/setHeightVeto 50.6 m
/Lena/det/geo/setRadiusTank 16.6 m
/Lena/det/geo/setHeightTank 50.6 m
/Lena/det/geo/setRadiusTarget 14 m
/Lena/det/geo/setHeightTarget 48 m
/Lena/det/geo/setRadiusOuterBuffer 16 m
/Lena/det/geo/setHeightOuterBuffer 50 m
/Lena/det/geo/setRadiusBuffer 14.25 m
/Lena/det/geo/setHeightBuffer 48.25 m
#position the PMT at the edge of the buffer, so that are
   ↪ completely inside the buffer volume
/Lena/det/geo/setDistanceTankPMT 0.20 m
#update the geometry (fully loads the now specified detector
   ↪ )
/Lena/det/update
```

6.1.3 Template.mac

```
#save the Monte Carlo Event data
/Lena/run/saveMcData true
#RNG (Random Number Generator) seed set by the time
/Lena/run/setSeedFromTime
#do not save RNG-seeds
/Lena/run/saveMcSeed false
#normal simulation type
```

```
/Lena/run/sim_type 2
#save every photon hit, but save only minimal information
   ↪ about each hit (only hit time)
/Lena/run/sim_subtype 3
#load the physics.mac and geometry.mac
/control/execute /nfs/neutrino/data2/fbenckwitz/lenasim/
   ↪ trunk/macros/physics2.mac
/control/execute /nfs/neutrino/data2/fbenckwitz/lenasim/
   ↪ trunk/macros/geometry.mac
#set the output path
/Lena/run/setOutputPath /nfs/neutrino/data2/fbenckwitz/
   ↪ lenasim/trunk/simoutput/
#set the filename
/Lena/run/setOutputFileName
   ↪ mu__n10__40GeV__1000_830_4600_cm__-0.209_-0.174_-0.962
   ↪ _10particles
#set the number of successive events
/run/beamOn 10
```

6.2 Mathematical derivations

Some basic mathematical derivations used for this thesis are collected in this section of the appendix.

6.2.1 Calculating the distance point-line in three dimensions

For this derivation the shortest distance of a point $\mathbf{x}_\mathrm{p}$ to a line $[\mathbf{x} \in \mathbb{R}^3 | \mathbf{x} = \mathbf{x}_0 + a \cdot \mathbf{v}]$ is calculated. $\mathbf{x}_0$ is the line's reference point and $\mathbf{v}$ is the direction vector and $a \in \mathbb{R}^1$.

At first the start vector $\mathbf{v}_\mathrm{s}$ is calculated as the difference between $\mathbf{x}_\mathrm{p}$ and a point on the line (for simplicity the reference point $\mathbf{x}_0$ is used).

This can be seen as a simple transformation vector for the origin of the x-,y-,z-coordinates $\mathbf{0}$ to the reference point $\mathbf{x}_0$. Having the reference point $\mathbf{x}_0$ as origin, the vector $\mathbf{v}_{0\mathrm{n}}$ between the reference point $\mathbf{x}_0$ and the nearest point on the particle track $\mathbf{x}_\mathrm{n}$ to the point $\mathbf{x}_\mathrm{p}$ can be

[1] There is no starting- nor ending-point and this vector is normalized to $|\mathbf{v}| = 1$

calculated. The vector $\mathbf{v}_{0n}$ is the scalar product between the start vector $\mathbf{v}_s$ and the normalized direction vector $\mathbf{v}$ multiplied with the normalized track vector $\mathbf{v}$.

$$\mathbf{v}_{0n} = (\mathbf{v}_s \cdot \mathbf{v}) \cdot \mathbf{v} \tag{6.1}$$

Knowing the nearest point $\mathbf{x}_n$ on the line

$$\mathbf{x}_n = \mathbf{v}_{0n} + \mathbf{x}_0 \tag{6.2}$$

The distance of the difference between the nearest point $\mathbf{x}_n$ and the point $\mathbf{x}_p$ can be calculated by

$$d = |\mathbf{x}_n - \mathbf{x}_p| \tag{6.3}$$

6.2.2 Generating randomized bin centres

The generation of random numbers was done with the TRandom3 class in the ROOT framework [8] which is based on the Mersenne Twister [33]. The seed for the random numbers was given by the unix timestamp[2].

The three dimensional cubic bins have a center point $\mathbf{x}_c$ and a n edge length l. The aim is to redistribute the center points within the cubic volume around the former bin.

TRandom3 provides a pseudo random value of double precision in the interval $[0.0, 1.0]$. By simply adding -0.5 the interval shifts to $[-0.5, 0.5]$. This random double a_i[3] times the edge length l shifts the center point within the bin volume. The new center point $\mathbf{x}_c^*$ can be calculated by

$$\mathbf{x}_c^* = \mathbf{x}_c + \begin{pmatrix} a_i l \\ a_{i+1} l \\ a_{i+2} l \end{pmatrix} \tag{6.4}$$

[2]Number of seconds passed since January 1, 1970 Coordinated Universal Time (UTC)
[3]The positive integer index i denotes the different random numbers

6.3 Additional Plots

This part of the appendix covers plots of the reconstruction algorithm. The different improvements made are listed as subsection to create a good overview.

6.3.1 Normal reconstruction

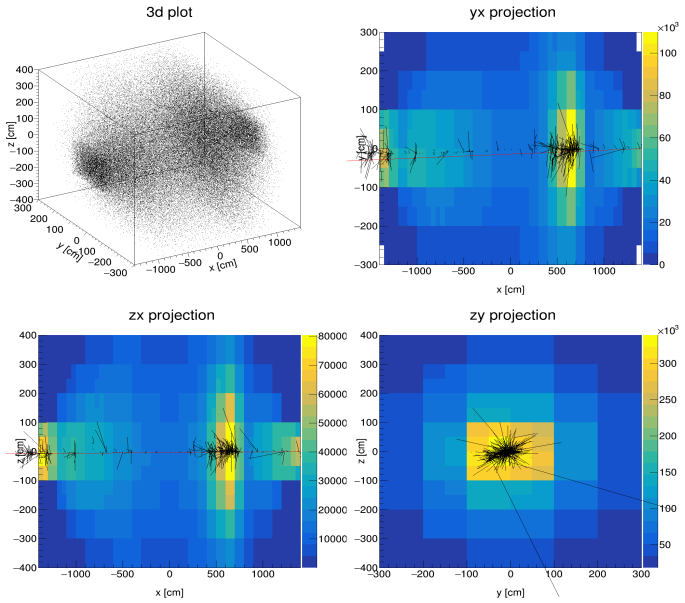

Figure 6.1: Normal reconstruction of a 20 GeV muon surpassing the center of the detector in the xy-plane.

6.3.2 Normal reconstruction with a cylindrical probability mask

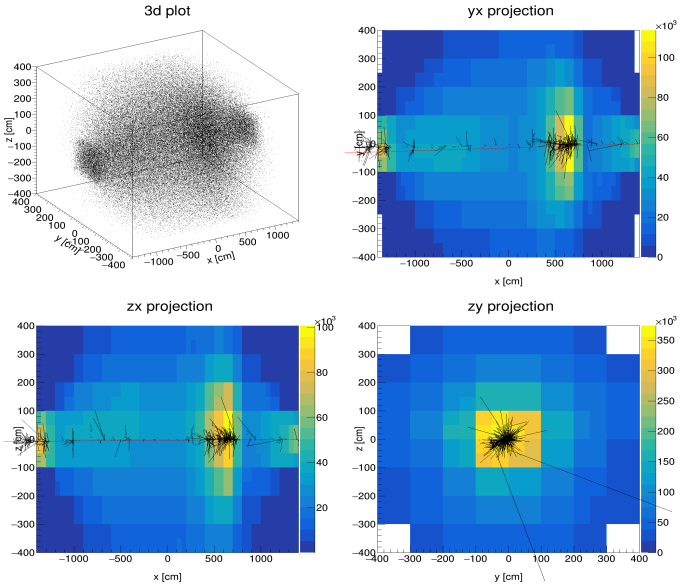

Figure 6.2: Normal reconstruction with a pre-defined probability mask of a 20 GeV muon surpassing the center of the detector in the xy-plane.

6.3.3 Reconstruction considering scattered light

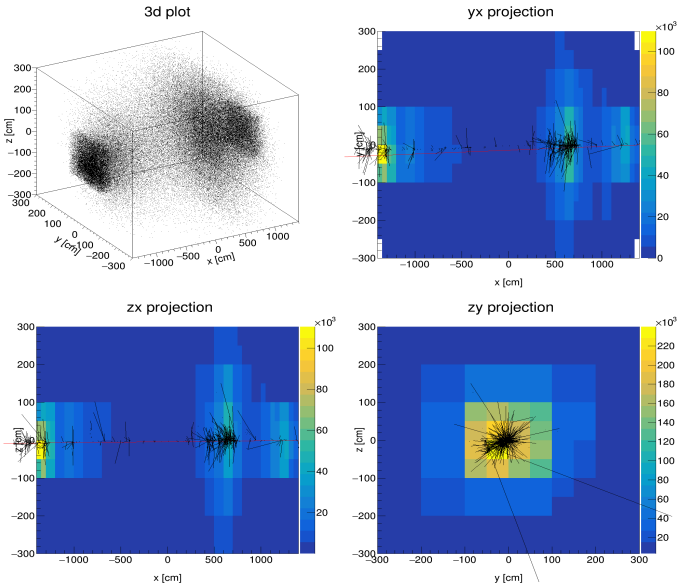

Figure 6.3: Reconstruction with a pre-defined probability mask and the SLA of a 20 GeV muon surpassing the center of the detector in the xy-plane.

6.4 Additional plots for the identification of showering muons

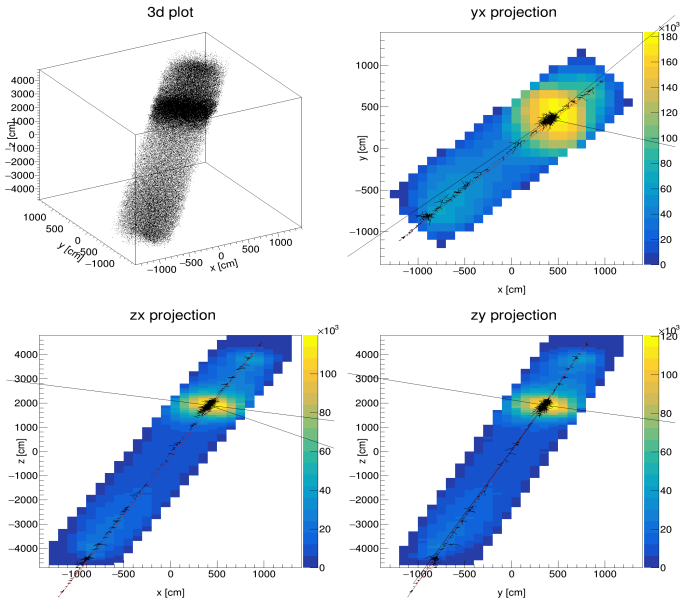

Figure 6.4: Projections of the reconstruction result with the particles of the MC-Data printed on top.

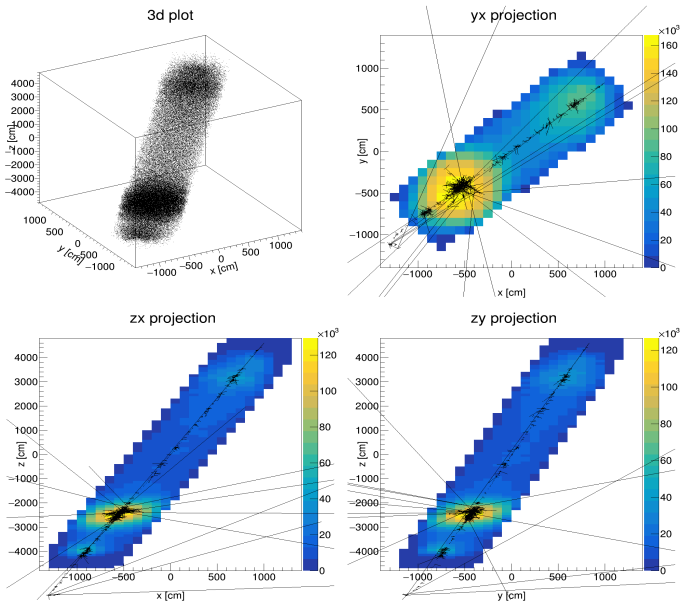

Figure 6.5: Projections of the reconstruction result with the particles of the MC-Data printed on top.

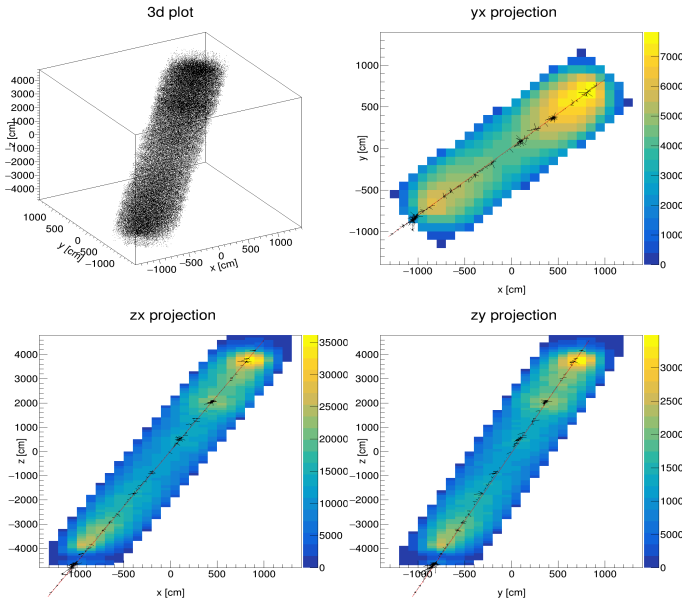

Figure 6.6: Projections of the reconstruction result with the particles of the MC-Data printed on top.

List of Figures

List of Tables

Abbreviations

BOREXINO Boron Solar Neutrino Experiment.

CC Charged Current.

CKM Cabibbo-Kobayashi-Maskawa.

CP Charge Parity.

DSNB Diffuse Supernova Neutrino Background.

FLUKA FLUktuierende KAskade.

JUNO Jiangmen Underground Neutrino Observatory.

KamLAND Kamioka Liquid Scintillator AntiNeutrino Detector.

LAB Linear AlkylBenzene.

LENA Low Energy Neutrino Astronomy.

LUT Look-Up-Table.

MC Monte Carlo.

NC Neutral Current.

NPP Nuclear Power Plant.

OM Optical Module.

OPERA Oscillation Project with Emulsion tRacking Apparatus.

P Parity.

PMNS Pontecorvo-Maki-Nakagawa-Sakata.

PMT Photomultiplier Tube.

QCD Quantum Chromo Dynamics.

QED Quantum Electro Dynamics.

RENO Reactor Experiment for Neutrino Oscillation.

SLA Scattered Light Algorithm.

SM Standard Model.

SNO Sudbury Neutrino Observatory.

T2K Tokai to Kamioka.

UTC Coordinated Universal Time.

WLS WaveLength Shifting.

Bibliography

[1] JUNO Projekt Neutrino Forschungsgruppe Universität Hamburg. Accessed: 15.01.2017.

[2] Open streetmap. ©openstreetmap contributors, licensed under the creative commons attribution-sharealike 2.0 license (cc by-sa). Accessed: 15.01.2017.

[3] T. Adam. The OPERA experiment Target Tracker. 2007.

[4] T. Adam et al. Juno conceptual design report, 2015.

[5] S. Agostinelli et al. Geant4a simulation toolkit. *Nuclear Instruments and Methods in Physics Research Section A: Accelerators, Spectrometers, Detectors and Associated Equipment*, pages 250 – 303, 2003.

[6] M. Agostini et al. Results on neutrinoless double beta decay of 76Ge from GERDA Phase I. 2013.

[7] Fengpeng An et al. Neutrino physics with juno. *Journal of Physics G: Nuclear and Particle Physics*, 2016.

[8] I. Antcheva et al. {ROOT} c++ framework for petabyte data storage, statistical analysis and visualization. *Computer Physics Communications*, 2009.

[9] John N. Bahcall, Aldo M. Serenelli, and Sarbani Basu. New solar opacities, abundances, helioseismology, and neutrino fluxes. 2004.

[10] H. A. Bethe. Energy Production in Stars. *Phys. Rev.*, Mar 1939.

[11] J.B. Birks, D.W. Fry, L. Costrell, and K. Kandiah. *The Theory and Practice of Scintillation Counting: International Series of Monographs in Electronics and Instrumentation*. International series of monographs on electronics and instrumentation. Elsevier Science, 2013.

[12] F. Capozzi, G. L. Fogli, E. Lisi, A. Marrone, D. Montanino, and A. Palazzo. Status of three-neutrino oscillation parameters, circa 2013. 2013.

[13] Borexino Collaboration et al. Final results of borexino phase-i on low energy solar neutrino spectroscopy. 2013.

[14] SNO Collaboration. Measurement of the rate of $\nu_e + d - - > p + p + e^-$ interactions produced by 8b solar neutrinos at the sudbury neutrino observatory. 2001.

[15] The KamLAND Collaboration. Production of Radioactive Isotopes through Cosmic Muon Spallation in KamLAND. 2009.

[16] C. L. Cowan, F. Reines, F. B. Harrison, H. W. Kruse, and A. D. McGuire. Detection of the Free Neutrino: a Confirmation. *Science*, 1956.

[17] Raymond Davis, Don S. Harmer, and Kenneth C. Hoffman. Search for Neutrinos from the Sun. *Phys. Rev. Lett.*, May 1968.

[18] W. Demtröder. *Experimentalphysik 4*. Experimentalphysik / Wolfgang Demtröder. Springer Berlin Heidelberg, 2009.

[19] Lisa Edelhäuser and Alexander Knochel. *Tutorium Quantenfeldtheorie - Was Sie schon immer über QFT wissen wollten, aber bisher nicht zu fragen wagten*. Springer-Verlag Berlin Heidelberg.

[20] Joshua Ellis. TikZ-Feynman: Feynman diagrams with TikZ. 2016.

[21] G. Fiorentini, G. L. Fogli, E. Lisi, F. Mantovani, and A. M. Rotunno. Mantle geoneutrinos in KamLAND and Borexino. 2012.

[22] L. Gao et al. Attenuation length measurements of liquid scintillator with LabVIEW and reliability evaluation of the device. 2013.

[23] Marco Grassi, Jarah Evslin, Emilio Ciuffoli, and Xinmin Zhang. Showering Cosmogenic Muons in A Large Liquid Scintillator. 2014.

[24] Marco Grassi, Jarah Evslin, Emilio Ciuffoli, and Xinmin Zhang. Vetoing Cosmogenic Muons in A Large Liquid Scintillator. 2015.

[25] Daniel Hartwig. Directional analysis of electrons and discrimination between electrons and muons at high energies in large liquid scintillator detectors. 2016.

[26] Dominikus Hellgartner. Advanced Event Reconstruction in LENA and Precision Attenuation-Length Measurements in Liquid Scintillators. 2015.

[27] J.Jackson. *Klassische Elektrdynamik*. De Gruyter Studium, 2006.

[28] Benedict Kaiser. Commissioning of a testfacility to characterise JUNO photomultipliers. 2016.

[29] T. W. B. Kibble. History of electroweak symmetry breaking. 2015.

[30] William R. Leo. *Techniques for nuclear and particle physics experiments : a how-to approach*. Springer, Berlin u.a., 2., rev. ed edition, 1994.

[31] Shirley Weishi Li and John F. Beacom. First calculation of cosmic-ray muon spallation backgrounds for MeV astrophysical neutrino signals in Super-Kamiokande. 2014.

[32] Sebastian Lorenz. Topological Track Reconstruction in Liquid Scintillator and LENA as a Far-Detector in an LBNO Experiment. 2016.

[33] Makoto Matsumoto and Takuji Nishimura. Mersenne Twister: A 623-dimensionally Equidistributed Uniform Pseudo-random Number Generator. *ACM Trans. Model. Comput. Simul.*, January 1998.

[34] David Johannes Meyhöfer. Vertex reconstruction in large liquid scintillator detectors. 2017.

[35] Randolph Möllenberg. LENA Monte Carlo Simulation User Documentation, 2013.

[36] L. Oberauer, C. Grieb, F. von Feilitzsch, and I. Manno. Light Concentrators for Borexino and CTF. 2003.

[37] C. Patrignani et al. Review of Particle Physics. *Chin. Phys.*, 2016.

[38] D.H. Perkins. *Particle Astrophysics*. Oxford Master Series in Condensed Matter Physics. Oxford University Press, 2003.

[39] X. Qian and P. Vogel. Neutrino Mass Hierarchy. 2015.

[40] Stefan Scherer. *Symmetrien und Gruppen in der Teilchenphysik*. Springer-Verlag Berlin Heidelberg.

[41] Hauke Ortwin Schmidt. Parallelisierung eines Algorithmus zur topologischen Rekonstruktion in Flüssigszintillator-Detektoren. 2016.

[42] O. Y. Smirnov et al. Measurement of neutrino flux from the primary proton–proton fusion process in the Sun with Borexino detector. 2015.

[43] Virginia Strati, Marica Baldoncini, Ivan Callegari, Fabio Mantovani, William F. McDonough, Barbara Ricci, and Gerti Xhixha. Expected geoneutrino signal at juno, 2014.

[44] Shimpei Tobayama. Recent Updates on fiTQun, a New Event Reconstruction Algorithm for Water Cherenkov Detectors, 2013.

[45] L. Wolfenstein. Neutrino oscillations in matter. *Phys. Rev. D*, May 1978.

[46] Björn Wonsak. Institut für Experimentalphysik Hamburg, Forschungsgruppe Neutrinophysik.

[47] M. Wurm. Status of LENA R&D, Conference talk, 2014. at APC Paris.

[48] Michael Wurm et al. Optical Scattering Lengths in Large Liquid-Scintillator Neutrino Detectors. 2010.

[49] Xing-Chen Ye et al. Preliminary study of light yield dependence on LAB liquid scintillator composition. 2015.

[50] K. Zuber. *Neutrino Physics*. Series in High Energy Physics, Cosmology and Gravitation. CRC Press, 2003.

Danksagung

Vielen Dank an die gesamte Neutrinophysik Arbeitsgruppe für die entspannte, nette und lehrreiche Zeit. Hier gilt vor allem Dr. Björn Wonsak und Prof. Dr. Caren Hagner mein Dank für die Möglichkeit einer Arbeit in diesem spannendem Feld der Physik. Vor allem gilt Björn mein Dank für die angenehmen Gespräche über mein Thema.

Für das Korrekturlesen danke ich Henning, der desweiteren bewiesen hat, dass auch Eltern cool sein können.

Simon und Benedict danke ich für fachliche Hilfe und die immer nette Zerstreuung, welche nur Freunde untereinander verbreiten können.

Meinem Lieblingsdoktoranden und Hello Kitty Fanatiker David danke ich für die immense Hilfe bei Programmierfragen und die lustigen Gespräche ab 18 Uhr, wenn wir nach zwei Stunden Arbeit frustriert waren.

Die Ersatzbank (Kathi, Hauke, Daniel, Benedikt) bleibt nicht ungenannt, denn das Büroklima war immer ungemein nett.

Der Bier-um-vier-Kooperation danke ich für die netten Freitagnachmittage bei kaltem Getränk und lustigem Gesprächsstoff.

Desweiteren möchte ich diversen Nicht-Physikern einen Dank aussprechen, dass sie mich immer unterstützt haben.

Meinen Eltern, die mich noch nicht verhungern lassen haben, und meiner Schwester, die nur diesen Teil hier lesen wird, um zu sehen, ob sie aufgeführt wurde.

Jesper, Baron von Arm Curl, der sich als findiger Fehlerfuchs durch die Bachelorarbeit gewühlt hat und zudem ein zuverlässiger Freund und Trainingspartner ist.

Jahne, der beim Lesen dieser Arbeit hoffentlich ein wenig versteht, möchte ich für die nun schon sehr lange Freundschaft danken.

Weiterhin danke ich der TS-Gruppe für die netten verzockten Stunden, der Ela-Truppe für die netten Feiern und meiner Mitbewohnerin Mona für die herzliche Atmosphäre zuhause.

Bei so viel Dankbarkeit, muss noch meine Undankbarkeit dem Root-Framework ausgesprochen werden, welches mich des öfteren zur segmentation violation getrieben hat.

Erklärung

Hiermit bestätige ich, dass die vorliegende Arbeit von mir selbständig verfasst wurde und ich keine anderen als die angegebenen Hilfsmittel insbesondere keine im Quellenverzeichnis nicht benannten Internet-Quellen benutzt habe und die Arbeit von mir vorher nicht einem anderen Prüfungsverfahren eingereicht wurde. Die eingereichte schriftliche Fassung entspricht der auf dem elektronischen Speichermedium. Ich bin damit einverstanden, dass die Bachelorarbeit veröffentlicht wird.

Hamburg, den 29.03.2017

Felix Benckwitz